CWP-617
January 2009

Modeling of Seismic Signatures for Reservoir Characterization: Applications Involving Fracture- and Stress-induced Seismic Velocity Anisotropy

Rodrigo Felício Fuck

— Doctoral Thesis —
Geophysics

Defended on November 25, 2008

Committee Chair:	Prof. Luis Tenorio
Advisor:	Prof. Ilya Tsvankin
Committee members:	Prof. Dave Hale
	Prof. Michael L. Batzle
	Prof. Terrence K. Young
	Prof. Eric Nelson

Center for Wave Phenomena
Colorado School of Mines
Golden, Colorado 80401
(1) 303 273-3557

Abstract

High demand for hydrocarbons combined with declining reserves has contributed to a surge in the use of seismic reservoir monitoring to optimize both production and recovery of oil and gas. In this thesis, I analyze the contribution of fracture- and stress-induced velocity anisotropy to seismic signatures typically used in reservoir characterization. To gain insight into the behavior of seismic signatures, I develop closed-form analytic equations parameterized in terms of the fracture compliances or subsurface stresses and strains.

In the study of fracture-related azimuthal anisotropy, I go beyond the conventional model of penny-shaped cracks and develop analytic solutions for microcorrugated fracture sets in isotropic background rock. The asperities of the fracture faces, for instance, cause the shear-wave splitting coefficient at vertical incidence to become sensitive to fluid saturation, especially for tight, low-porosity host rock. In contrast to the model with two orthogonal sets of penny-shaped cracks, the influence of microcorrugation rotates the NMO (normal-moveout) ellipses of all three reflection modes (P, S_1, S_2) with respect to the fracture strike directions. These results can be used to identify the underlying physical model and, potentially, to estimate the combinations of fracture parameters constrained by multicomponent, multiazimuth seismic data.

In many hydrocarbon fields, reservoir compaction due to depletion can cause surface subsidence or shearing of wells. The current technology to monitor compaction using traveltime shifts of P-wave reflection events is limited to zero-offset rays, which restricts analysis to the vertical-velocity (and stress) changes. To overcome such limitation, I give an analytic 3D descriptioin of traveltime shifts that can be efficiently used for numerical modeling in the offset domain and, ultimately, for reconstructing the stress distribution around compacting reservoirs. The approximated solution adequately reproduces the behavior of time shifts, although its accuracy decreases for reflectors below areas with large velocity perturbations. The sign and magnitude of the offset variation of time shifts are sensitive to the horizontal and shear deviatoric stress components and depend on the CMP location with respect to the reservoir. Large contrasts in the rigidity modulus μ ($> 25\%$) across the reservoir boundaries can reduce the offset variation of traveltime shifts but only for reflectors close to the top or bottom of the reservoir. Overall, analysis of traveltime shifts as a function of offset should provide better constraints on the geomechanical changes around depleting reservoir blocks and improve interpretation of 4D seismic data.

Table of Contents

Acknowledgments

Pursuing a Ph.D. degree is a solitary (ad)venture, but I would not have done it without the help and support of a lot of people. First and foremost, I want to thank my wife, Simone Fernandes Sabatier Fuck, and our children, Rafael and Julia, for their love and support throughout all my years here at the Colorado School of Mines. They were a constant source of inspiration, motivation and joy. I thank my father, Reinhardt Adolfo Fuck, my mother, Maria Isaura Felício Fuck, and my in-laws, Pierre Julien and Neide Sabatier, for being loving, caring and so dependable; I thank my sisters, Ana Carolina and Beatriz Helena, and my brother Luciano, for being there when I need it and for never sparing a word of encouragement.

I am grateful to my thesis adviser, Dr. Ilya Tsvankin, for his guidance, patience, friendship and support, which were instrumental for my success in the Ph.D. program. I am also thankful for the help, comments, suggestions and contributions that I received from the members my of thesis committee, Dr. Mike Batzle, Dr. Terry Young, Dr. Dave Hale, Dr. Luis Tenorio, and Dr. Eric Nelson. I am also in debt with Dr. Andrey Bakulin (WesternGeco) for his invaluable help, suggestions, feedback and collaboration in the research project on traveltime shifts.

I thank the Geophysics department as whole and, in particular, the faculty of the Center for Wave Phenomena (CWP) and of the Reservoir Characterization project, for the incredible educational and professional experience I had at the Colorado School of Mines. I also thank the Geophysics department staff, especially Sara Summers, Susan Venable and Dawn Umpleby for always being so professional and helpful. My stay at CWP was made all the more special by Michele Szobody and Barbara McLenon, people who not only work to make your life easier, but merrier. I am also in debt with John Stockwell for all his help with computer related issues and for the many discussions about geophysics and math. My internships were great learning experiences as well, and I was privileged to work with bright people, which also contributed to my education: Dr. John Sumner, Dr. Grant Gist, Dr. Chris Finn, Dr. Charlie Ching and Dr. Tommie Rape from ExxonMobil Upstream Research Company; Dr. Leon Thomsen and Dr. Ganyuan Xia from BP America.

One of the best things of the Geophysics department is the culturally diverse and incredibly bright student body. They are special group of friendly people who are fun to be around. In particular, for me was an honor and a pleasure to meet and to study with Alison Malcolm, Carlos Pacheco, Kasper Van Wijk, Alex Grêt, Matt Haney, Matt Reynolds, Reynaldo Cardona, Ludmila Adam, Kjeitl "KJ" Jansen, Farnoush Forghani, Myoung Jae Kwon, Ronnie Hoffmann, Neil Dannemiller, Werner Heigl, John Mathewson, Derek Parks, and the newcomers Francesco Perrone and Bharath Shekar. I also enjoyed a lot the friendship of my colleagues of the A(nisotropy)-team, from whom I always learned something new: Debashish Sarkar, Pawan Dewangan, Yaping Zhu, Xiaoxia Xu, Jyoti Behura, Steve

Smith, Xiaoxiang Wang and Jia Yan. I also appreciate the support of my dear friends Vinicio Sanchez, Amir Ghaderi, Dirk Gajewski, Ramzy Al-Zayer and Tagir Galikeev. A big thank you goes to my pals of the “Brazilian mafia”, Ivan Vasconcelos, Gabriela Melo, Eduardo Filpo and Marco Antônio Braga. They made the bright days shinier, and helped me endure the bleak ones. In addition, I thank Magnus and Cecilia Skold for being just like family to me.

Finally, my graduate studies here at CSM were made possible by funding provided in part by CAPES (Coordenação de Aperfeiçoamento de Pessoal de Nível Superior), Brazilian Ministry of Education, under scholarship BEX 1340-0/00, and in part by the Consortium Project on Seismic Inverse Methods for Complex Structures at the Center for Wave phenomena. I thank these sponsors for providing me this life-changing opportunity.

Chapter 1

Introduction

The growing demand for hydrocarbons and declining oil and gas reserves have made reservoir characterization an important area of research in geosciences. Indeed, even a small increase in the recovery rate of oil or gas not only lengthens the life of the field but also reduces operational costs. Therefore it is essential to study the reservoir architecture and compartmentalization, as well as faults and fractures and production-induced dynamic changes.

The areal coverage and high vertical resolution of reflection seismic data make them a good source of information about the inter-well properties of reservoir rocks. Hence, reflection data are playing a leading role in the development of new technologies in reservoir characterization and monitoring. Among these new technologies is application of seismic velocity and amplitude anisotropy to map reservoir properties, such as fracturing and compartmentalization, and to monitor dynamic changes in the reservoir caused by depletion. For example, the azimuthal variation of normal-moveout (NMO) velocities and amplitude-variation-with-offset (AVO) attributes can help to estimate both the direction and intensity of fracture sets, which can act as the fluid and gas pathways.

In this thesis, I analyze how velocity anisotropy affects commonly observed seismic signatures used in reservoir characterization, such as the traveltime changes, NMO velocities and AVO attributes. To gain insight into the behavior of seismic signatures, I develop closed-form analytic equations in terms of the fracture parameters or subsurface stresses. These analytic expressions are obtained by means of linearization assuming the stress- or fracture-induced velocity anisotropy to be weak.

Chapters 2–5 of this thesis have been written as individual papers. In particular, chapters 2 and 3 have already been published (Fuck and Tsvankin, 2006; Fuck et al., 2009).

In *Chapter 2*, I investigate how seismic signatures commonly used to detect reservoir fractures can be influenced by complex fracture rheology. Instead of the commonly used penny-shape crack model, I use one in which fracture faces contain asperities or microcorrugations. Motivation to take this approach came from Cardona (2002), which reports misalignments among seismic signatures in Weyburn Field, Canada, that cannot be explained by models with penny-shape fractures. The microcorrugations allow coupling of normal stresses to shear displacements across the fracture faces and vice-versa during wave propagation through the fractured medium. This coupling causes the misalignment between the directions of the fracture sets and the trends of seismic signatures, such as NMO ellipse or azimuthally varying AVO gradient.

Chapter 3 focuses on using stress-induced anisotropy in monitoring pore-pressure changes and compaction of hydrocarbon reservoirs. Existing methodology employs time-lapse traveltime shifts of events recorded above and below the reservoir on stacked data. Such traveltime shifts, however, carry information about depletion-induced subsurface changes only in the vertical direction. I derive an analytic expression that can be used to model traveltime shifts in a completely general way. It allows reflectors to be described by 3D surfaces and for traveltime shifts to be computed for nonzero offsets, taking into account the heterogeneous and anisotropic compaction-induced velocity changes. Using first-order perturbation, traveltime shifts are expressed as a linear combination of the geometric and velocity changes brought about by the pore-pressure variation inside the reservoir. 2D numerical modeling shows that traveltime shifts are largely caused by the anisotropic velocity perturbations related to the deviatoric stress changes. Thus, the offset analysis of traveltime shifts can help to constrain not only the vertical, but also the horizontal and shear stress changes and improve interpretation of 4D seismic data.

The contrast in the elastic properties across the reservoir boundaries increases the magnitude of isotropic velocity perturbations during reservoir compaction. To investigate this issue in *Chapter 4*, I study the offset variation of traveltime shifts for models in which the background velocity is heterogeneous. The first group of models is based on the homogeneous model used in Chapter 3, in which the contrast between the reservoir and the host rocks is gradually changed. I also analyzed a layered model based on velocity profiles from Valhall field in the North Sea. The numerical simulations demonstrate that significant isotropic velocity perturbations are observed only for large contrasts in rigidity modulus μ (¿ 25%) and are restricted to reflections close to the reservoir. Overall, the offset variation of traveltime shifts still provides critically important information needed to constrain depletion-induced stress and strain changes around compacting reservoirs.

Stress-induced velocity perturbations in Chapters 3 and 4 are expressed not in terms of a fracture model—a more common approach adopted in the literature—but through strain-sensitivity tensors. These so-called third-order elastic (TOE) tensors, allow for a general solution to the problem of translating stress and strain subsurface changes into velocity perturbations. However, sixth-rank TOE tensors are difficult to manipulate because of the large number of their components. In particular, determination of the symmetry of the elastic stiffness tensor for a stressed medium (this tensor is responsible for traveltime shifts) is cumbersome even for an isotropic strain-sensitivity tensor. In *Chapter 5* I present a matrix representation of these tensors that simplifies the process of evaluating the symmetry of the stressed medium given any type of symmetry of the TOE and strain tensors.

Finally, the general conclusions and recommendations for future work are given in *Chapter 6*.

Chapter 2

Seismic signatures of two orthogonal sets of vertical microcorrugated fractures

2.1 Summary

Conventional fracture-characterization techniques operate with the idealized model of penny-shaped (rotationally invariant) cracks and ignore the roughness (microcorrugation) of fracture surfaces. Here, we develop analytic solutions based on the linear-slip theory to examine wave propagation through an effective anisotropic medium that contains two microcorrugated, vertical, orthogonal fracture sets in isotropic background rock.

The off-diagonal elements of the compliance matrix associated with the corrugation cause the deviation of the polarization vectors of the vertically traveling S-waves from the horizontal plane. Also, the shear-wave splitting coefficient at vertical incidence becomes sensitive to fluid saturation, especially for tight, low-porosity host rock. In contrast to the model with two orthogonal sets of penny-shaped cracks, the NMO (normal-moveout) ellipses of all three reflection modes (P, S_1, S_2) are rotated with respect to the fracture strike directions. Another unusual property of the fast shear wave S_1, which can help to distinguish between models with one and two microcorrugated fracture sets, is the misalignment of its polarization vector at vertical incidence and the semi-major axis of the NMO ellipse.

The model analyzed here may adequately describe the orthogonal fracture sets at Weyburn Field in Canada, where the axes of the P-wave NMO ellipse deviate from the S_1-wave polarization direction. Our results can be used to identify the underlying physical model and, potentially, to estimate the combinations of fracture parameters constrained by multicomponent, multiazimuth seismic data.

2.2 Introduction

A key element in reservoir characterization is identification of fluid pathways that control the production of hydrocarbons. Since such pathways are often formed by fracture networks and joints, detection and analysis of fractures using seismic data is an important area of reservoir geophysics (e.g., Lynn et al., 1995; Pérez et al., 1999; Mallick et al., 1998; DeVault et al., 2002). In a series of three papers, Bakulin et al. (2000a,b,c) outlined several practical approaches to estimating fracture parameters from surface seismic and VSP (vertical seismic profiling) data. Using the linear-slip theory described by Schoenberg (1980) and Schoenberg and Sayers (1995), they expressed the equations describing the NMO (normal-moveout) ellipses and AVO (amplitude-variation-with-offset) gradients of reflected waves in terms of the fracture compliances and orientations. These analytic expressions helped Bakulin et al. (2000a,b,c) to devise fracture-characterization methods based on the inversion of multicomponent, mutliazimuth reflection data.

The work of Bakulin et al. (2000a,b,c) was largely focused on the idealized model of rotationally invariant fractures (i.e., oblate spheroids), which have perfectly smooth surfaces and are often called “penny-shaped cracks.” Grechka et al. (2003) extended the results of Bakulin et al. (2000a) by considering a single set of the most general vertical fractures allowed by the linear-slip formalism. Physically, such “general” fractures have rough (microcorrugated) surfaces and are described by a compliance matrix that has nonzero off-diagonal elements. The results of Grechka et al. (2003) show that fracture rheology has a strong impact on the velocities and reflection moveout of pure modes, as well as on the shear-wave splitting coefficient. For instance, if the fractures are rotationally invariant, the axes of the NMO ellipses from horizontal reflectors are always parallel and perpendicular to the fracture strike. By contrast, for a set of general fractures only the NMO ellipse of the fast shear wave S_1 maintains its alignment with the fractures, while the ellipses of the P- and S_2-waves may have different orientations.

While the methodology of Grechka et al. (2003) helps to treat realistic fracture rheologies, their results are limited to effective media that include only one general fracture set. Many naturally fractured reservoirs, however, contain two (or even more) systems of fractures, which are often orthogonal to each other (Schoenberg and Sayers, 1995; Grechka and Tsvankin, 2003). Here, we study an effective anisotropic medium formed by two vertical, orthogonal, microcorrugated fracture sets embedded in isotropic background rock.

Our motivation for investigating this model comes from analysis of multiazimuth P- and S-wave reflection data acquired at Weyburn Field in Canada, where borehole imaging and geological information reveal the presence of three open vertical fracture sets (Cardona, 2002). Over most of the field two of these sets, which have relatively close orientations, seem to act as a single effective fracture set orthogonal to the dominant NE-SW fracture trend. If these two orthogonal sets are rotationally invariant, the effective medium should have orthorhombic symmetry, which is confirmed by analysis of seismic data (Cardona, 2002). In the southern part of the field, however, the orthorhombic model fails to explain the misalignment of the P-wave NMO ellipse and the fast S-wave polarization direction. As shown by Cardona (2002), even the introduction of a third set of penny-shaped cracks is insufficient to fit the seismic signatures in that area. Making the fractures microcorrugated can help to develop an effective model with two orthogonal fracture sets that fully accounts for the observed anomaly.

The objective of this paper is to analyze the influence of two orthogonal sets of microcorrugated fractures on the NMO ellipses and AVO gradients of reflected waves, as well as on the shear-wave splitting coefficient. Applying the weak-anisotropy approximation, we derive closed-form analytic expressions for these common seismic signatures in terms of the fracture compliances. Although the feasibility study by Grechka and Tsvankin (2003) indicates that the individual compliances of two general fracture sets cannot be resolved even from the complete effective stiffness tensor, our results can assist in retrieving certain combinations of the compliances and identifying the presence of two fracture sets.

2.3 Effective Medium

The model considered here includes two orthogonal sets of vertical fractures of the most general rheology embedded in a purely isotropic background (Figure 2.1). To compute the elastic stiffnesses for the fractured model, we employ the linear-slip theory introduced by Schoenberg (1980) and further discussed by Schoenberg and Sayers (1995) and others (see Appendix AA). According to the linear-slip formalism, fractures can be described as non-welded interfaces that cause discontinuities in the displacement field (i.e., slips). The slips are taken to be proportional to the product of the (continuous) tractions that act across the fractures and the excess fracture compliances.

The most general mathematical description of a fracture set in the linear-slip theory is a 3×3 symmetric matrix of the excess compliances (Grechka et al., 2003):

$$\mathbf{K} = \begin{pmatrix} K_N & K_{NH} & K_{NV} \\ K_{NH} & K_H & K_{VH} \\ K_{NV} & K_{VH} & K_V \end{pmatrix} , \tag{2.1}$$

where K_N is the normal compliance that relates the normal traction (stress) across the fracture surface to the normal slip, and K_V and K_H are the tangential compliances relating the shear stresses to the tangential slips. The off-diagonal compliances incorporate the mechanical effects of irregularities and asperities on the fracture surfaces (Figure 2.2) by coupling the normal slips to the shear stresses and vice versa (Schoenberg and Douma, 1988). Due to lack of experimental data on this coupling mechanism (with the exception of Nakagawa et al., 2000), it is unclear what scale of microcorrugations is needed to produce measurable off-diagonal compliances. As follows from the theoretical analysis of Kachanov and Sevostianov (2005), microcorrugations should be mismatched and should provide contact points between the two fracture surfaces to ensure significant coupling.

Fractures are usually classified in accordance with the structure of their compliance matrix $\mathbf{K}$ (equation 2.1). If at least one of the off-diagonal elements does not vanish, the fractures are sometimes called "monoclinic" (Schoenberg and Douma, 1988). Fractures described by a diagonal matrix $\mathbf{K}$ are called "orthotropic" or simply "diagonal;" rotationally invariant fractures are a special subset of diagonal fractures corresponding to equal tangential compliances $K_V = K_H$.

In the linear-slip theory, the compliance matrix of the effective model is obtained by adding the compliance matrices of the two corrugated fracture sets to that of the isotropic background (Appendix A). The effective stiffness elements c_{ij}, obtained by inverting the compliance matrix, can be simplified by linearizing the exact values in the normalized compliances called *fracture weaknesses* (Schoenberg and Douma, 1988; Bakulin et al., 2000a). The weaknesses vary from zero for unfractured medium to unity for intensely fractured rock in which the body-wave velocities go to zero in a certain direction. Since the weaknesses for typical fractured formations are much smaller than unity, they can be conveniently used in developing closed-form approximations for seismic signatures. The fracture weaknesses

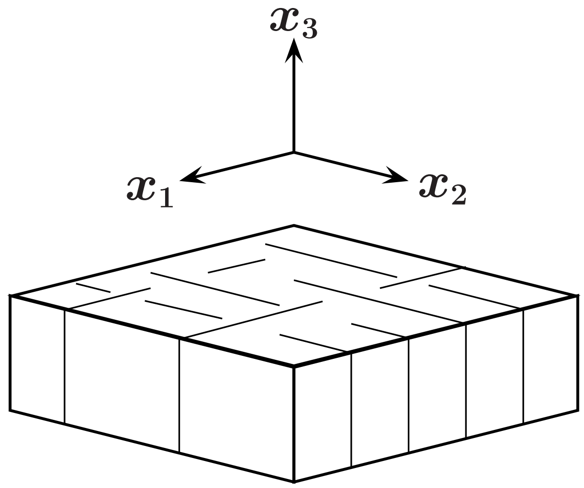

Figure 2.1. Model of two sets of orthogonal vertical fractures. Since the linear-slip theory does not account for the interaction of fracture sets, fractures are not supposed to intersect each other. The parameters of the fracture set with the normal parallel to the x_1-axis are denoted by the subscript “1” in the text.

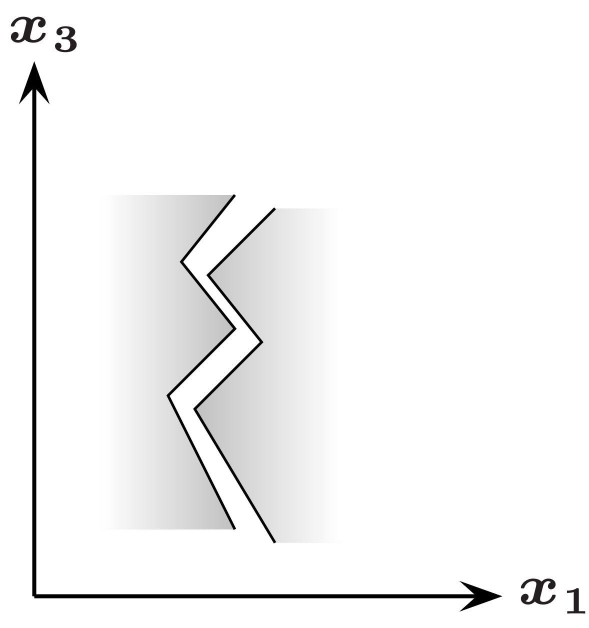

Figure 2.2. Idealized fracture with corrugations that are offset from one face to the other (adapted from Schoenberg and Douma, 1988). In such a model, the normal slips (discontinuities in displacement) are coupled to the shear stresses and vice-versa. For example, slip in the x_3-direction will cause the coupling of the fracture faces and, therefore, shear stress in the x_1-direction.

Δ_N, Δ_V, Δ_H, Δ_{NV}, Δ_{NH}, and Δ_{VH} for our model are defined in equations B.1–B.6.

The effective stiffness matrix linearized in the weaknesses of both fracture sets can be represented as (see Appendix B)

$$\mathbf{c} = \begin{pmatrix} c_{11} & c_{12} & c_{13} & \chi c_{24} & c_{15} & c_{16} \\ c_{12} & c_{22} & c_{23} & c_{24} & \chi c_{15} & c_{26} \\ c_{13} & c_{23} & c_{33} & \chi c_{24} & \chi c_{15} & c_{36} \\ \chi c_{24} & c_{24} & \chi c_{24} & c_{44} & 0 & c_{46} \\ c_{15} & \chi c_{15} & \chi c_{15} & 0 & c_{55} & c_{56} \\ c_{16} & c_{26} & c_{36} & c_{46} & c_{56} & c_{66} \end{pmatrix}, \tag{2.2}$$

where

$$\chi \equiv \frac{\lambda}{(\lambda + 2\mu)} .$$

The linearized stiffnesses c_{ij} are given in equations B.10–B.30. According to equation 2.2, the effective model has the most general, triclinic symmetry (i.e., it does not have symmetry planes or axes of rotational symmetry), with only one vanishing elastic constant, $c_{45} = c_{54}$. This is not surprising since even a single set of microcorrugated fractures creates an effective triclinic medium. Nonetheless, only 14 out of the 20 elastic constants are independent because the effective model is constructed using the two Lamé parameters of the isotropic background (λ and μ) and 12 fracture compliances (six for each fracture set). Note that if the fracture azimuth is unknown, it is also necessary to introduce an orientation angle that defines the azimuth of one of the sets in a specified coordinate frame.

By dividing the matrix $\mathbf{c}$ into 3×3 submatrices $\mathbf{c}_i$, it can be represented in block form:

$$\mathbf{c} = \left(\begin{array}{c|c} \mathbf{c}_1 & \mathbf{c}_2 \\ \hline \mathbf{c}_2^T & \mathbf{c}_3 \end{array} \right); \tag{2.3}$$

the superscript "T" denotes transposition. The influence of the complex fracture rheology in our model on the structure of the stiffness matrix can be understood by comparing the matrix 2.3 with that for an effective orthorhombic medium due to two orthogonal sets of *rotationally invariant* fractures (Bakulin et al., 2000b):

$$\mathbf{c}^{\text{orth}} = \left(\begin{array}{c|c} \mathbf{c}_1^{\text{orth}} & \mathbf{0} \\ \hline \mathbf{0} & \mathbf{c}_3^{\text{orth}} \end{array} \right). \tag{2.4}$$

Clearly, the block $\mathbf{c}_2$ vanishes if the fractures are rotationally invariant. Note that the matrix $\mathbf{c}_3^{\text{orth}}$ in equation 2.4 is diagonal, and c_{66} contained in $\mathbf{c}_3^{\text{orth}}$ is a linear combination of c_{44} and c_{55}.

2.4 Vertical Wave Propagation

In this section we examine how the microcorrugations of the fracture faces affect the propagation of plane waves in the veritcal direction.

2.4.1 Approximate Velocities and Polarizations

The phase velocities and polarization vectors of vertically propagating plane waves can be obtained by solving the Christoffel equation for the effective medium described by the stiffness matrix 2.2. Applying the first-order perturbation theory (e.g., Jech and Pšenčik, 1989; Pšenčik and Vavryčuk, 2002) and linearizing the vertical velocities of the P-, S_1-, and S_2-waves in the weaknesses yields

$$V_P = V_{Pb}\left[1 - \frac{1}{2}\left(\Delta_{N_1} + \Delta_{N_2}\right)\chi^2\right], \tag{2.5}$$

$$V_{S1} = V_{Sb}\left(1 - \frac{\Delta_{V_2}}{2}\right), \tag{2.6}$$

$$V_{S2} = V_{Sb}\left(1 - \frac{\Delta_{V_1}}{2}\right), \tag{2.7}$$

where V_{Pb} and V_{Sb} are the P- and S-wave velocities in the isotropic background, whereas Δ_{N_i} and Δ_{V_i} denote the normal and vertical weaknesses of fracture sets 1 and 2, as indicated by the subscript i. It is assumed that the first set has a larger weakness Δ_V than the second set; otherwise, equation 2.6 for V_{S1} would give the vertical velocity of the slow S-wave. Although the vertical velocities are influenced by the presence of fractures, equations 2.5–2.7 do not contain off-diagonal weaknesses and, therefore, coincide with the linearized velocities for rotationally invariant fractures (Bakulin et al., 2000b).

In contrast, the polarization vectors ($\mathbf{U}$) of the vertically traveling waves contain first-order contributions of the off-diagonal compliances Δ_{NV_i}:

$$\mathbf{U}_P \approx \left(a\,\Delta_{NV_1},\, a\,\Delta_{NV_2}, 1\right)^T, \tag{2.8}$$

$$\mathbf{U}_{S1} \approx \left(0, 1,\, -a\,\Delta_{NV_2}\right)^T, \tag{2.9}$$

$$\mathbf{U}_{S2} \approx \left(1, 0,\, -a\,\Delta_{NV_1}\right)^T, \tag{2.10}$$

where

$$a \equiv \frac{(1-2g_b)}{(1-g_b)}\sqrt{g_b}\ , \qquad g_b \equiv \left(\frac{V_{Sb}}{V_{Pb}}\right)^2 .$$

Because of the corrugation of fracture surfaces, the P-wave polarization vector deviates from the vertical, and the vertically propagating shear waves are no longer polarized in the horizontal plane. Equations 2.9 and 2.10, however, show that the shear-wave polarization vectors are still confined to the planes of the two fracture sets.[1]

Therefore, Alford-style rotation of the horizontal displacement components of near-offset S-wave reflections can be used to estimate the fracture azimuths. To measure the vertical components of the shear-wave polarization vectors, which are indicative of the

[1]Due to the limitations of the first-order perturbation theory, the shear-wave polarization vectors are no longer orthogonal, despite being perpendicular to the P-wave polarization vector. Also, the perturbed polarization vectors were not normalized; still, to the first order in the fracture weaknesses, the magnitude of the vectors $\mathbf{U}_P$, $\mathbf{U}_{S1}$ and $\mathbf{U}_{S2}$ is equal to unity.

presence of microcorrugated fractures, it is necessary to apply 3D polarization analysis.

2.4.2 Shear-Wave Splitting

The shear-wave splitting coefficient (γ^S) at vertical incidence is defined as (Thomsen, 1988; Tsvankin, 2001)

$$\gamma^S \equiv \frac{V_{S1}^2 - V_{S2}^2}{2V_{S2}^2}, \tag{2.11}$$

where V_{S1} is the velocity of the fast shear wave. Applying the second-order perturbation theory (Farra, 2001) and retaining terms quadratic in the fracture weaknesses, we find

$$\begin{aligned}\gamma^S =& \frac{1}{2}\Bigg\{ (\Delta_{V_1} - \Delta_{V_2})(1 + \Delta_{V_1} - \Delta_{V_2}) \\ & - g_b \left[(\Delta_{VH_1}^2 - \Delta_{VH_2}^2) + (\Delta_{NV_1}^2 - \Delta_{NV_2}^2) \frac{(3-4g_b)}{1-g_b} \right] \Bigg\}.\end{aligned} \tag{2.12}$$

As expected, γ^S at vertical incidence vanishes when the two fracture sets have identical weaknesses. If the terms quadratic in the weaknesses are dropped from equation 2.12, the splitting coefficient reduces to the difference between the diagonal tangential weaknesses Δ_{V_1} and Δ_{V_2} (see equations 2.6 and 2.7). Therefore, to the first order γ^S coincides with the splitting coefficient for rotationally invariant fractures, which is controlled by the difference between the fracture densities of the two sets (Thomsen, 1988; Bakulin et al., 2000a,b).

However, if the second-order terms are substantial, γ^S is also influenced by the off-diagonal weaknesses Δ_{VH_i} and Δ_{NV_i}. Note that the weakness Δ_{NV_i} depends on saturation and takes different values for fractures filled with compressible gas, brine, or oil (Bakulin et al., 2000c).[2] Therefore, the vertical-incidence splitting coefficient for microcorrugated fractures with relatively large off-diagonal weaknesses may serve as an indicator of fluid saturation.

As illustrated by Figure 2.3, the exact coefficient γ^S can vary by as much as 50% over the entire range of plausible values of Δ_{NV_1} (Δ_{NV_2} was fixed). We would like to emphasize that the exact γ^S (as well as the exact NMO ellipses below) is computed from the *exact* (not linearized) stiffness matrix for our model obtained using the linear-slip theory (see Appendix A). For a tight (non-porous) host rock, $\Delta_{NV_1} = 0$ corresponds to fractures filled with incompressible fluid such as brine, whereas nonzero values of Δ_{NV_1} describe fractures at least partially saturated with gas (Bakulin et al., 2000c). Although the weak-anisotropy approximation 2.12 correctly reproduces the overall character of the curve $\gamma^S(\Delta_{NV_1})$, it understimates the sensitivity of the shear splitting to the weakness Δ_{NV_1}.

[2]Equation 2.12 is more accurate than equation (30) of Bakulin et al. (2000c) because it includes all terms quadratic in the weaknesses.

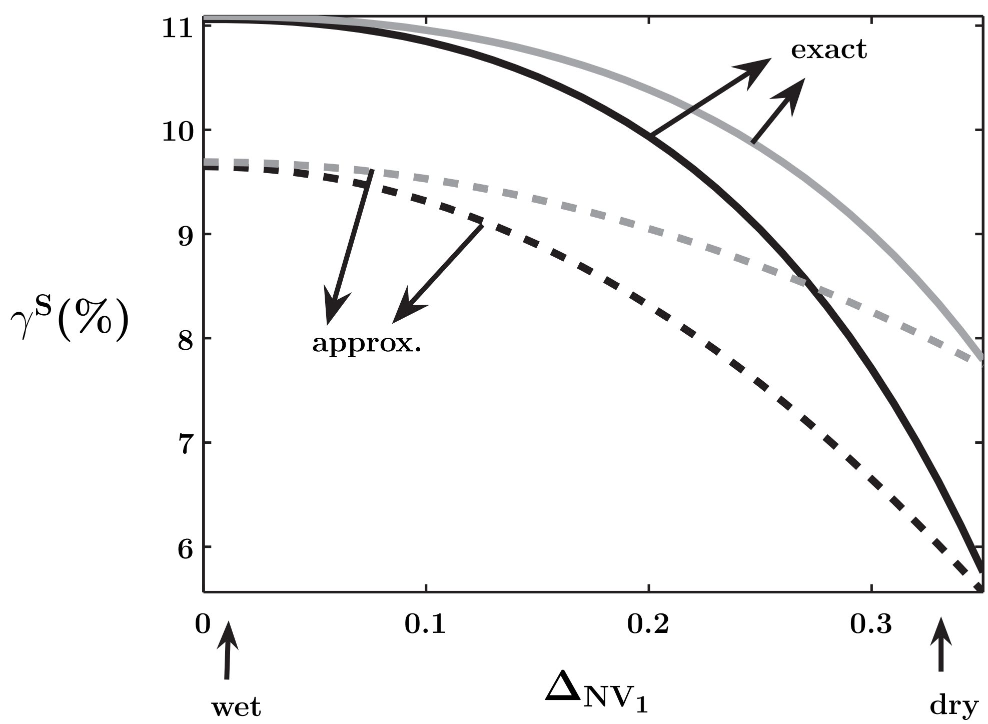

Figure 2.3. Variation of the shear-wave splitting coefficient (γ^S) for vertical propagation as a function of the weakness Δ_{NV_1} and the V_{Pb}/V_{Sb} ratio. The solid curves mark the exact γ^S from equation 2.11, where the velocities are computed from the Christoffel equation; the dashed curves are the approximation 2.12. The V_{Pb}/V_{Sb} ratio is equal to two (black lines) and three (gray). The other model parameters are $V_{Pb} = 3$ km/s, $\Delta_{N_1} = 0.5$, $\Delta_{V_1} = \Delta_{H_1} = 0.25$, and $\Delta_{NH_1} = \Delta_{VH_1} = 0.1$. Each weakness of the second fracture set except for Δ_{NV_2} is equal one-third of the corresponding weakness of the first set; $\Delta_{NV_2} = (1/3)\Delta_{NH_1}$.

If the saturation of both both fracture sets changes simultaneously and Δ_{NV_2} varies similarly to Δ_{NV_1}, the splitting coefficient becomes less sensitive to fluid content. Also, when the host rock has pore space hydraulically connected to the fractures, the weaknesses Δ_{NV_i} do not necessarily vanish even for incompressible saturating fluids (Cardona, 2002; Gurevich, 2003). As a consequence, for porous rocks the variation of γ^S with saturation may be less pronounced than that suggested by Figure 2.3. Finally, γ^S becomes less sensitive to the off-diagonal compliances and saturation for softer rocks (e.g., marine sediments) with smaller values of the ratio g_b , i.e., higher V_P/V_S ratios.

2.5 NMO Ellipses from Horizontal Reflectors

Important information for fracture detection is provided by azimuthally varying traveltimes (moveout) of reflected waves, in particular by their normal-moveout (NMO) ellipses. For a horizontal, homogeneous layer of arbitrary anisotropic symmetry, the NMO velocity of pure (non-converted) reflection modes as a function of the azimuth α is given by (Grechka et al., 1999):

$$V_{\text{nmo}}^{-2} = W_{11}\cos^2\alpha + 2W_{12}\sin\alpha\cos\alpha + W_{22}\sin^2\alpha\,, \tag{2.13}$$

where $\mathbf{W}$ is a symmetric 2×2 matrix,

$$\mathbf{W} = \frac{q}{q_{,12}^2 - q_{,11}q_{,22}}\begin{pmatrix} q_{,22} & -q_{,12} \\ -q_{,12} & q_{,11}\end{pmatrix}. \tag{2.14}$$

Here, q is the vertical component of the slowness vector $\mathbf{p} = [p_1, p_2, q]$ of the zero-offset ray and $q_{,ij}$ denote the following partial derivatives evaluated at zero offset:

$$q_{,ij} \equiv \frac{\partial^2 q(p_1,p_2)}{\partial p_i \partial p_j}\,. \tag{2.15}$$

The vertical slowness and its derivatives can be obtained from the Christoffel equation, as discussed by Grechka et al. (1999). If the eigenvalues of the matrix $\mathbf{W}$ are positive (the most typical case), equation 2.13 describes an ellipse in the horizontal plane.

To analyze the dependence of the NMO ellipses on the medium parameters, it is convenient to linearize equation 2.14 in the fracture weaknesses (equations B.1–B.6). For P-waves, the linearized matrix $\mathbf{W}$ takes the form

$$\mathbf{W}^P = \frac{1}{V_{Pb}^2}\begin{pmatrix} W_{11}^P & W_{12}^P \\ W_{12}^P & W_{22}^P\end{pmatrix}, \tag{2.16}$$

where

$$W_{11}^P = 1 + \Delta_{N_1}\left(1 - 4g_b^2\right) + \Delta_{N_2}\left(1 - 2g_b\right)^2 + 4g_b\,\Delta_{V_1}\,, \tag{2.17}$$

$$W_{12}^P = 2\left(\Delta_{NH1} + \Delta_{NH_2}\right)\left(1 - 2g_b\right)\sqrt{g_b}\,, \tag{2.18}$$

$$W_{22}^P = 1 + \Delta_{N_2}\left(1 - 4g_b^2\right) + \Delta_{N_1}\left(1 - 2g_b\right)^2 + 4g_b\,\Delta_{V_2}\,. \tag{2.19}$$

The structure of equations 2.17–2.19 can be understood from the "addition rule" formulated by Bakulin et al. (2000b). To find the linearized weak-anisotropy approximation for most seismic signatures (one exception is discussed below), the anisotropic terms due to each fracture set can be simply added together taking into account the fracture orientation. This recipe can be used to obtain equations 2.17–2.19 from the P-wave NMO ellipse for a single set of microcorrugated fractures given in equation (56) of Grechka et al. (2003).

For the fast shear wave S_1 the matrix $\mathbf{W}$ becomes

$$\mathbf{W}^{S1} = \frac{1}{V_{Sb}^2} \begin{pmatrix} W_{11}^{S1} & W_{12}^{S1} \\ W_{12}^{S1} & W_{22}^{S1} \end{pmatrix}, \tag{2.20}$$

with

$$W_{11}^{S1} = 1 + \Delta_{H_1} + \Delta_{H_2} - \mathcal{A}\,, \tag{2.21}$$

$$W_{12}^{S1} = \sqrt{g_b}\;(2\Delta_{NH_2} - \mathcal{C})\,, \tag{2.22}$$

$$W_{22}^{S1} = 1 - 3\Delta_{V_2} + 4g_b\,\Delta_{N_2} - \mathcal{B}\,. \tag{2.23}$$

Here,

$$\mathcal{A} \equiv \mathcal{D}\,\Delta_{VH_1}^2\,, \tag{2.24}$$

$$\mathcal{B} \equiv \mathcal{D}\,\Delta_{VH_2}^2\,, \tag{2.25}$$

$$\mathcal{C} \equiv \mathcal{D}\,\Delta_{VH_1}\,\Delta_{VH_2}\,, \tag{2.26}$$

and

$$\mathcal{D} \equiv \frac{g_b}{(\Delta_{V_1} - \Delta_{V_2})}\,. \tag{2.27}$$

Although the factors $\mathcal{A}$, $\mathcal{B}$, and $\mathcal{C}$ are proportional to products of the weaknesses Δ_{VH_i}, their denominator contains the difference in the tangential weaknesses Δ_{V_i} (see equation 2.27). For that reason, $\mathcal{A}$, $\mathcal{B}$, and $\mathcal{C}$ have to be retained in the linearized approximation for the NMO ellipse $\mathbf{W}^{S1}$. In such a case, the addition rule discussed above is not valid, and the approximate NMO ellipse of the S_1-wave cannot be obtained as the sum of the contributions of each fracture set.

The linearized matrix $\mathbf{W}$ for the S_2-wave is given by

$$\mathbf{W}^{S2} = \frac{1}{V_{Sb}^2} \begin{pmatrix} W_{11}^{S2} & W_{12}^{S2} \\ W_{12}^{S2} & W_{22}^{S2} \end{pmatrix}, \tag{2.28}$$

where

$$W_{11}^{S2} = 1 - 3\Delta_{V_1} + 4g_b\,\Delta_{N_1} + \mathcal{A}\,, \tag{2.29}$$

$$W_{12}^{S2} = \sqrt{g_b}\;(2\Delta_{NH_1} + \mathcal{C})\,, \tag{2.30}$$

$$W_{22}^{S2} = 1 + \Delta_{H_1} + \Delta_{H_2} + \mathcal{B}\,. \tag{2.31}$$

Equations 2.16–2.31 show that only the presence of the off-diagonal weaknesses can explain the misalignment of the NMO ellipses with the fracture planes. If both fracture sets were rotationally invariant, the matrices $\mathbf{W}$ for all three modes (equations 2.16, 2.20, and 2.28) would be diagonal, and the axes of the NMO ellipses would be parallel to the fracture strike directions. In an effective orthorhombic medium due to two orthogonal sets of rotationally invariant fractures, the semi-major axes of the NMO ellipses of the P- and S_1-waves (Figure 2.4) are aligned with the strike of the dominant fracture set (Bakulin et al., 2000b).

By contrast, when both fracture sets are microcorrugated, all three NMO ellipses generally have different orientations, and none of them is aligned with the fracture azimuths (Figure 2.5). The deviation of the semi-major axis of the NMO ellipse from the azimuth of the dominant fracture set reaches 30° for the P-wave and 20° for the S_1-wave. The weak-anisotropy approximations for the NMO ellipses are close to the exact solutions for the full range of azimuths (Figure 2.6). The error of the approximate solution, caused primarily by the misalignment of the axes of the exact and approximate NMO ellipses, is noticeable only for the slow shear wave S_2. The higher accuracy of the approximation for the S_1-wave compared to that for the S_2-wave is not surprising since equations 2.22 and 2.23 for the matrix elements W_{12}^{S1} and W_{22}^{S1} become exact for one set of fractures (Grechka et al., 2003).

The orientation of the NMO ellipse of the fast wave S_1 can help to distinguish between the models with one or two microcorrugated fracture sets. If the second set does not exist, then $\Delta_{NH_2} = \Delta_{VH_2} = 0$, and the element W_{12} for the S_1-wave vanishes (equations 2.22 and 2.26). In this case, the matrix $\mathbf{W}^{S1}$ (equation 2.20) becomes diagonal, and the semi-major axis of the NMO ellipse of the S_1-wave is parallel to both the fast shear-wave polarization direction (equation 2.9) and the fracture strike. Moreover, for the model with one set of microcorrugated fractures, both the S_1-wave vertical velocity and the NMO velocity in the fracture-strike direction coincide with the background velocity V_{Sb}. This result, discussed by Grechka et al. (2003), follows from equations 2.6, 2.20, and 2.23.

Grechka et al. (2000) defined the Thomsen-style parameters $\zeta^{(i)}$ $(i = 1, 2, 3)$ responsible for the orientations of the NMO ellipses of pure modes in a horizontal monoclinic layer with a horizontal symmetry plane. Equations 2.16–2.31 can be used to generalize their result for our triclinic model because the elements W_{12} include the parameters $\zeta^{(i)}$ and, for the shear waves, additional correction terms. Using equations B.21 and B.24, the element W_{12}^{P} (equation 2.18) responsible for the rotation of the P-wave NMO ellipse with respect to the x_1-axis can be represented as

$$W_{12}^{P} = -2\frac{c_{36}}{c_{33}} = -2\zeta^{(3)}\,, \tag{2.32}$$

which coincides with the expression for W_{12}^{P} in Grechka et al. (2000). For our model, the parameter $\zeta^{(3)}$ is proportional to the sum of the weaknesses Δ_{NH_1} and Δ_{NH_2}.

Similarly, the off-diagonal elements W_{12}^{S1} and W_{12}^{S2} for the S-waves (equations 2.22

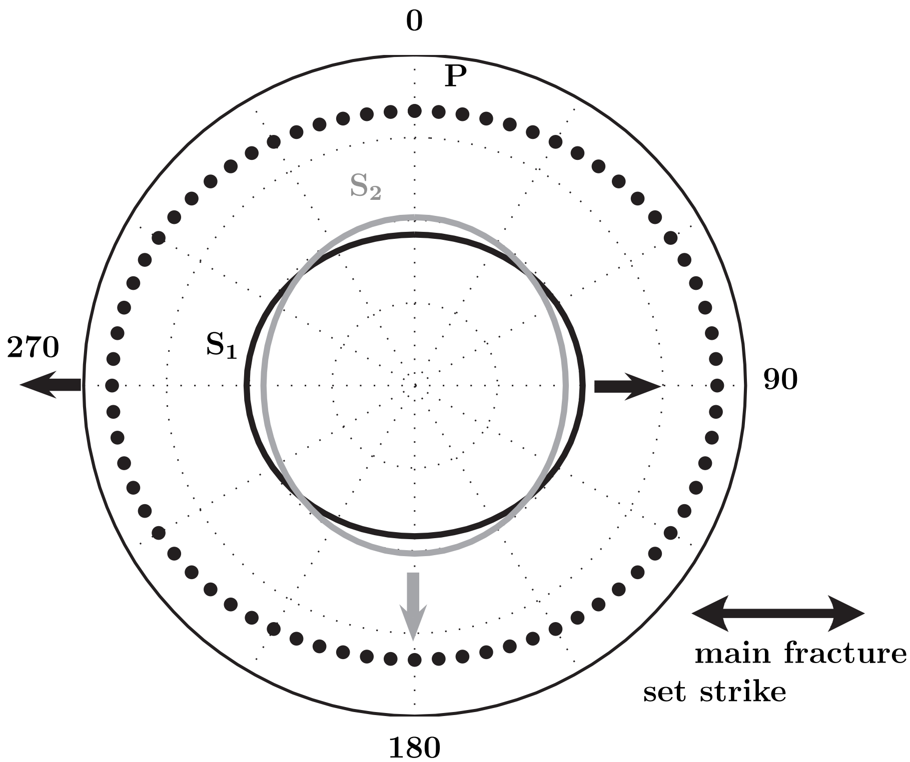

Figure 2.4. Exact NMO ellipses of P-waves (dotted), S_1-waves (solid black) and S_2-waves (solid gray) for an effective orthorhombic model formed by two vertical, orthogonal sets of rotationally invariant fractures. The semi-major axes (black arrows) of the P- and S_1-wave NMO ellipses are parallel to the strike of the dominant fractured set (azimuth 90°). The semi-major axis of S_2-wave ellipse (gray arrow) is orthogonal to the main fracture set. The parameters are $V_{Pb} = 2$ km/s, $V_{Sb} = 1$ km/s, $\Delta_{N_1} = 0.25$, and $\Delta_{V_1} = \Delta_{H_1} = 0.12$. Each weakness of the second fracture set is equal to one-third of the corresponding weakness of the first set. The radius of the external circle corresponds to 2 km/s.

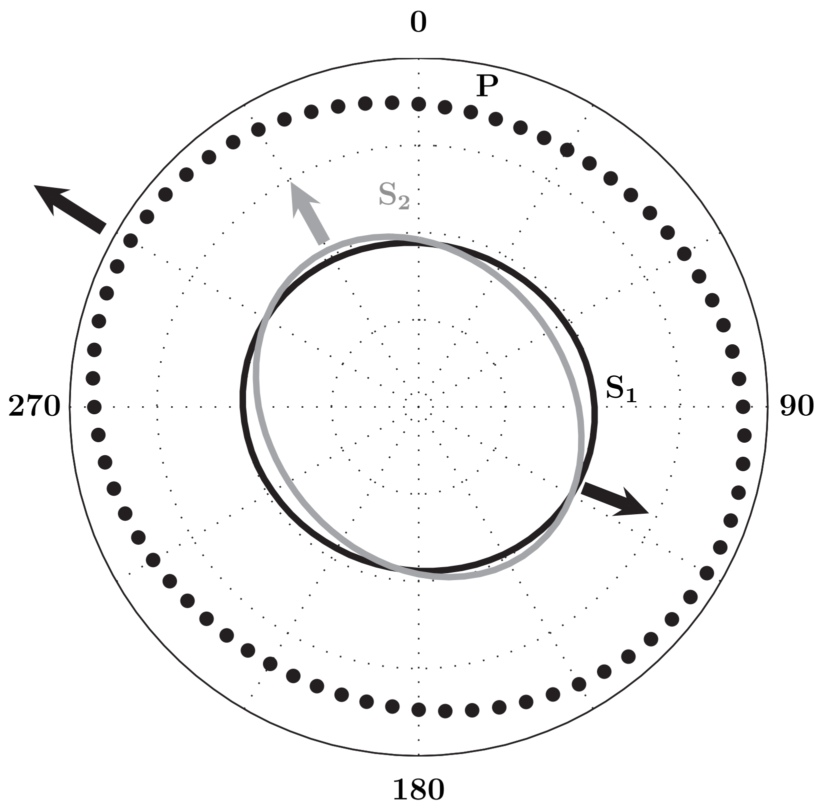

Figure 2.5. Exact NMO ellipses for two vertical, orthogonal sets of microcorrugated fractures. The strike azimuth of the dominant (first) fracture set is 90°. The parameters are V_{Pb}=2 km/s, V_{Sb}=1 km/s, $\Delta_{N_1} = 0.25$, $\Delta_{V_1} = \Delta_{H_1} = 0.12$, $\Delta_{NV_1} = \Delta_{NH_1} = 0.17$, and $\Delta_{VH_1} = 0.12$. Each weakness of the second fracture set is equal to one-third of the corresponding weakness of the first set.

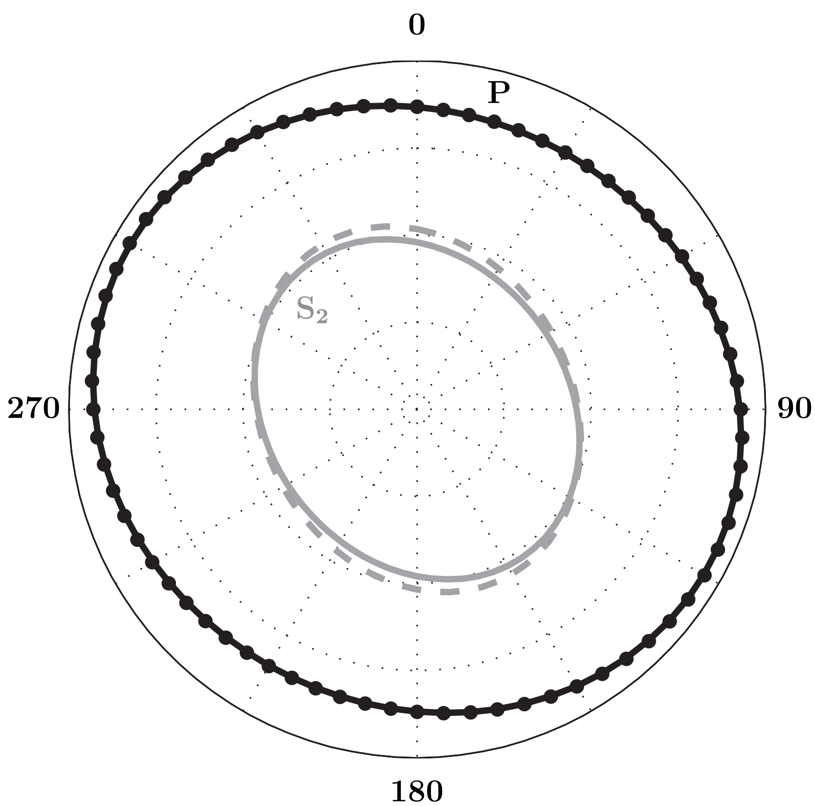

Figure 2.6. Comparison between the exact NMO ellipses of the P- and S_2-waves from Figure 2.5 (solid lines) and the weak-anisotropy approximations (dots for the P-wave and the dashed line for the S_2-wave). The approximations are computed from equations 2.17–2.19 and 2.29–2.31. The exact and approximate NMO ellipses of the S_1-wave (not shown) practically coincide with each other.

and 2.30) can be expressed through the parameters $\zeta^{(1)}$ and $\zeta^{(2)}$:

$$W_{12}^{S1} = -2\,\frac{c_{16} - c_{36}}{2V_{Pb}^2\, g_b} + \mathcal{C} = -2\frac{\zeta^{(1)}}{g_b} + \mathcal{C}\,, \tag{2.33}$$

$$W_{12}^{S2} = -2\,\frac{c_{26} - c_{36}}{2V_{Pb}^2\, g_b} - \mathcal{C} = -2\frac{\zeta^{(2)}}{g_b} - \mathcal{C}\,, \tag{2.34}$$

where $\mathcal{C}$ (equation 2.26) is an additional correction factor needed to account for the nonzero stiffnesses c_{46} and c_{56} in the triclinic model (equation 2.3). The parameters $\zeta^{(1)}$ and $\zeta^{(2)}$ depend on the weaknesses Δ_{NH_2} and Δ_{NH_1}, respectively.

Our approximations for the NMO ellipses of both S-waves break down when tangential weaknesses Δ_{V_1} and Δ_{V_2} are identical and the weaknesses $\Delta_{VH_i} \neq 0$. In this case, the parameter $\mathcal{D}$ (equation 2.27) goes to infinity, which reflects the fact that a point shear-wave singularity develops in a close vicinity of the zero-offset ray. Analysis of the influence of singularities on normal moveout for models with two orthogonal sets of penny-shaped cracks can be found in Bakulin et al. (2000b).

2.6 P-Wave Reflection Coefficient

Another seismic signature that can be effectively used in fracture detection is the azimuthally varying reflection coefficient, in particular the AVO (amplitude variation with offset) gradient responsible for small- and moderate-offset reflection amplitudes. Here, we present a linearized expression for the P-wave AVO response in our model and discuss its dependence on the fracture weaknesses.

We consider an isotropic incidence halfspace separated by a plane boundary from the triclinic medium described by equation 2.2 and assume a weak contrast in the elastic properties across the interface and weak anisotropy in the reflecting halfspace (i.e., the triclinic medium is treated as a perturbation of the incidence isotropic medium caused by small fracture weaknesses). The weak-contrast, weak-anisotropy approximation for the P-wave reflection coefficient in arbitrary anisotropic media is derived in Vavryčuk and Pšenčik (1998). By combining their general result with the linearized stiffness coefficients for our model (equations B.10–B.30), we find the P-wave reflection coefficient R_{PP} as a function of the phase incidence angle θ:

$$\begin{aligned} R_{PP} &= A + B\sin^2\theta + C\sin^2\theta\,\tan^2\theta \\ &= A_{\text{iso}} + A_{\text{ani}} + (B_{\text{iso}} + B_{\text{ani}})\sin^2\theta \;+\; (C_{\text{iso}} + C_{\text{ani}})\sin^2\theta\tan^2\theta\,. \end{aligned} \tag{2.35}$$

Here, A is the normal-incidence reflection coefficient (“AVO intercept”), B is the AVO gradient, and C is the so-called “curvature” (large-angle) term. In the weak-contrast, weak-anisotropy approximation, each term can be separated into the isotropic (subscript “iso”) and anisotropic (subscript “ani”) part. Since the isotropic part of the linearized reflection coefficient is well known (it is expressed through the background velocities and densities), we will discuss only the additional anisotropic terms. The anisotropic component of the

AVO intercept A is formed by the contribution of the normal fracture weaknesses to the P-wave vertical velocity in the fractured layer:

$$A_{\text{ani}} = -\,\frac{(\Delta_{N_1} + \Delta_{N_2})\,\chi^2}{4}\,. \tag{2.36}$$

The anisotropic part of the AVO gradient is given by

$$B_{\text{ani}}(\phi) = A_{\text{ani}} + B_1 \cos^2\phi + B_2 \sin 2\phi + B_3 \sin^2\phi\,, \tag{2.37}$$

where ϕ is the azimuthal phase angle measured from the x_1-axis, and

$$B_1 = g_b\big(\Delta_{V_1} - \Delta_{N_1}\chi\big)\,, \tag{2.38}$$

$$B_2 = -\frac{\chi\sqrt{g_b}}{2}\left(\Delta_{NH_1} + \Delta_{NH_2}\right)\,, \tag{2.39}$$

$$B_3 = g_b\big(\Delta_{V_2} - \Delta_{N_2}\chi\big). \tag{2.40}$$

The anisotropic curvature term is obtained as

$$\begin{aligned} C_{\text{ani}}(\phi) = {} & A_{\text{ani}} + C_1 \cos^4\phi + C_2 \sin^4\phi \\ & + \big(C_3\cos^2\phi + C_4 \sin 2\phi + C_5 \sin^2\phi\big)\sin 2\phi\,, \end{aligned} \tag{2.41}$$

with

$$C_1 = g_b\,(1 - g_b)\,\Delta_{N_1}, \tag{2.42}$$

$$C_2 = g_b\,(1 - g_b)\,\Delta_{N_2}, \tag{2.43}$$

$$C_3 = \frac{\sqrt{g_b}}{2}\big(\Delta_{NH_1} + \Delta_{NH_2}\chi\big), \tag{2.44}$$

$$C_4 = \frac{\sqrt{g_b}}{4}\big[\Delta_{H_1} + \Delta_{H_2} + (\Delta_{N_1} + \Delta_{N_2})\,\chi\big], \tag{2.45}$$

$$C_5 = \frac{\sqrt{g_b}}{2}\big(\Delta_{NH_1}\chi + \Delta_{NH_2}\big). \tag{2.46}$$

There are interesting similarities between equations 2.37–2.46 and equations 2.16–2.19 for the P-wave NMO ellipse. First, if the sign of the AVO gradient does not change with azimuth, $|B_{\text{ani}}(\phi)|$ plotted as the radius-vector traces out a curve close to an ellipse in the horizontal plane, with $B_{\text{ani}}^{-2}(\phi)$ being exactly elliptical. (Note that the shape of the azimuthally varying curvature term is more complicated and is not represented by a quadratic function in the horizontal coordinates.) Second, the only off-diagonal weaknesses appearing in the linearized equations for both the reflection coefficient and NMO ellipse are Δ_{NH_1} and Δ_{NH_2}. Third, the "principal directions" of the curve $|B_{\text{ani}}(\phi)|$ are are rotated with respect to the horizontal coordinate axes (i.e., with respect to the fracture azimuths) only when $\Delta_{NH_1} \neq 0$ or $\Delta_{NH_2} \neq 0$. Furthermore, the rotation angle of both the NMO ellipse (equation 2.18) and AVO gradient (equation 2.39) is controlled by the sum $\Delta_{NH_1} + \Delta_{NH_2}$. As shown above, the rotation angle can be also expressed through the anisotropy coefficient

$\zeta^{(3)}$ (equation 2.32).

The example in Figure 2.7 illustrates the orientation and shape of the magnitude of the azimuthally varying AVO gradient from equation 2.37. The curve $|B_{\text{ani}}(\phi)|$ ($B_{\text{ani}} < 0$) is close to an ellipse with the semi-major axis deviating by about 55° from the strike of the dominant fracture set. If the weaknesses Δ_{NH_1} and Δ_{NH_2} are set to zero, the direction of the largest (by absolute value) AVO gradient is perpendicular to the dominant fracture set.

Despite the small value of $\Delta_{NH_1} = 0.05$, the contribution of the off-diagonal weaknesses is sufficient for rotating this direction by about 35°. This high sensitivity of the orientation of the AVO-gradient curve to the off-diagonal terms is explained by equations 2.38–2.40. While the element B_2 is a weighted average of the weaknesses Δ_{NH_j} ($j = 1, 2$), the coefficients B_1 and B_3 are proportional to the difference $\Delta_{V_i} - \Delta_{N_i}\chi$. Since for our model this difference is small, it does not take large off-diagonal weaknesses to cause a significant rotation of the AVO gradient.

2.7 Discussion and Conclusions

We studied seismic signatures of an effective medium formed by two sets of vertical, orthogonal fractures with microcorrugated surfaces embedded in isotropic host rock. Each fracture set is described by the most general compliance matrix allowed within the framework of the linear-slip theory, with the off-diagonal compliance elements responsible for the character and degree of corrugation. The effective model is triclinic and has no symmetry planes, although only 15 stiffness elements are independent.

By applying expansions in the fracture weaknesses (normalized compliances), we derived closed-form analytic expressions for shear-wave splitting, the NMO ellipses of horizontal reflection events, and the P-wave reflection coefficient. These weak-anisotropy approximations provide valuable insight into the influence of the fracture rheology on seismic signatures commonly used in reservoir characterization. For instance, the presence of the off-diagonal weaknesses makes the shear-wave splitting coefficient γ^S at vertical incidence sensitive (to the second order) to fluid saturation. The variation of γ^S with saturation may be substantial in tight, high-velocity formations where fluids cannot easily move from the fractures into pore space.

The fracture weaknesses also control the orientation and eccentricity of the NMO ellipses of the reflected P-, S_1, and S_2-waves. In particular, the contributions of the off-diagonal weaknesses Δ_{NH_i} and Δ_{VH_i} ($i = 1, 2$) lead to the rotation of the NMO ellipses with respect to the fracture strike directions. In contrast to the effective orthorhombic medium formed by two orthogonal sets of penny-shaped cracks, all three NMO ellipses in our model have different orientations. Extending existing results for monoclinic models, we expressed the rotation angles of the NMO ellipses in triclinic media through the anisotropy parameters $\zeta^{(1)}$, $\zeta^{(2)}$, and $\zeta^{(3)}$.

Analysis of the NMO ellipse of the fast shear wave S_1 suggests a simple way to distinguish between models with one and two microcorrugated fracture sets. For a single set of fractures, the semi-major axis of the S_1-wave NMO ellipse and the polarization vector of the S_1-wave at vertical incidence are parallel to each other and to the fracture strike.

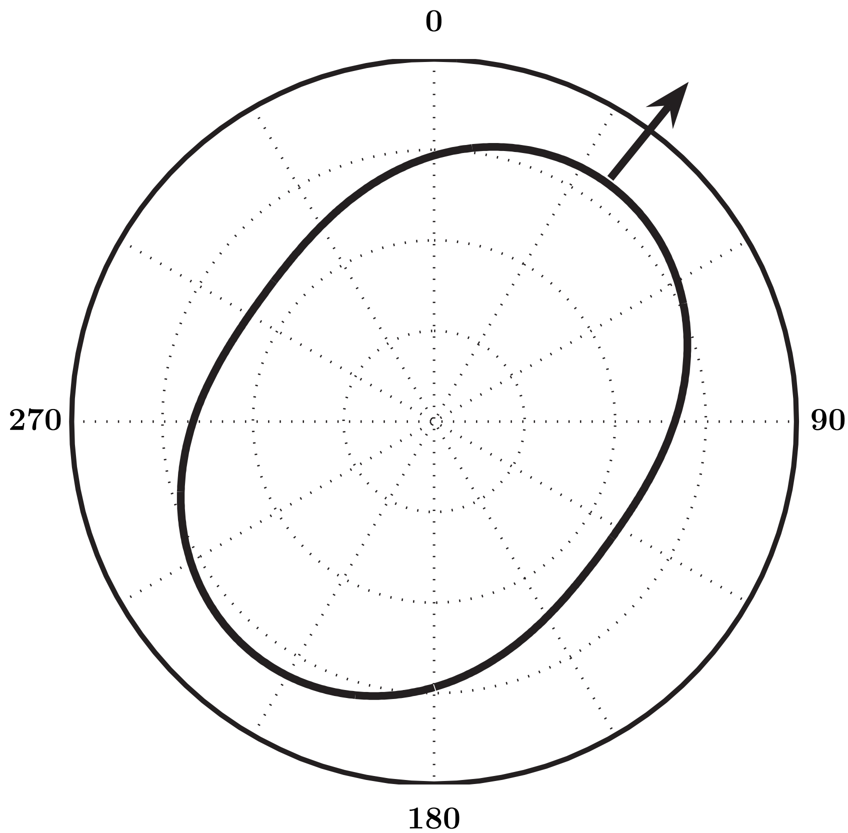

Figure 2.7. Azimuthal variation of the absolute value of the P-wave AVO gradient for our triclinic model computed from equation 2.37. The strike azimuth of the dominant fracture set is 90°; the direction of the largest gradient (black arrow) is close to 35°. The parameters are $V_{Pb}/V_{Sb} = 3$, $\Delta_{N_1} = 0.25$, $\Delta_{V_1} = \Delta_{H_1} = 0.12$, and $\Delta_{NH_1} = 0.05$. Each weakness of the second fracture set is equal to one-third of the corresponding weakness of the first set.

This is no longer the case for the model with two fracture sets where the angle between the polarization vector and the semi-major axis of the NMO ellipse for the S_1-wave can reach 20-30°.

For P-waves, the principal azimuthal directions of both the NMO ellipse and AVO gradient depend on the sum of the off-diagonal weaknesses Δ_{NH_1} and Δ_{NH_2}. If both Δ_{NH_1} and Δ_{NH_2} vanish, then the NMO ellipse and AVO gradient are aligned with the fracture strike directions, as is always the case for penny-shaped cracks. Whereas the azimuthally varying P-wave AVO gradient traces out a quasi-elliptical curve (if it does not change sign with azimuth), the large-angle AVO term has a much more complicated azimuthal dependence.

The results of this work can be instrumental in developing inversion algorithms for estimating the fracture parameters from multicomponent seismic data. Unfortunately, it has been shown that the inversion for all 15 independent parameters of this model is ill-posed. Even if all 21 elastic constants of the triclinic medium are recovered with high accuracy, it is impossible to resolve the fracture weaknesses individually. The equations presented here, however, can help to estimate certain parameter combinations and verify whether the underlying physical model is appropriate. Lack of data on the magnitude of the off-diagonal weaknesses for natural fracture networks makes such experimental studies particularly important.

As discussed above, comparison of the NMO ellipse and polarization direction of the S_1-wave makes it possible to discriminate between the effective models with one and two sets of microcorrugated fractures. Our results also indicate that it may be possible to invert seismic data for the velocity ratio g_b and the differences between the diagonal weaknesses Δ_{N_i}, Δ_{V_i} and Δ_{H_i} of the two sets, if the vertical velocities are available. Also, the P-wave ellipses and AVO gradient can potentially constrain the sum of the off-diagonal weaknesses Δ_{NH_i}.

The weaknesses Δ_{NV_i} do not appear in the linearized equations for any of the NMO ellipses or for the P-wave AVO gradient and contribute only to the second-order term in the shear-wave splitting coefficient. The only quantities that contain first-order contributions of Δ_{NV_i} are the vertical components of the S-wave polarization vectors, which may be difficult to measure on field data. Likewise, the weaknesses Δ_{VH_i} are contained only in relatively small terms in the equations for the shear-wave NMO ellipses and for the splitting coefficient γ^S. Therefore, estimation of the weaknesses Δ_{VH_i} and Δ_{NV_i} is likely to be unstable. For a single microcorrugated fracture set, both Δ_{VH} and Δ_{NV} can be determined from VSP data using the slowness surface of P-waves. It is not clear, however, if such an algorithm can be extended to the more complicated model treated here.

2.8 Acknowledgments

We are grateful to members of the A(nisotropy)-Team of the Center for Wave Phenomena (CWP) at Colorado School of Mines (CSM) for helpful discussions and to Tom Davis and Ken Larner (both CSM) for their reviews of the manuscript. Rodrigo Fuck's graduate studies at CSM were funded by the Brazilian government through CAPES under the scholarship BEX1340-0/00. This work was also supported by the Consortium Project on Seismic Inverse Methods for Complex Structures at CWP and by the Chemical Sciences, Geosciences and Biosciences Division, Office of Basic Energy Sciences, U.S. Department of Energy.

Chapter 3

Theory of traveltime shifts around compacting reservoirs: 3D solutions for heterogeneous anisotropic media

3.1 Summary

Time-lapse traveltime shifts of reflection events recorded above hydrocarbon reservoirs can be used to monitor production-related compaction and pore-pressure changes. Existing methodology, however, is limited to zero-offset rays and cannot be applied to traveltime shifts measured on prestack seismic data. Here, we give an analytic 3D description of stress-related traveltime shifts for rays propagating along arbitrary trajectories in heterogeneous anisotropic media.

The nonlinear theory of elasticity helps to express the velocity changes in and around the reservoir through the excess stresses associated with reservoir compaction. Since this stress-induced velocity field is both heterogeneous and anisotropic, it should be studied using prestack traveltimes or amplitudes. Then we obtain the traveltime shifts by first-order perturbation of traveltimes that accounts not only for the velocity changes, but also for 3D deformation of reflectors. The resulting closed-form expression can be efficiently used for numerical modeling of traveltime shifts and, ultimately, for reconstructing the stress distribution around compacting reservoirs.

The analytic results are applied to a 2D model of a compacting rectangular reservoir embedded in an initially homogeneous and isotropic medium. The computed velocity changes around the reservoir are primarily caused by deviatoric stresses and produce a transversely isotropic medium with a variable orientation of the symmetry axis and substantial values of the Thomsen parameters ϵ and δ. The offset dependence of the traveltime shifts should play a crucial role in estimating the anisotropy parameters and the compaction-related deviatoric stress components.

3.2 Introduction

Traveltime shifts (differences), measured between two or more time-lapse seismic reflection surveys, have become an important tool for dynamic reservoir characterization. Production-related pore-pressure changes and compaction inside the reservoir cause accumulation of stress throughout the section. This excess stress modifies the elastic properties of rocks inside and around the reservoir, and the corresponding velocity changes can be estimated using reflection traveltimes recorded in time-lapse surveys. Analysis of traveltime shifts can help to map compaction throughout a reservoir and, therefore, optimize infill drilling and hydrocarbon production by identifying compartments and pressure cells inside the producing units.

The stress dependence of traveltime shifts is well understood for vertically propagating waves and horizontal layers (i.e., for zero-offset data). Traveltime shifts estimated on stacked seismic data from horizontally layered media have been successfully used to delineate compartments in reservoirs (e.g., Landrø and Stammeijer, 2004; Hatchell and Bourne, 2005b). However, this theory breaks down in the presence of dip and cannot be applied to prestack data, as demonstrated by data from South Arne field in the North Sea (Herwanger et al., 2007). Offset-dependent traveltimes shifts were analyzed by Røste et al. (2006), but their theory is restricted to horizontally layered isotropic media. Herwanger et al. (2007) used nonlinear elasticity to model the offset variation of traveltime shifts, but they do not present explicit expressions relating shifts to the stress field.

Here we provide an analytic 3D description of traveltime shifts around a compacting reservoir embedded in a heterogeneous, layered, anisotropic medium. Taking heterogeneity and anisotropy into account is necessary for an adequate physical description of traveltime shifts. Indeed, the excess stress field created by compaction is anisotropic (in general, it is triaxial) and heterogeneous because the magnitude of stress depends on reservoir geometry and varies spatially around the reservoir.

Our analysis of traveltimes shifts in and around a compacting reservoir involves two main steps. We start by expressing the velocity changes through the excess stress and strain fields created by the compaction. Then the first-order perturbation of traveltimes is used to obtain a linearized analytic approximation for the traveltime shifts. To describe stress-related velocity changes, we apply the nonlinear theory of elasticity (e.g., Thurston and Brugger, 1964a), which has several advantages over more conventional approaches to model stress-sensitivity of velocity fields. First, it does not rely on a specific micromechanical model and, therefore, is more general than approaches based on stiffening of grain contacts and closing or opening of specific micro-crack distributions (Shapiro and Kaselow, 2005). Second, nonlinear elasticity yields the full stiffness tensor of the deformed medium needed to compute traveltimes and other signatures for arbitrarily anisotropic media. Third, all possible mechanisms of stress sensitivity are absorbed by a small number of third-order elastic coefficients. For instance, an isotropic third-order strain-sensitivity tensor is completely defined by three parameters. In contrast, fracture models include at least two sets of penny-shape fractures, with each set defined by three parameters. Fourth, third-order elastic coefficients can be directly measured in laboratory or wellbore experiments (e.g, Sinha and Plona, 2001), whereas the fracture weaknesses have to be inverted from field data (Sayers, 2006).

The nonlinear theory has been successfully applied to estimate stress-induced anisotropy and the corresponding stress-sensitivity (or strain-sensitivity) tensor in sandstones and shales. Examples include ultrasonic velocity experiments on rock samples (Johnson and Rasolofosaon, 1996; Sarkar et al., 2003; Prioul et al., 2004) and in-situ stress estimation in boreholes (Winkler et al., 1998; Sinha and Plona, 2001). Unfortunately, measurements of third-order elastic coefficients (which represent elements of a sixth-rank tensor) for sedimentary rocks are rare, with most existing results obtained for crystals and man-made materials. This is an inherent limitation of our approach, but we expect more data to be available in the near-future, in particular because of the straightforward way of measuring third-order coefficients in the laboratory or boreholes. Also, the results by Prioul et al. (2004) indicate that detailed knowledge of the sixth-order elasticity tensor is not critical, and for most applications in exploration and reservoir geophysics that tensor can be assumed to be isotropic.

We start by describing the variational problem related to the first-order perturbation of traveltimes. Then perturbation theory and nonlinear elasticity are used to express traveltime shifts in terms of the excess stresses and volumetric strains caused by reservoir compaction. Synthetic tests for a 2D reservoir model confirm that the stress-induced velocity field is anisotropic and illustrate the offset dependence of traveltime shifts for reflectors above and below the reservoir.

3.3 P-Wave Traveltime Shifts from First Principles

Assuming that reservoir compaction produces only small changes in the traveltimes of seismic waves propagating through the medium, such traveltime shifts can be expressed through small perturbations of the model parameters. The deformation caused by compaction changes the relative positions of the boundaries between layers, while the extra stress alters the elastic properties. Therefore, traveltime shifts depend on the perturbations of the geometry of the medium interfaces and the elastic (stiffness) moduli.

To obtain first-order traveltime perturbations, we apply Hamilton's principle of least action to traveltimes computed for rays traced in an unperturbed background medium. For simplicity, we consider this background medium to be isotropic, with smoothly varying velocity and density, and restrict the analysis to P-waves. Then the traveltime shifts δt are described by the following equation well known in classical mechanics (e.g., Lanczos, 1986) (Appendix C):

$$\delta t = \mathbf{p} \cdot \delta\mathbf{x}\Big|_{\tau_1}^{\tau_2} - \int_{\tau_1}^{\tau_2} \Delta\mathcal{H}\,\mathrm{d}\tau\,, \tag{3.1}$$

where $\mathbf{p}$ is the slowness vector of the reference ray traced in the background medium, $\delta\mathbf{x}$ is the first-order variation of the position vector of the reference ray in 3D Cartesian coordinates, $\Delta\mathcal{H}$ is the corresponding variation of the system's Hamiltonian and τ is the integration parameter along the reference ray. The Hamiltonian $\mathcal{H}$ of the system is the scaled Eikonal equation, in which the integration parameter τ represents the traveltime along the reference ray (e.g., Červený, 2001):

$$\mathcal{H}(\mathbf{x},\mathbf{p}) = \frac{1}{2}\left[V^2(\mathbf{x},\mathbf{p})\,p_k\,p_k - 1\right] = 0\,, \tag{3.2}$$

where $V(\mathbf{x},\mathbf{p})$ is the phase velocity; summation over repeated indices is implied throughout the paper.

Equation 3.1 provides important insights into the nature of the traveltime shifts caused by reservoir compaction. First, in the linear approximation the contributions of the geometric and velocity changes to traveltimes are independent. Second, the changes of the ray trajectory (i.e., geometric changes) contained in the term $\mathbf{p} \cdot \delta\mathbf{x}$ do not contribute to first-order traveltime perturbations, unless they occur at the endpoints. Third, the influence of the velocity changes is represented by the perturbed Hamiltonian $\Delta\mathcal{H}$, which should be integrated along the reference ray.

3.3.1 Traveltime Shifts in Layered Media

Equation 3.1 is designed for rays traced in smoothly heterogeneous media (Figure 3.1a). If the medium is stratified, it is necessary to account for deformation of the reflectors that move the reflection/transmission points along the ray. This can be done by dividing the reference ray into segments, applying equation 3.1 to each of them and then summing up the results (Farra and Le Bégat, 1995). For the ray in Figure 3.1b, equation 3.1 is applied to segments **SA**, **AB**, **BC**, and **CR** separately, with subsequent summation of the individual contributions. Therefore, extension of equation 3.1 to layered media accounts for the movement of all N scattering (reflection/transmission) points along the raypath:

$$\delta t^i = (\grave{\mathbf{p}} - \acute{\mathbf{p}})^i \cdot \delta\mathbf{x}^i \quad (i = 1, 2, ...N), \tag{3.3}$$

where $\grave{\mathbf{p}}$ and $\acute{\mathbf{p}}$ are the slowness vectors of the incident and scattered (reflected or transmitted) rays, respectively. Note that each scattering point i belongs to two ray segments. By separating the contribution of the endpoints (δt^e) from that of the scattering points ($i = 1, 2, ...N$), equation 3.1 can be generalized for any number of layers arbitrarily deformed in 3D space:

$$\delta t = \delta t^e + \sum_{i=1}^{N} \delta t^i - \int_{\tau_1}^{\tau_2} \Delta\mathcal{H} d\tau \,, \tag{3.4}$$

where

$$\delta t^e = \mathbf{p} \cdot \delta\mathbf{x}\Big|_{\tau_1}^{\tau_2}, \quad \delta t^i = (\grave{\mathbf{p}} - \acute{\mathbf{p}}) \cdot \delta\mathbf{x} \,. \tag{3.5}$$

Equation 3.4 can be further simplified by taking Snell's law into consideration. Since the projection of the slowness vector onto the interface is conserved, the only nonzero component of vector $(\grave{\mathbf{p}} - \acute{\mathbf{p}})$ is that orthogonal to the interfaces. If layer boundaries are horizontal, the traveltime shifts depend just on the vertical components of the vector $(\grave{\mathbf{p}} - \acute{\mathbf{p}})$. For interfaces with arbitrary orientation, the unit normal vector (i.e., the vector perpendicular to the interface) at the reflection/transmission point $\mathbf{x}$ is given by the gradient of the unperturbed interface $f(\mathbf{x}) = 0$:

$$\mathbf{N}(\mathbf{x}) = \frac{\nabla f(\mathbf{x})}{|\nabla f(\mathbf{x})|} \,. \tag{3.6}$$

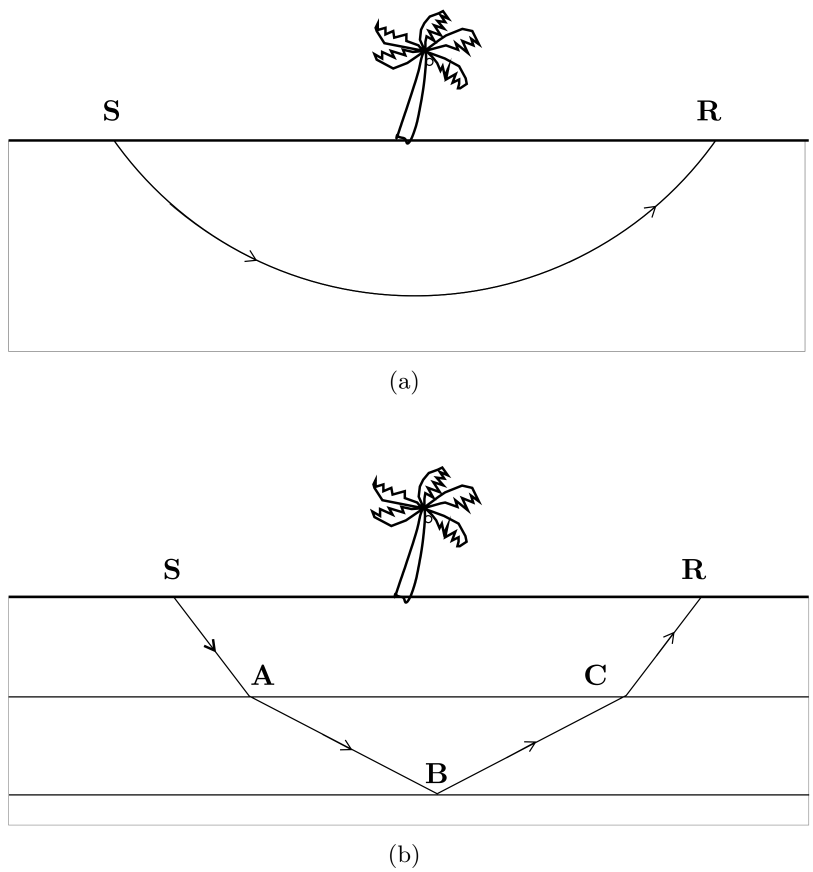

Figure 3.1. Equation 3.1 is valid for rays traced in a smoothly heterogeneous medium (plot a). For layered media (plot b), it is necessary to account for the movement of reflection (B) and transmission (A,C) points (see equation 3.4).

To find the component of the vector $\grave{\mathbf{p}} - \acute{\mathbf{p}}$ in the direction of $\mathbf{N}(\mathbf{x})$, we use the projection operator $\mathbf{A}(\mathbf{x})$:

$$\mathbf{A} = \frac{\mathbf{N}\mathbf{N}^{\mathsf{T}}}{\mathbf{N}^{\mathsf{T}}\mathbf{N}}\,. \tag{3.7}$$

Applying equation 3.7 to each term $(\grave{\mathbf{p}} - \acute{\mathbf{p}}) \cdot \delta\mathbf{x}$ in equation 3.4 gives

$$(\grave{p}_i - \acute{p}_i)\,\delta x_i = A_{ij}\,(\grave{p}_j - \acute{p}_j)\,\delta x_i\,. \tag{3.8}$$

3.3.2 Traveltime Shifts in Heterogeneous Anisotropic Media

As discussed above, reservoir compaction causes the velocity field around the reservoir to become both heterogeneous and anisotropic. Note that equation 3.1 involves no assumptions regarding the heterogeneity or anisotropy of the Hamiltonian or its perturbation $\Delta\mathcal{H}$. The generality of equation 3.1 helps to construct ray-tracing solutions for heterogeneous, arbitrarily anisotropic media (e.g., Jech and Pšenčik, 1989; Chapman and Pratt, 1992; Červený, 2001). The perturbation $\Delta\mathcal{H} = \Delta V/V$ is obtained from equation 3.2 for the reference ray with the components p_i held constant. Perturbing the Christoffel equation for P-waves leads to the following expression for the term ΔV under the assumption that reference rays are traced in an isotropic medium (Červený, 2001):

$$\Delta\mathcal{H} = \frac{1}{2}\,\frac{\Delta a_{ijkl}(\mathbf{x})\,n_i n_j n_k n_l}{V^2(\mathbf{x})}\,, \tag{3.9}$$

where Δa_{ijkl} are the perturbations of the density-normalized stiffness coefficients, and n_i are the components of the unit slowness vector.

3.4 Relating Velocity Changes to Excess Stresses

Equations 3.4 and 3.9 provide the basis for analytic description of compaction-induced traveltime shifts. The next step is to express the density-normalized stiffnesses Δa_{ijkl} in terms of the strains and excess stresses caused by reservoir compaction. As discussed in the introduction, we apply the nonlinear theory of elasticity to describe the stress sensitivity of the stiffness coefficients. The two main assumptions used here are that the strain-sensitivity tensor is isotropic and stress-induced anisotropy is weak.

3.4.1 Nonlinear Elasticity

According to Prioul et al. (2004), the effective stiffness coefficients c_{ijkl} of an elastic medium deformed under stress can be written in terms of the pre-deformation stiffnesses (c^0_{ijkl}) and the deformation-induced changes of the stress (ΔS_{ij}) and strain (Δe_{ij}) tensors:

$$\begin{aligned} c_{ijkl} =& c^0_{ijkl} + \Delta S_{ik}\delta_{jl} + c_{ijklmn}\,\Delta e_{mn} \\ &+ c^0_{ijpl}\,\Delta e_{kp} + c^0_{ipkl}\,\Delta e_{jp}\,, \end{aligned} \tag{3.10}$$

where δ_{ij} is Kronecker's symbol and c_{ijklmn} is a sixth-rank tensor with no more than 56 independent elements (Hearmon, 1953)[1]. Provided that deformation is small and elastic, equation 3.10 represents a suitable local linear approximation for the changes in the stiffness elements, similar to a Taylor series expansion around c^0_{ijkl}. We reduce the number of independent components of c_{ijklmn} to three by assuming that this tensor is isotropic, as suggested by Prioul et al. (2004).

For typical magnitudes of compaction-related stress changes (from 2–10 MPa inside the reservoir and one-tenth of that outside), equation 3.10 can be simplified further by dropping relatively small terms. Indeed, laboratory measurements have shown that typically $\Delta S_{ij} \ll c_{ijkl} \ll c_{ijklmn}$ (e.g., Johnson and Rasolofosaon, 1996), which allows us to neglect the terms $\Delta S_{ik}\delta_{jl}$, $c^0_{ijpl}\Delta e_{kp}$ and $c^0_{ipkl}\Delta e_{jp}$ in equation 3.10 (Prioul et al., 2004):

$$c_{ijkl} \approx c^0_{ijkl} + c_{ijklmn}\,\Delta e_{mn}\,. \tag{3.11}$$

Equation 3.11 shows that the tensor c_{ijklmn} is a measure of the sensitivity of the stiffnesses c_{ijkl} to deformation. Indeed, the definition of c_{ijklmn} in terms of the strain-energy function W (e.g., Hearmon, 1953) corroborates equation 3.11:

$$c_{ijklmn} \equiv \frac{\partial^3 W}{\partial e_{ij}\partial e_{kl}\partial e_{mn}} = \frac{\partial c_{ijkl}}{\partial e_{mn}}\,. \tag{3.12}$$

If the medium density ρ is assumed to be constant, equation 3.11 yields the changes in the density-normalized stiffnesses Δa_{ijkl} needed in equation 3.9:

$$\Delta a_{ijkl} = \rho^{-1}\frac{\partial c_{ijkl}}{\partial e_{mn}}\,\Delta e_{mn} = \rho^{-1} c_{ijklmn}\,\Delta e_{mn}\,. \tag{3.13}$$

Evaluation of the term $c_{ijklmn}\,\Delta e_{mn}$ is discussed in Appendix D. In the first-order approximation, we can follow Sarkar et al. (2003) and employ linear Hooke's law to relate Δe_{ij} to ΔS_{ij}:

$$\Delta a_{ijkl} = \rho^{-1} c_{ijklmn}\left(c^0_{mnpq}\right)^{-1}\Delta S_{pq}\,. \tag{3.14}$$

3.4.2 Traveltime Shifts Due to Compaction

A concise expression for traveltime shifts can be derived by substituting equation 3.14 into equation 3.9 for the perturbation of the Hamiltonian. Using the results of Appendix E (equation E.8), we find:

$$\Delta\mathcal{H} = \frac{1}{2}\left[B_1\Delta e_{kk} + B_2\left(\mathbf{n}^{\mathsf{T}}\Delta\sigma\,\mathbf{n}\right)\right], \tag{3.15}$$

[1]The qualifier "nonlinear" comes from the inclusion of the tensor c_{ijklmn} into Hooke's law (Thurston and Brugger, 1964a).

$$B_1 = \frac{1}{3C_{33}^o}\left(C_{111} + 2C_{112}\right), \quad B_2 = 2\,\frac{C_{155}}{C_{33}^0 C_{44}^0}\,, \tag{3.16}$$

where Δe_{kk} is the trace of the strain tensor and $\Delta\sigma$ is the tensor of deviatoric stress. The constants C_{111}, C_{112} and C_{155} are elements of the isotropic sixth-order tensor c_{ijklmn} written in Voigt notation, while C_{33}^0 and C_{44}^0 are the stiffnesses of the background isotropic medium. The traveltime shifts given by equation 3.4 can then be rewritten as

$$\delta t = \underbrace{\delta t^e + \sum_{i=1}^{N} \delta t^i}_{geom} - \underbrace{\frac{1}{2}\int_{\tau_1}^{\tau_2} \left[B_1 \Delta e_{kk} + B_2 \left(\mathbf{n}^\mathsf{T} \Delta\sigma\, \mathbf{n}\right)\right] \mathrm{d}\tau}_{vel}\,, \tag{3.17}$$

where “geom” and “vel” refer to the contributions of the geometric and velocity changes.

Except for possible influence of tides on offshore 4D surveys, typically, the “geometric” term is relatively small. Indeed, for the geometric changes to produce a traveltime shift of at least 1 ms, an unlikely set of conditions have to take place: the displacements should be on the order of meters; for layered models, the slowness contrasts cannot be smaller than 10^{-2} s/km; and summation should include from 10 to 100 scattering points. When elastic deformation is caused by depletion, however, displacements throughout the section are on the order of centimeters, consistent with the annual subsidence rates observed in fields like Valhall (Herwanger and Horne, 2005). In addition, for layered models there is little room to increase the number of reflection/transmission points without reducing the slowness contrasts.

According to equation 3.17, the velocity-related traveltime shifts are given by the arithmetic average of the isotropic ($B_1 \Delta e_{kk}$) and anisotropic ($B_2\, \mathbf{n}^\mathsf{T} \Delta\sigma\, \mathbf{n}$) terms computed along the raypath. In our sign convention, negative strains denote contraction, while positive strains denote extension. (Likewise, negative stresses imply compression.) This means that the coefficient C_{155} and the combination $C_{111} + 2C_{112}$ should be negative. Then, according to equations 3.15–3.17, compression leads to increase in velocity, which results in negative traveltime shifts. In contrast, traveltime shifts due to extension are positive.

To clarify how equation 3.17 generalizes existing results, in Appendix F it is reduced to the equation for zero-offset data from Hatchell and Bourne (2005b). In addition to extending the results of Hatchell and Bourne (2005b) to nonzero offsets and dipping reflectors, equation 3.17 provides useful insight into the meaning of different terms. The result of Hatchell and Bourne (2005b) for two-way traveltimes shifts has the form

$$\delta t = 2\int_0^Z (1 + R)\,\frac{\Delta e_{zz}}{V(z)}\,\mathrm{d}z\,. \tag{3.18}$$

According to equation 3.17, the ratio R from equation 3.18 can be written as

$$\delta t = 2\int_0^Z \left[1 + \frac{1}{2}\left(R_1 + R_2\right)\right] \frac{\Delta e_{zz}}{V(z)}\,\mathrm{d}z\,,$$

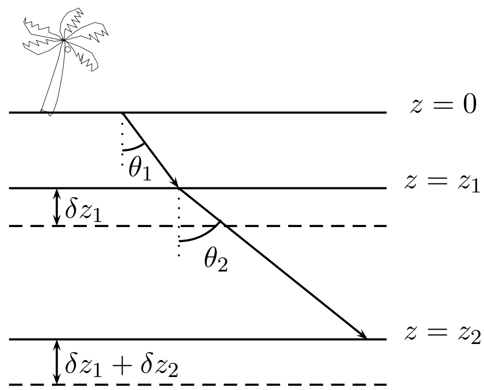

Figure 3.2. Model of two horizontal layers above a compacting reservoir. The compaction increases the thickness of layer 1 by δz_1 and that of layer 2 by δz_2. The velocities remain constant after the deformation.

where

$$\Delta e_{zz}\, R_1 = -B_1 \Delta e_{kk}\, ; \quad \Delta e_{zz}\, R_2 = -B_2 \Delta \sigma_{33}\, . \tag{3.19}$$

Hence, the ratio R represents the average of two terms related to the volumetric strain and vertical deviatoric stress changes. If the reservoir thickness is much smaller than its depth, the volumetric changes are expected to be small. Then the ratio R can be used to estimate $\Delta\sigma_{33}$ using reflectors at or above the reservoir. On the other hand, for reservoirs with comparable depth and thickness R is likely to reflect both volumetric and deviatoric stress changes.

3.5 Modeling of Traveltime Shifts

In this section we use equation 3.17 to study the influence of both reflector deformation and velocity changes on traveltime shifts. First, we obtain an analytic expression for traveltime shifts caused by the movement of reflectors in a simple horizontally layered medium. Then we compute and discuss the spatial distribution of traveltime shifts in shot and CMP (common-midpoint) gathers for a 2D model of a compacting reservoir.

3.5.1 Special Case: Reflector Deformation in A Layered Medium

We consider a ray that travels from the surface to the bottom of a model comprised of two horizontal isotropic layers. The layers are assumed to have been deformed uniaxially in the z-direction such that the thickness of layer 1 was increased by δz_1 and that of layer 2 by δz_2 (Figure 3.2).

To study the influence of the geometric changes, the velocities in the layers (v_1 and

v_2) are kept constant after the deformation. Therefore, the exact one-way traveltime from the top to the bottom of the model after the deformation can be written as

$$t = \frac{z_1 + \delta z_1}{v_1 \cos\theta_1} + \frac{z_2 + \delta z_2}{v_2 \cos\theta_2}\,, \tag{3.20}$$

where θ_1 and θ_2 are the angles between the ray and the vertical in the first and second layers, respectively. Hence, the exact traveltime difference due to the deformation is

$$\Delta t_{\rm ex} = \frac{\delta z_1}{v_1 \cos\theta_1} + \frac{\delta z_2}{v_2 \cos\theta_2}\,. \tag{3.21}$$

Expressing $\Delta t_{\rm ex}$ in equation 3.21 in terms of the vertical components $q_i = \cos\theta_i / v_i$ of the slowness vector and the propagation angle θ_i $(i = 1, 2)$, we find:

$$\Delta t_{\rm ex} = \delta z_1\, q_1 \left(1 + \tan^2\theta_1\right) + \delta z_2\, q_2 \left(1 + \tan^2\theta_2\right). \tag{3.22}$$

Applying equation 3.17 to the reference ray traced before the deformation (the ray in Figure 3.2 with the same take-off angle θ_1) yields an approximation ($\Delta t_{\rm pert}$) for $\Delta t_{\rm ex}$:

$$\begin{aligned} \delta t^e &= (\delta z_1 + \delta z_2)\, q_2\,, \\ \delta t^i &= \delta z_1\, (q_1 - q_2)\,, \\ \Delta t_{\rm pert} &= \delta t^e + \delta t^i \ = \delta z_1\, q_1 + \delta z_2\, q_2\,. \end{aligned} \tag{3.23}$$

For propagation angles of up to $25 - -30^\circ$ equations 3.22 and 3.23 give similar results because $\tan^2\theta \ll 1$. In particular, for zero-offset rays ($\theta_1 = \theta_2 = 0$) equation 3.23 is exact. Note that multiplying equations 3.22 and 3.23 by a factor of two yields two-way traveltime shifts for a reference ray with the source located at position s and receiver at $r = s + 2X$ ($X = z_1 \tan\theta_1 + z_2 \tan\theta_2$) on the surface of the model.

3.5.2 Traveltime Shifts Due to Velocity Changes

To illustrate the distribution of traveltime shifts in prestack data, we applied equation 3.17 to a 2D model that includes a rectangular reservoir embedded in a homogeneous isotropic halfspace (Figure 3.3). In such a model, traveltime shifts can be attributed to velocity changes only, because geometric terms will cause shifts not exceeding 10^{-2} ms. The pore-pressure variation occurs only in the reservoir, and the resulting excess stress, strain and displacement were computed using analytic expressions adapted from Hu (1989). The strain was confined to the incidence plane $[x, z]$, with no deformation in the y-direction ($e_{12} = e_{22} = e_{23} = 0$).

Figure 3.4 shows the spatial distribution of the deviatoric stresses and volumetric strains generated by the pore-pressure drop inside the reservoir. For the plane strain problem treated here, the stress tensor is triaxial, so the 3D stress-induced velocity field has orthorhombic symmetry. The velocity function in the $[x, z]$-plane, however, can be described by a heterogeneous transversely isotropic (TI) model with a tilted symmetry axis because this vertical plane represents a symmetry plane of the orthorhombic medium. Using the perturbations of the stiffness coefficients, we computed the stress-related Thomsen parameters ϵ and δ and the rotation angle of the symmetry axis from the vertical (Figure 3.5). Because the strain-sensitivity tensor and the background medium are isotropic, the resulting velocity anisotropy is elliptical ($\epsilon = \delta$). The absolute δ-values in and near the reservoir reach 0.18, which indicates that the stress-induced anisotropy is non-negligible even for the relatively small pressure drop (5 MPa) used in the test. The similarity between δ and the normal deviatoric stress components ($\Delta\sigma_{11}$ and $\Delta\sigma_{33}$) is explained by the fact that for our model $\Delta\sigma_{11} \approx -\Delta\sigma_{33}$. Then, for locations where $\Delta\sigma_{13}$ is small and the symmetry axis is close to vertical, δ is given by (Sarkar et al., 2003)

$$\delta = \frac{C_{155}}{C_{33}^0\, C_{44}^0} \left(\Delta\sigma_{11} - \Delta\sigma_{33}\right) \approx \frac{2\Delta\sigma_{11}\, C_{155}}{C_{33}^0\, C_{44}^0} \,. \tag{3.24}$$

Close to the corners of the reservoir, accumulation of the shear stress $\Delta\sigma_{13}$ causes rotation of the symmetry axis (Figure 3.5 b).stress-induced anisotropy is described by a tilted orthorhombic model[2].

Approximate and exact (ray-traced) traveltime shifts are compared in Figure 3.6. The noticeable discrepancy for reflectors beneath the reservoir is caused by the large velocity change inside the reservoir (as high as 27% for the P-wave vertical velocity). For deep reflectors, the linearized approximation 3.17 is more accurate in models with lower velocity sensitivity inside the reservoir.

The offset variation of traveltime shifts in Figure 3.6 is controlled by the spatial distribution of deviatoric stress and volumetric changes as well as by the incidence angle (see equation 3.17). Since stress-induced velocity changes are mostly concentrated inside and near the reservoir, traveltime shifts are largest for rays that probe the immediate vicinity of the reservoir. We observe two distinct trends for traveltime shifts depending on the CMP location with respect to the reservoir. For common midpoints within the projection of the reservoir onto the surface, traveltime shifts tend to decrease by absolute value with offset (Figures 3.6 and 3.7a). In contrast, the magnitude of traveltime shifts for CMP locations outside the reservoir projection generally increases with offset (Figure 3.7b). Likewise, traveltime shifts in shot gathers become mostly confined to longer offsets as the source is moved away from the reservoir center (Figure 3.8).

For a fixed CMP or shot location, the offset dependence of traveltime shifts is largely governed by the term $\Delta\sigma_{ij}n_in_j$ in equation 3.17. For instance, the reflectors above the reservoir in Figure 3.7 show an increase rather than a decrease in the magnitude of the shifts for larger offsets.

Ultimately, this variation of traveltime shifts with incidence angle (i.e., with direction **n**) may help to estimate the components of the deviatoric stress tensor from prestack seismic data. Therefore, it is important to analyze the relative magnitude of traveltime shifts caused by isotropic and anisotropic velocity changes. For the homogeneous and isotropic background model used in the test, volumetric (i.e., isotropic) changes are significant only

[2]The medium symmetry can be verified by setting $e_{22} = e_{12} = e_{23} = 0$ in equations D.16–D.33.

inside the reservoir (see Figure 3.4). Thus, traveltime shifts above the reservoir are primarily produced by deviatoric stress (i.e., anisotropic) changes, while volumetric changes make a non-negligible contribution for reflectors at and below the reservoir level (see Figure 3.9).

Still, the character of the offset variation of traveltime shifts is largely controlled by the anisotropic terms even for deep reflectors, especially for common midpoints close to the center of the reservoir (Figure 3.10). For CMP locations inside the reservoir projection onto the surface, the isotropic and anisotropic components of the traveltime shifts have slopes of opposite sign (Figures 3.10a–3.10d). In contrast, the slopes have the same sign for common midpoints outside the reservoir projection (Figures 3.10e and 3.10f). Therefore, if the volumetric term is neglected in a inversion scheme, deviatoric stress changes reconstructed from traveltime shifts will be underestimated for CMP locations inside the reservoir projection and overestimated for those outside it. The sharp variations of the small-offset shifts near the reservoir edges ($x = \pm 1$ km) in Figure 3.10 are caused by singularities in the analytic solutions for stress used in the modeling.

Figure 3.11 demonstrates that the vertical stress change ($\Delta\sigma_{33}$) governs small-offset traveltime shifts, while the contributions of the horizontal and shear stresses gradually increase with offset. Indeed, for our 2D model the term $\Delta\sigma_{ij} n_i n_j$ in equation 3.17 takes the form

$$\Delta\sigma_{ij} n_i n_j = \Delta\sigma_{33} \cos^2\theta + 2\Delta\sigma_{13} \cos\theta \sin\theta + \Delta\sigma_{11} \sin^2\theta \,, \tag{3.25}$$

where θ, as before, is the incidence angle. Clearly, the sensitivity of traveltime shifts to the components $\Delta\sigma_{13}$ and $\Delta\sigma_{11}$ increases with offset. Equation 3.25 and Figure 3.11 indicate that, in principle, the horizontal and shear stress changes can be estimated from the offset dependence of traveltime shifts. Reconstruction of the stress components, however, is complicated by the strong heterogeneity of the excess stress field around the reservoir. As illustrated by Figure 3.12a, for a relatively shallow reflection event recorded above the center of the reservoir, the slope of the function δt up to relatively long offsets is governed mostly by $\Delta\sigma_{11}$. However, when the CMP is located above the edge of the reservoir (Figure 3.12b), the offset variation of traveltime shifts is dominated by $\Delta\sigma_{13}$ with contributions from $\Delta\sigma_{33}$ and $\Delta\sigma_{11}$.

3.6 Conclusions

Our analytic description of compaction-related traveltime shifts is based on three main assumptions. First, a closed-form expression for traveltime shifts was obtained using first-order traveltime perturbations. Anisotropic ray tracing for a 2D model of a compacting reservoir confirms that the first-order approximation reproduces the general behavior of traveltime shifts. The approximate solution produces substantial errors for deep reflectors when the velocity changes inside the reservoir are large (30% or so). However, case studies of compaction-related traveltime shifts suggest that the our model likely exaggerates the strain sensitivity inside the reservoir. Second, we used an isotropic sixth-order strain-sensitivity tensor to describe the influence of stress on the stiffness coefficients. While this assumption limits the stress-induced anisotropic model to the special case of tilted orthorhombic symmetry[3], it also reduces the number of model parameters and helps to derive concise expressions for traveltime shifts.

Third, deformation was assumed to be purely elastic, which is not always appropriate for velocity changes inside a compacting reservoir (or within a reactivated fault zone outside it) where the contribution of anelastic processes may be substantial. We believe, however, that the physical insight provided by our relatively simple equations justifies neglecting plastic deformation. Also, experimental studies confirm that elastic theory adequately describes a wide range of deformation processes caused by reservoir depletion in various geological settings.

The main result of our analytic development is equation 3.17, which generalizes the expressions for zero-offset traveltime shifts and those for offset-dependent traveltime shifts in isotropic media. The simple structure of equation 3.17 helped us to gain valuable insight into the behavior of compaction-related traveltime shifts in common-midpoint (CMP) and shot gathers.

Traveltime shifts are caused by two different factors – geometric and velocity changes. Analysis of equation 3.17 indicates that the geometric component of the traveltime shifts typically is at least an order of magnitude smaller than the contribution of the velocity changes. Traveltime shifts due to the velocity changes could be further separated into two components, one of which is related to volumetric changes and the other to deviatoric stresses. Significant volumetric changes are restricted to the reservoir and to the vicinity of the model surface. The deviatoric stress term, which is related to changes in nonhydrostatic stress, controls the velocity anisotropy of the deformed elastic medium. Equations 3.16 and 3.17 also reveal the role of different components of the strain-sensitivity tensor. In particular, the combination $C_{111} + 2C_{112}$ is responsible for the isotropic P-wave velocity changes, while (in agreement with previously published results) C_{155} governs the magnitude of the stress-induced velocity anisotropy.

Although our numerical results are obtained for a simple 2D model, they illustrate several important properties of stress-induced variations in reflection traveltimes. First, traveltime shifts for reflectors at and above the reservoir are associated primarily with the deviatoric stress components (i.e., with stress-induced anisotropy). Because anisotropy parameters should be estimated from offset-dependent traveltimes, it would be highly beneficial to include prestack data in time-lapse analysis. Second, the magnitude of the anisotropy parameters may be substantial, and the orientation of the symmetry axis rapidly varies in space around the reservoir corners (similar variation is also observed for ellipsoidal reservoirs models close to the points of maximum curvature). Third, the modeling helps to understand the complex spatial distribution of traveltime shifts caused by the interplay between the propagation direction and different stress components. On the whole, adding an extra dimension (offset) to time-lapse analysis should help to better constrain the geomechanical changes around depleting blocks and improve interpretation of 4D seismic data.

One of the main practical difficulties in modeling and interpretation of compaction-related traveltime shifts is their dependence on the sixth-order strain-sensitivity tensor. Our analytic results, obtained under the simplifying assumption that this tensor is isotropic,

[3]In each of the symmetry planes, the stress-induced anisotropy is elliptical.

include two independent strain-sensitivity elements. Reliable constraints on these two elements can be provided by laboratory measurements of stress sensitivity of reservoir and overburden rocks similar to those already described in the literature.

Further development of the theory presented here could involve several possible directions. The first is to incorporate second-order phenomena, especially those related to the influence of lithostatic and regional stress fields and of plastic deformation. Then it may be possible to evaluate whether the contributions of compressive and tensile stress changes are indeed asymmetric. Note that existing measurements of traveltime shifts indicate that velocity is much more sensitive to tensile than to compressive stress. Indeed, velocity changes observed inside reservoirs are relatively small despite the strong compression of reservoir rocks. The second topic for future research is to derive similar equations for traveltime shifts of converted modes and pure shear waves. Time-lapse prestack shear-wave data should provide additional constraints on the parameters of the stress field. Third, our analytic results can be extended to incorporate intrinsic anisotropy, while keeping the strain-sensitivity tensor isotropic.

3.7 Acknowledgments

We are grateful to members of the A(nisotropy)-Team of the Center for Wave Phenomena (CWP) at Colorado School of Mines (CSM) for helpful discussions. We also thank the associate editor, Mirko van der Baan, two anonymous reviewers and Martin Landrø for suggestions, which helped to improve this manuscript. This work was supported by the Consortium Project on Seismic Inverse Methods for Complex Structures at CWP and by the Chemical Sciences, Geosciences and Biosciences Division, Office of Basic Energy Sciences, Office of Science, U.S. Department of Energy.

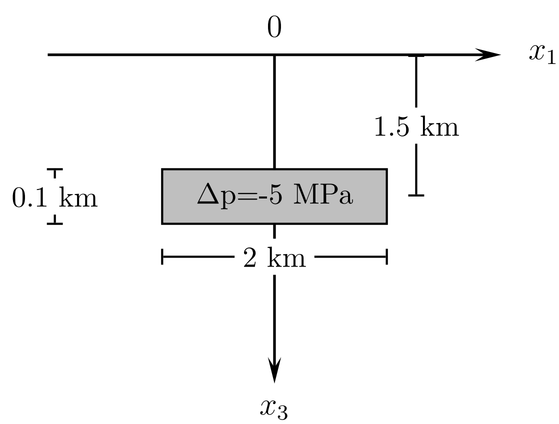

Figure 3.3. 2D model of a rectangular reservoir embedded in an isotropic homogeneous medium. The pressure drop inside the reservoir is 5 MPa. The medium parameters are taken from the laboratory results of Sarkar et al. (2003) for Berea sandstone: $V_P = 2.3$ km/s, $V_P/V_S = 1.58$, $\rho = 2.14$ g/cm^3, $C_{111} = -13904$ GPa, $C_{112} = 533$ GPa and $C_{155} = -3609$ GPa. To compute the excess stress, we set the Biot-Willis coefficient α to 0.85 (the closer is α to unity, the more stress is generated by reducing the pore pressure in the reservoir). To simulate the static stiffness coefficients, V_P was reduced by 10%, which yields the typical difference between the static and dynamic stiffnesses for well-consolidated rocks with low porosity (Yale and Jamieson, 1994).

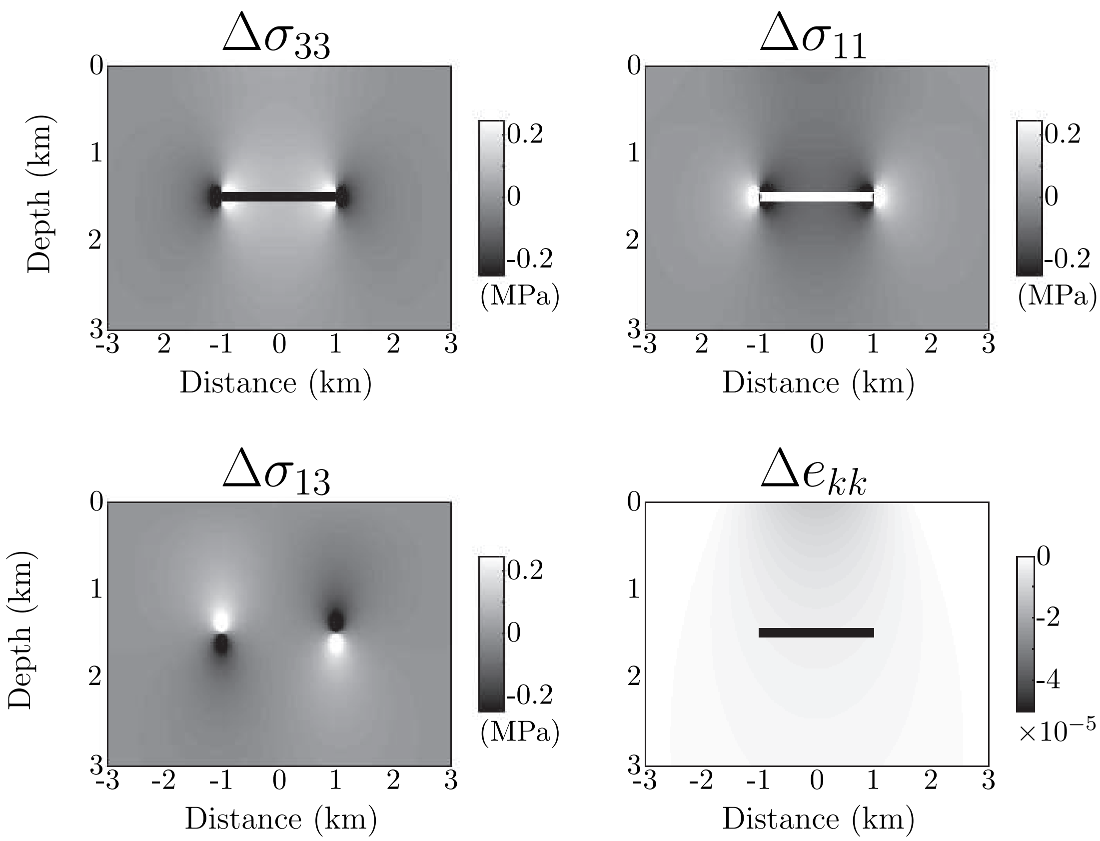

Figure 3.4. Stress and strain changes for the model from Figure 3.3 caused by the reservoir compaction. The top row shows changes in the vertical ($\Delta\sigma_{33}$) and horizontal ($\Delta\sigma_{11}$) normal deviatoric stresses. The shear deviatoric stress ($\Delta\sigma_{13}$) and the trace of the strain tensor Δe_{kk} are shown in the second row. Negative values imply compression for stress and contraction (shortening) for strain. Outside the reservoir, $\Delta\sigma_{11} \approx -\Delta\sigma_{33}$. Inside the reservoir, the maximum stress values are $\Delta\sigma_{33} = -2.2$ MPa and $\Delta\sigma_{11} = 1.7$ MPa, while the volumetric change is constant: $\Delta e_{kk} = -4.6 \times 10^{-4}$ (the plots were clipped for better visualization).

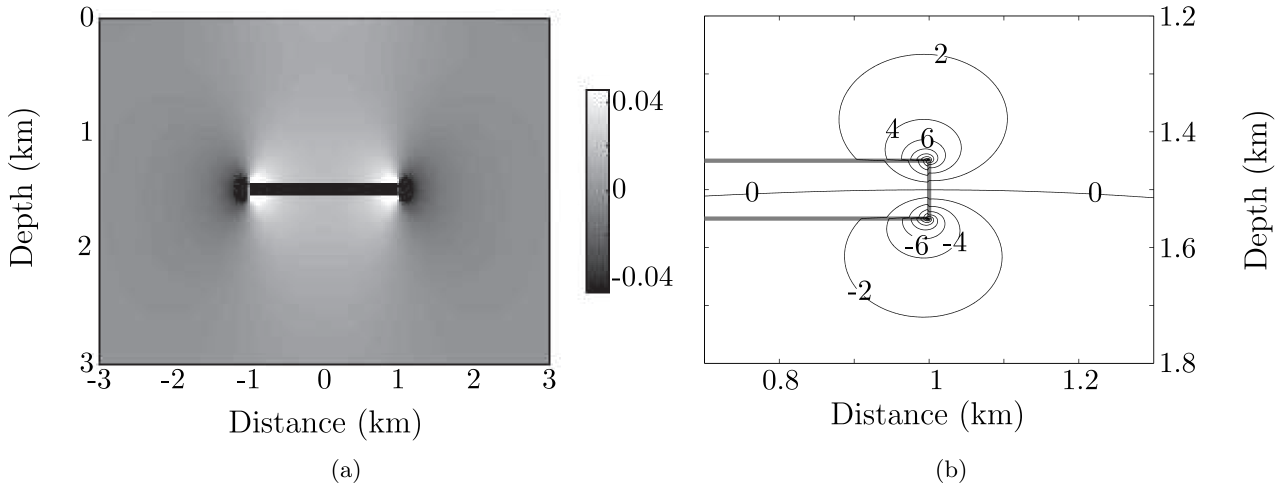

Figure 3.5. Reservoir compaction makes the medium heterogeneous and anisotropic. a) The anisotropy parameter $\delta = \epsilon$ (color scale is clipped); b) contours of the angle between the symmetry axis and the vertical (positive angle corresponds to counterclockwise tilt of the axis) near the reservoir right edge (solid gray outline). Inside the reservoir $\delta = -0.18$, while the tilt of the symmetry axis at the reservoir corners approaches $\pm 45°$.

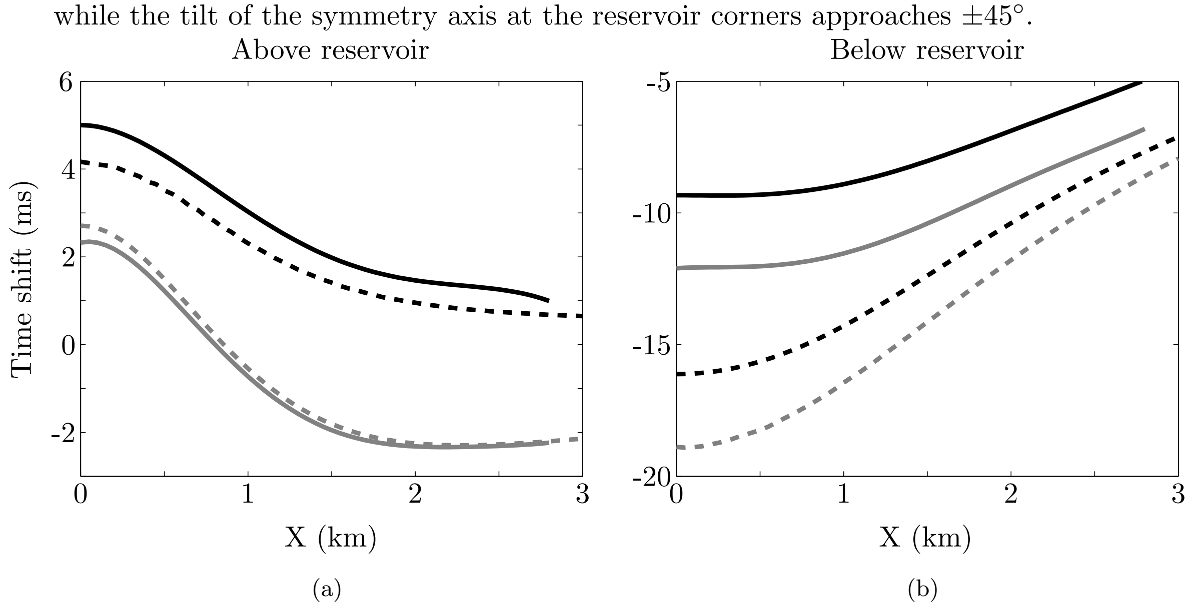

Figure 3.6. Comparison between traveltime shifts in CMP geometry computed by ray tracing (solid lines) and from approximation 3.17 (dashed). The CMP is located above the center of the reservoir ($x = 0$ km in Figure 3.3). The depths of imaginary reflectors are a) 1 km (gray) and 1.45 km (black); b) 1.55 km (gray) and 2 km (black). For this geometry, $X = \frac{1}{2}(s - r)$, where s and r denote the source and receiver positions.

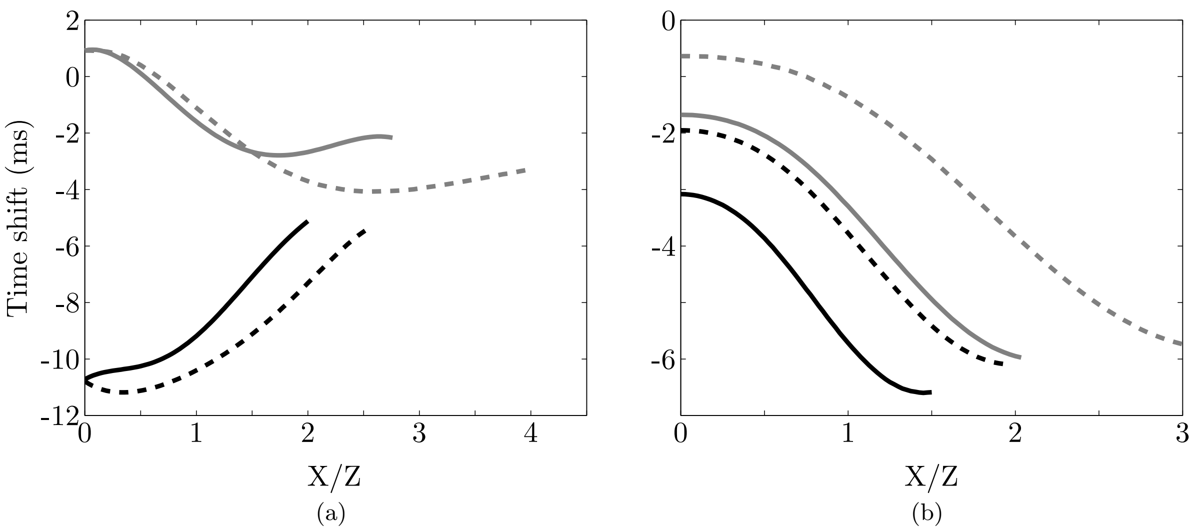

Figure 3.7. Traveltime shifts in CMP geometry for common midpoints at a) $x = 1$ km and b) $x = 2$ km. The gray lines correspond to imaginary reflectors above the reservoir at depths 1 km (dashed) and 1.45 km (solid). The black lines correspond to reflectors below the reservoir at 1.55 km (dashed) and 2 km (solid). X/Z is the ratio of the half-offset and reflector depth, which is equal to $\tan\theta$ for the reference ray.

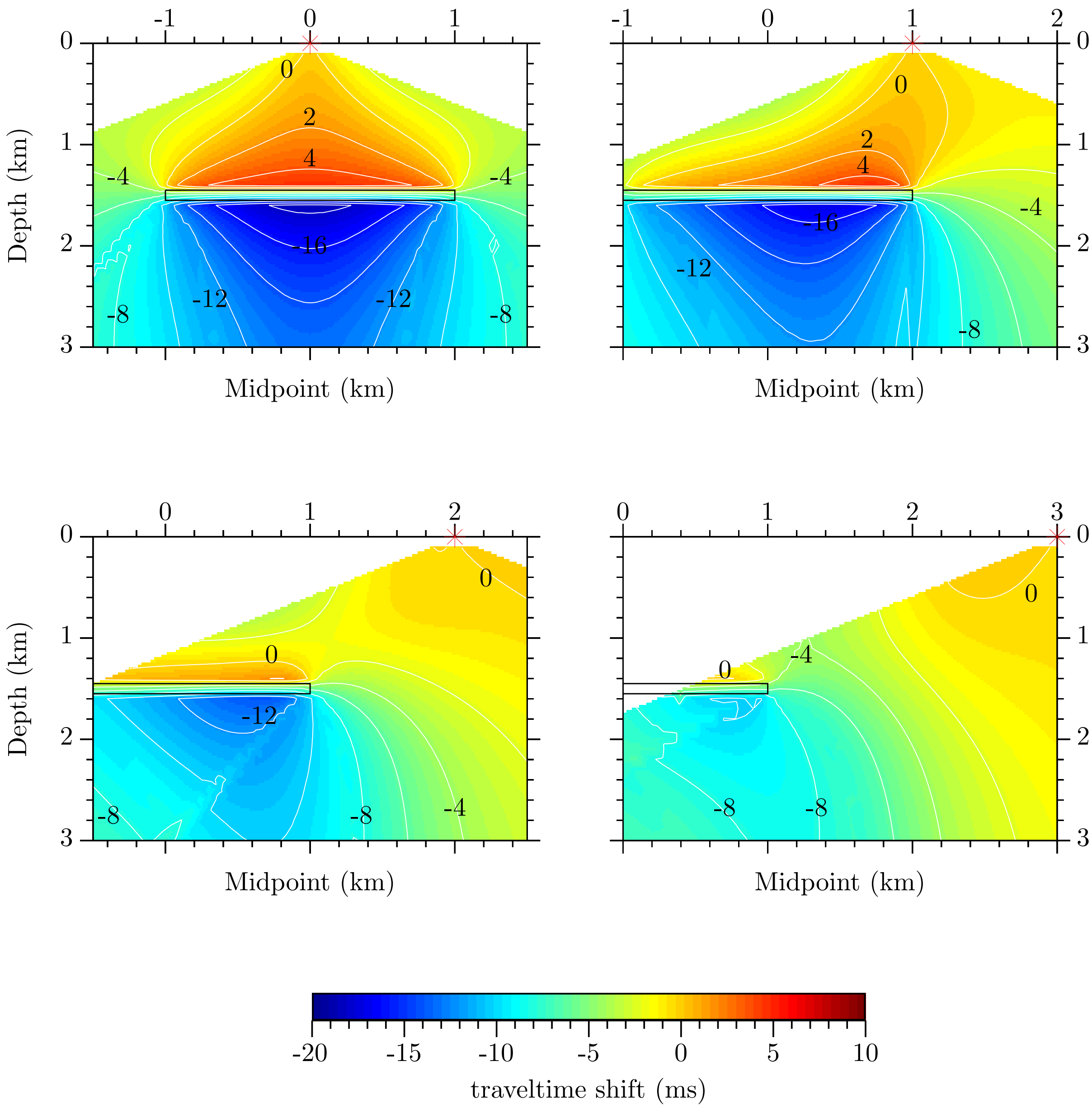

Figure 3.8. Traveltime shifts for four different shot locations (between 0 and 3 km) marked by the asterisk. The shift plotted at each (x, z) point would be recorded at the source-receiver offset $2x$ (i.e., the midpoint is at location x) from an imaginary horizontal interface at depth z. The reservoir is marked by the black rectangle. Revised version of orignal figure

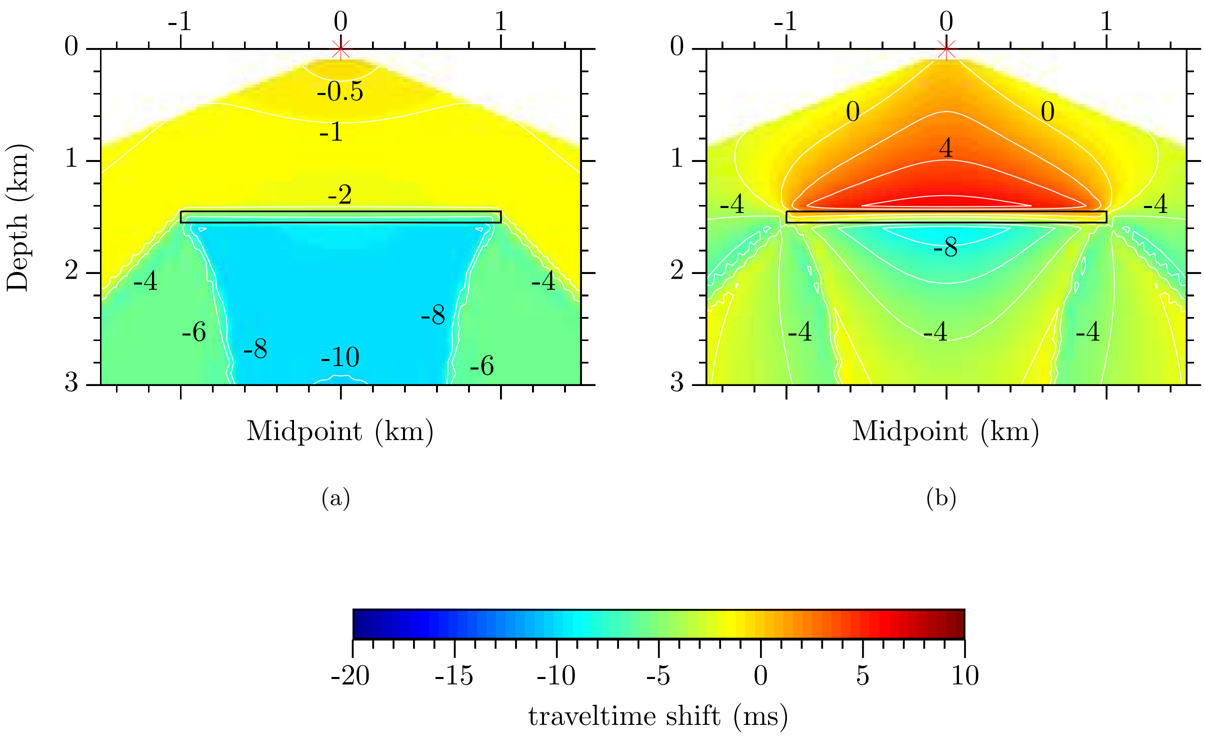

Figure 3.9. Traveltime shifts for a shot (marked by the asterisk) above the center of the reservoir (same display as in Figure 3.8). The contributions of the volumetric changes (a) and deviatoric stress changes (b) are computed separately.

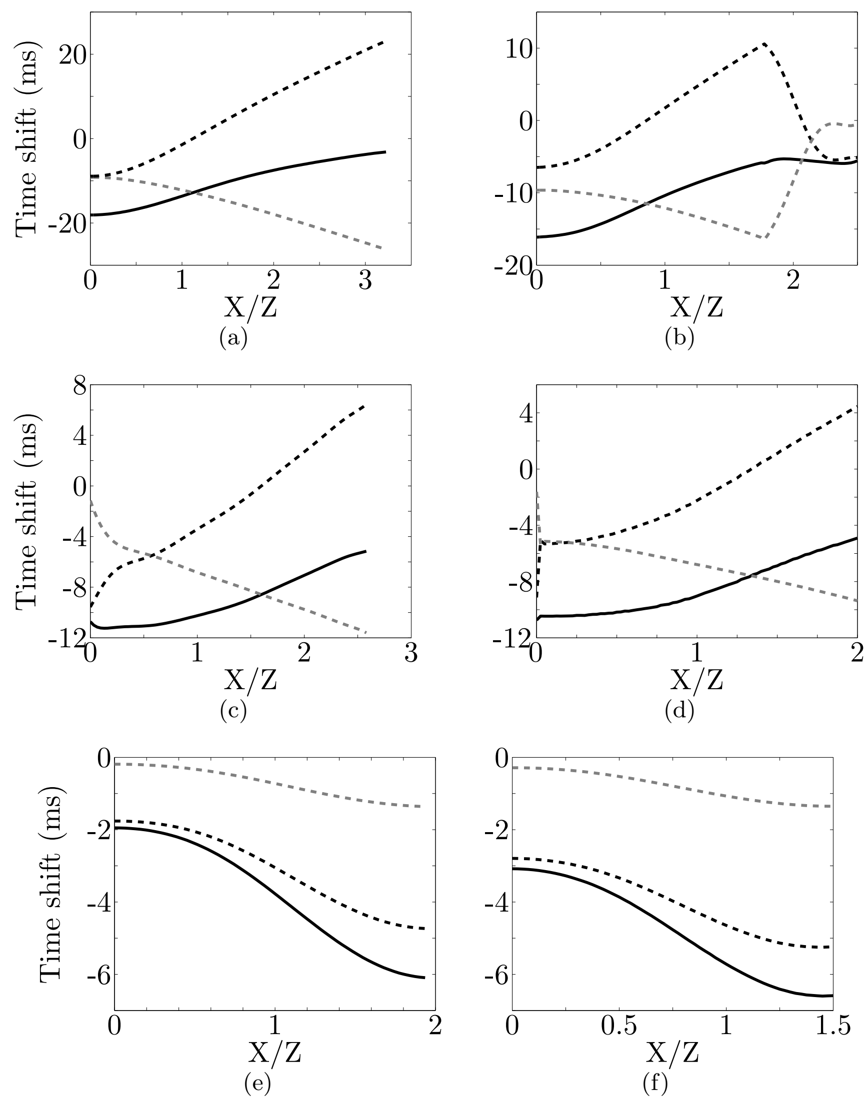

Figure 3.10. Traveltime shifts in CMP geometry for three different midpoints x (each row corresponds to a midpoint) and two different reflector depths z. a) $x = 0$ km, $z = 1.55$ km; b) $x = 0$ km, $z = 2$ km; c) $x = 1$ km, $z = 1.55$ km; d) $x = 1$ km, $z = 2$ km; e) $x = 2$ km, $z = 1.55$ km; and d) $x = 2$ km, $z = 2$ km. The total shifts (solid black lines) are plotted along with the shifts due to the volumetric changes (dashed gray) and deviatoric stress changes (dashed black).

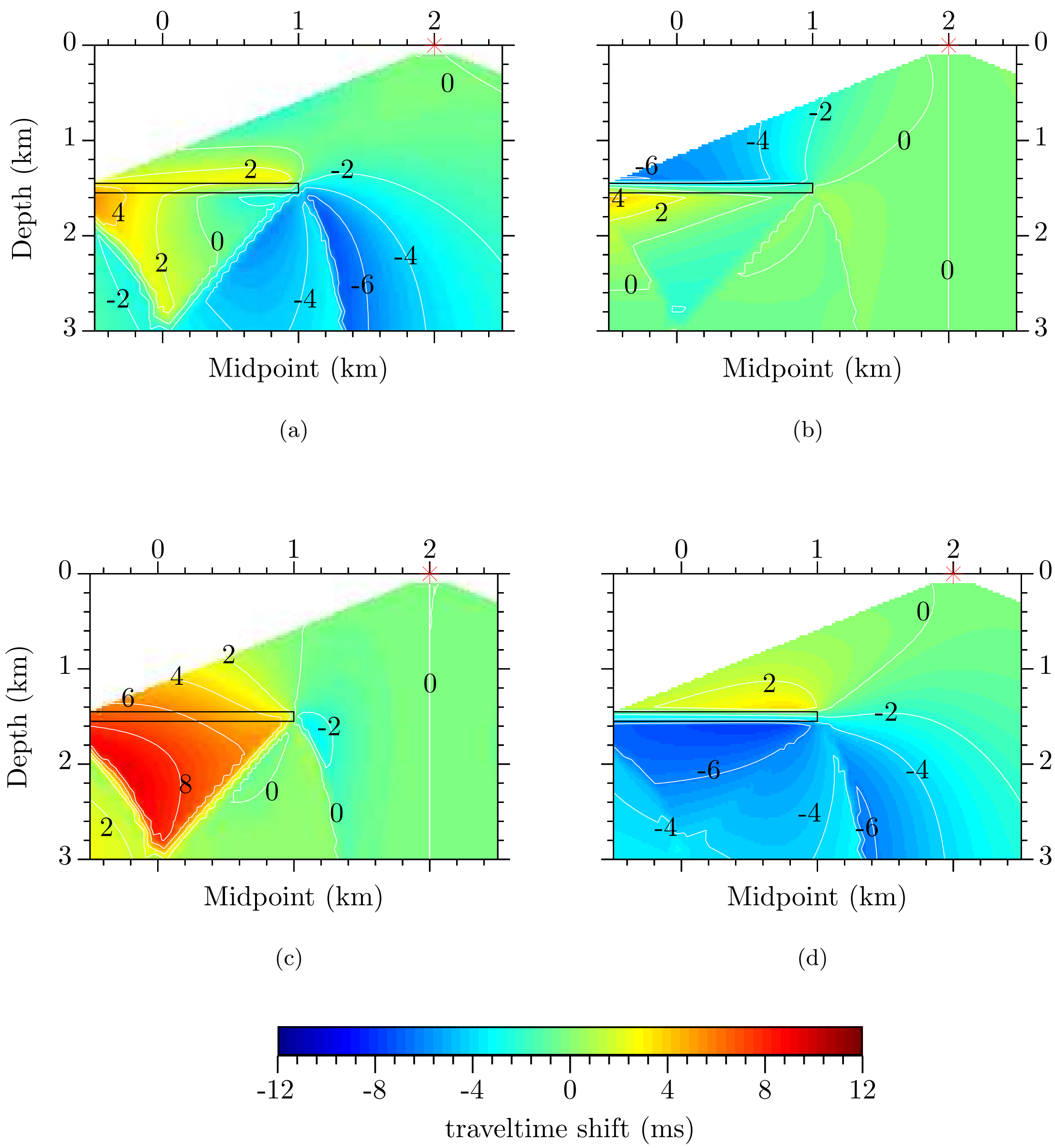

Figure 3.11. Contributions of the three deviatoric stress components to the traveltime shifts for the shot at $x = 2$ km (asterisk) from Figure 3.8. The shift due to a) the total deviatoric stress change ($\Delta\sigma_{11} + \Delta\sigma_{13} + \Delta\sigma_{33}$); b) $\Delta\sigma_{11}$; c) $\Delta\sigma_{13}$; and d) $\Delta\sigma_{33}$.

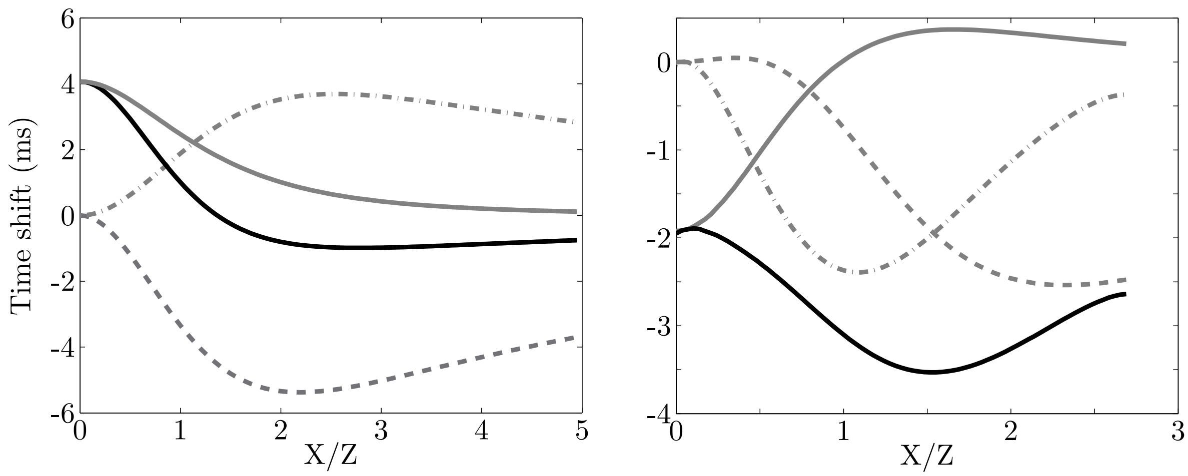

(a) (b)

Figure 3.12. Contributions of the three deviatoric stress components to traveltime shifts in CMP geometry for a) $x = 0$ km, $z = 1$ km; and b) $x = 1.1$ km, $z = 1.45$ km. The shifts due to the total deviatoric stress change (solid black lines) are plotted along with the contributions of $\Delta\sigma_{11}$ (dashed), $\Delta\sigma_{13}$ (dash-dotted), and $\Delta\sigma_{33}$ (solid gray).

Chapter 4

Influence of Background Heterogeneity on Traveltime Shifts for Compacting Reservoirs

4.1 Summary

Compaction induced by pore-pressure decrease inside a reservoir can be monitored by traveltime shifts of reflection events in time-lapse seismic data. Recently, we demonstrated that anisotropic velocity perturbations govern the traveltime shifts caused by compaction in homogeneous background models. Thus, analysis of these shifts in the offset domain provides additional information about the velocity perturbation field that cannot be retrieved from zero-offset data.

In this paper we model and analyze traveltime shifts for compacting reservoirs whose elastic properties are different from those of the surrounding medium. Synthetic examples show that large contrasts in rigidity modulus μ ($> 25\%$) across the reservoir boundaries produce significantly larger isotropic velocity perturbations outside the reservoir, in comparison with homogeneous models. Nevertheless, this effect is mostly confined to interfaces close to the top and bottom of the reservoir. Hence, anisotropic velocity perturbations remain the dominant component of traveltime shifts. As a consequence, prestack analysis of traveltime shifts is required to help constrain the compaction-induced velocity perturbations in heterogeneous background models as well. In addition, our analysis gives insight on how traveltime shifts behave when reservoirs are stiffer or softer than the host rocks. For example, compaction of softer reservoirs yields larger anisotropic velocity perturbations inside the reservoir, but smaller ones outside it, in comparison with homogeneous background models. As a result, traveltime shifts show more offset variation if reflections come from below the softer reservoir. Finally, analysis of a layered model, based on velocity profiles from Valhall field in the North Sea, indicates that compaction-induced strain changes are similar to simpler models, despite discontinuities in strain across layer boundaries. Substantial differences, however, are observed on the patterns of traveltime shifts, because velocity perturbations were largely confined to the softer and more stress-sensitive upper part of the model. Thus, larger offset variation of traveltime shifts are observed for reflections from interfaces above the reservoir, recorded in CMPs close to the edges of the reservoir.

4.2 Introduction

Traveltime shifts (i.e., the differences in traveltime for the same reflector measured between time-lapse seismic surveys) are increasingly used to monitor dynamic changes in hydrocarbon reservoirs caused by depletion. For example, Guilbot and Smith (2002) employ traveltime shifts to detect and monitor reservoir compaction and surface subsidence in Ekofisk field in the North Sea. Hatchell and Bourne (2005b) introduce a method to estimate the ratio of the perturbations in the vertical velocity and vertical strain from traveltime shifts measured on stacked data. This ratio ("R") can be used to monitor compaction and detect compartments in a reservoir. Hodgson et al. (2007) use the vertical derivatives of traveltime shifts computed from stacked data to estimate the pressure changes in the Genesis reservoir.

In a recent paper (Fuck et al., 2009), we derive an analytic expression for traveltime shifts that provides valuable physical insight into the influence of compaction-related stress on reflection traveltimes. In contrast to previously published papers (e.g. Landrø and Stammeijer, 2004; Hatchell and Bourne, 2005a; Røste et al., 2006), our approximation permits analysis of traveltime shifts in the offset domain while honoring the fact that reservoir compaction produces heterogeneous, anisotropic velocity perturbations. The numerical examples in Fuck et al. (2009) are given for the simple model of a 2D homogeneous halfspace, with pore-pressure changes confined to a rectangular reservoir. Traveltime shifts in this model are primarily controlled by the anisotropic velocity perturbations, which should be estimated from prestack data.

Here we model and analyze traveltime shifts for a compacting reservoir whose elastic properties are different from those of the surrounding medium. These numerical simulations are designed to evaluate how the elastic contrast influences traveltime shifts created by the pore-pressure drop inside the reservoir. First, we review the properties of the excess stress and strain in and around a reservoir undergoing a pore-pressure drop in an initially homogeneous model. Then, we discuss the approximation for traveltime shifts presented by Fuck et al. (2009) and review the modeling algorithm used here to simulate traveltime shifts for the two types of 2D models. The first type includes a rectangular reservoir embedded in an otherwise homogeneous host rock; for the second-type models, the background medium is horizontally layered. The numerical results demonstrate that although the contrast in the elastic properties between the reservoir and host rock changes traveltime shifts, they are still controlled primarily by the anisotropic velocity perturbations.

4.3 Excess Stress and Strain for Compacting Reservoirs

Compaction of hydrocarbon reservoirs results from both elastic and anelastic deformation induced by depletion. Elastic deformation, in general, is caused by the pore-pressure drop inside the reservoir; anelastic (i.e., irreversible) deformation may include the crushing of grains and pores or dissolution of reservoir rocks by injected fluids used to enhance oil recovery.

We restrict our treatment to elastic strains, following the approach of Geertsma (1973), Segall (1992) and Segall et al. (1994), who successfully explained depletion-induced phenomena using linear poroelastic behavior of the reservoir rocks. Poroelastic rocks can be deformed not only by external forces, but also by pressure changes inside the pores [1]. Due to the spatial variation of the pore-pressure changes (which are restricted to the reservoir), the excess strain field includes not only normal but also shear components. For homogeneous models of this type, it is possible to obtain analytic solutions for the particle displacement, stress and strains, if the reservoir has a relatively simple shape. Hu (1989), for instance, provides a concise analytic description of the excess stress field for a 3D reservoir that has the shape of a parallelepiped[2]. Such analytic solutions provide important physical insight into the behavior of offset-dependent traveltime shifts. For instance, Hu (1989) demonstrates that volumetric strain changes (i.e., the trace Δe_{kk} of the strain tensor) vanish outside the reservoir, if the background model is homogeneous, while Downes et al. (1997) show that Δe_{kk} inside the reservoir should be constant[3]. Nonzero volumetric changes outside the reservoir occur only if the model includes a free surface. In this case, the largest values of Δe_{kk} are observed near the surface (Hu, 1989); this anomaly decreases for deeper reservoirs.

Furthermore, it can be inferred from the equations of Hu (1989) that the deviatoric stress changes $\Delta\sigma_{ij}$ are inversely proportional to the squared ratio of P- and S-waves velocities (V_P/V_S):

$$\Delta\sigma_{ij} \propto \left(\frac{V_S}{V_P}\right)^2 \alpha\,\Delta P\,, \tag{4.1}$$

where ΔP is the pore-pressure change inside the reservoir and α is the Biot-Willis coefficient[4]. Substituting Hooke's law for isotropic media into equation 4.1, we obtain the deviatoric strain changes ($\Delta\epsilon_{ij} = \Delta e_{ij} - \frac{1}{3}\Delta e_{kk}$) as

$$\Delta\epsilon_{ij} \propto \frac{\alpha\,\Delta P}{\rho V_P^2}\,. \tag{4.2}$$

The volumetric strain change is given by

$$\Delta e_{kk} \propto \frac{\alpha\,\Delta P}{\rho V_P^2}\frac{g}{(3-4g)} \approx \frac{\alpha\,\Delta P}{\rho V_P^2}\,\frac{g}{3}\left(1+\frac{4g}{3}\right)\,, \tag{4.3}$$

where $g = (V_P/V_S)^{-2}$. Since $g << 1$ for most rocks, Δe_{kk} is inversely proportional to both to V_P^2 and to V_P^2/V_S^2.

[1] A good survey of poroelasticity can be found in Wang (2000).

[2] Hu (1989) actually considers the equivalent thermoelastic problem (i.e., the excess stress are caused not by pore-pressure changes, but by temperature changes). Excess strains are obtained by Hooke's law.

[3] The total effective stress inside the reservoir is computed by adding the initial pore-pressure drop to Hu's solution (Glas, 1991).

[4] α varies from 0 to 1 and quantifies the pore-pressure response to external forces.

4.4 Traveltime Shifts

To reach an analytic description of P-wave traveltime shifts observed above a compacting reservoir, Fuck et al. (2009) assume that the corresponding velocity perturbations are small. Traveltime shifts can be obtained from a first-order perturbation of the traveltimes of reference P-wave rays traced in the background velocity model. The approximation includes two terms, one of which is "geometric" (i.e., related to the displacement of the sources, receivers and interfaces), while the other depends on the velocity pertubations along the ray. The stress-induced velocity perturbations are computed using nonlinear theory of elasticity, which represents the stiffness tensor c_{ijkl} of the deformed medium as

$$c_{ijkl} \approx c^{\circ}_{ijkl} + c_{ijklmn}\,\Delta e_{mn}\,, \tag{4.4}$$

where c°_{ijkl} is the stiffness tensor of the background medium, c_{ijklmn} is the strain-sensitivity tensor, and Δe_{mn} is the tensor of the elastic strains induced by the reservoir depletion. Hereafter, the summation convention over repeated indices is assumed. Voigt notation maps each pair of indices ij in equation 4.4 to a single index

$$\alpha = i\delta_{ij} + (9 - i - j)\,(1 - \delta_{ij})\ , \tag{4.5}$$

where δ_{ij} is Kronecker's delta. Equation 4.4 then takes a more concise matrix form (Fuck and Tsvankin, 2009):

$$C_{\alpha\beta} \approx C^{\circ}_{\alpha\beta} + C_{\alpha\beta\gamma}\Delta E_{\gamma}\,. \tag{4.6}$$

Since the compaction-related displacements in the elastic regime yield negligibly small traveltime shifts, the observed shifts are largely caused by the velocity perturbations. Assuming both $C^{\circ}_{\alpha\beta}$ and $C_{\alpha\beta\gamma}$ to be isotropic, we represent the velocity-related P-wave traveltime shifts as (Fuck et al., 2009)[5]:

$$\delta t = -\frac{1}{2}\int_{\tau_1}^{\tau_2}\big[\underbrace{B_1\Delta e_{kk}}_{\text{volumetric}} + \underbrace{B_2\big(\mathbf{n}^{\mathsf{T}}\Delta\epsilon\,\mathbf{n}\big)}_{\text{deviatoric}}\big]\,\mathrm{d}\tau\,, \tag{4.7}$$

where $\mathbf{n}$ is the unit slowness vector of the reference ray, and τ is the time along the reference ray. The constants B_1 and B_2 are defined by:

$$B_1 = \frac{C_{111} + 2C_{112}}{3C^{\circ}_{33}}\,, \tag{4.8}$$

$$B_2 = \frac{4C_{155}}{C^{\circ}_{33}}\,. \tag{4.9}$$

Since $C_{155} = (C_{111} - C_{112})/4$, traveltime shifts in equation 4.7 depend on just two combinations of the three linearly independent elements $C_{\alpha\beta\gamma}$. Equation 4.7 separates the velocity-related traveltime shifts into the isotropic term, which depends on the volumet-

[5]Here, we express the traveltime shifts in terms of the deviatoric strain rather than deviatoric stress to facilitate the comparison between the contributions of the isotropic and anisotropic velocity changes.

ric changes (Δe_{kk}) and the anisotropic term associated with the deviatoric strain changes ($\Delta\epsilon_{ij}$).

4.5 Method

Following Fuck et al. (2009), we employ a three-step procedure to model depletion-related traveltime shifts. First, the excess stress and strain fields are computed for several 2D models with heterogeneous background. We use finite elements (COMSOL^{TM} package) to solve for the displacements, stresses and strains resulting from a pore-pressure drop inside a rectangular reservoir. The modeling is carried out in 2D by assuming a plane-strain model (i.e., there is no deformation in the x_2-direction). The accuracy of the numerical solutions is checked by comparing the results for a homogeneous model with those obtained from the analytic expressions of Hu (1989). The top of the model is specified as a free surface; to avoid artifacts due to the finite model dimensions, the computations are performed for models with the height and width 10 times larger than those of the reservoir. Since the pore-pressure changes are confined to the reservoir, the surrounding rock mass was modeled as linearly elastic.

At the second step, we compute the stiffness and velocity perturbations from the strain changes using equation 4.6. Finally, the traveltime shifts are obtained either from approximation 4.7 or by subtraction of the exact (ray-traced) traveltimes calculated for the perturbed and background velocity models. The anisotropic ray-tracing algorithm is based on the equations of Červený (2001) for heterogeneous anisotropic media, which are solved by the fifth-order Runge-Kutta method (Press et al., 1992). To avoid errors in traveltime shifts caused by smoothing of velocity models, we account for reflection/transmission at interfaces using Snell's law.

4.6 Numerical Results

This section is divided into two parts. First, we analyze models in which the reservoir is embedded in an otherwise homogeneous halfspace ("homogeneous host rock" models). Second, we present the results for a layered model based on velocity profiles from Valhall field in the North Sea.

4.6.1 Homogeneous Host Rock Models

We introduce a contrast in the P- or S-wave velocity between the undeformed reservoir and the host rock, while the density and the matrix $C_{\alpha\beta\gamma}$ are kept constant (Figure 4.1). The velocity contrast ranges from 0% to 50%; the reference values for the stiffness constants and the strain-sensitivity tensor are taken from the laboratory measurements of Sarkar et al. (2003) for a sample of Berea sandstone. For all numerical experiments, the pore-pressure drop is fixed at $\Delta p = -5$ MPa.

To simulate the static stiffnesses, which are generally smaller than those computed from traveltimes (Yale and Jamieson, 1994), the velocities were multiplied with 0.9. The same scaling coefficient was used in the tests of Fuck et al. (2009).

Stress and Strain Modeling The most prominent change caused by the velocity contrast across the reservoir boundary is the presence of a nonzero volumetric strain Δe_{kk} outside the reservoir that is not related to surface subsidence (Figure 4.2). This Δe_{kk} anomaly, however, is observed only when there is a contrast in the rigidity modulus μ, which is in agreement with the semi-analytic results of Soltanzadeh et al. (2007). Indeed, for models with no contrast in μ the pattern of the subsurface distribution of Δe_{kk} is similar to that for a homogeneous background model (Figure 4.2b). In contrast, Figures 4.2c and 4.2d show completely different patterns of the subsurface volumetric changes caused by the contrast in μ. The spatial distribution of Δe_{kk} also depends on whether the reservoir is more or less rigid than the host rock (compare Figures 4.2c and 4.2d).

The deviatoric strain distribution in the subsurface is also sensitive to the contrast in the μ (Figure 4.3). In particular, for relatively stiff reservoirs the deviatoric strain increases toward the reservoir and concentrates near its boundaries. If the reservoir rocks are softer, the deviatoric strain spreads throughout the section (especially in the vertical direction) and tends to accumulate at the reservoir corners[6].

Figure 4.4 illustrates how the volumetric strain and deviatoric strain components ($\Delta\varepsilon_{ij} = \Delta\sigma_{ij}/2\mu$) at the center of the reservoir depend on the contrast in V_S across its boundaries[7]. Then, a stiffer reservoir produces smaller deviatoric and larger volumetric strains, increasing the influence of the isotropic velocity changes for reflectors beneath and at the base of the reservoir. For softer reservoirs the opposite is true, as illustrated by Figure 4.4.

Exceptions include uncommon models with a low P-wave velocity (<2 km/s) and low V_P/V_S (< 1.6) inside the reservoir or with a much stiffer reservoir (i.e., with a high P-wave velocity in excess of 3 km/s and low V_P/V_S). In both cases, however, the volumetric and deviatoric strains change compared to the homogeneous case by almost the same amount. Hence, the relative contributions of the isotropic and anisotropic velocity perturbations to the traveltime shifts remain almost the same.

Finally, we note that the patterns observed in Figures 4.2–4.4 show that equations 4.2 and 4.3, which were derived for the homogeneous case, remain valid for heterogeneous models.

Offset Variation of Traveltime Shifts Two important issues discussed here are the magnitude of the variation of traveltime shifts with offset and the influence of the anisotropic velocity perturbations on this variation. If the offset variation is detectable, it provides new information about the excess stress field only if traveltime shifts are dominated by the anisotropic velocity changes. Otherwise, compaction-related velocity perturbations can be estimated from traveltime shifts on stacked data.

For homogeneous background models, the offset variation is significant, especially for reflectors below the reservoir. Despite the large isotropic velocity changes inside the

[6] The deviatoric vertical and shear strains exhibit patterns similar to that for the horizontal component in Figure 4.3

[7] The density is fixed, so the contrasts in V_S are equivalent to contrasts in μ.

reservoir, the offset variation below the reservoir is, nevertheless, largely controlled by the anisotropic velocity perturbations (Fuck et al., 2009).

As expected from the above results of stress and strain modeling, the behavior of the shifts in the absence of the contrast in μ is similar to that of a homogeneous medium. Indeed, as illustrated by the example in Figure 4.5 the anisotropic velocity perturbations are largely responsible for the traveltime shifts above the reservoir. Below the reservoir, they control the offset variation of the traveltime shifts.

A contrast in μ, however, can cause significant changes in the offset-dependent traveltime shifts. Comparison between Figures 4.6 and 4.7 shows that both the magnitude and offset variation of the traveltime shifts increase for reflections from interfaces above a more rigid reservoir. Conversely, when the reservoir is softer than the host rock, the magnitude of the shifts and their offset variation increase for reflectors beneath the reservoir. These changes in the behavior of the traveltime shifts can be explained by the variation in the subsurface distribution of strain with the contrast in μ. For example, the shifts above the reservoir result mostly from deviatoric strains. Therefore, the larger deviatoric strains observed above a more rigid reservoir (compare Figures 4.3b and 4.3c) produce larger shifts with more pronounced offset variation. Traveltime shifts beneath the reservoir are strongly depedent on the strains accumulated inside it. In particular, the larger offset variation of traveltime shifts beneath a softer reservoir is explained by the reduction in the volumetric strain and increase in the deviatoric strains inside such reservoirs (Figures 4.4a and 4.4b).

Figures 4.8 and 4.9 help to understand how the contrast in μ influences the behavior and composition of the traveltime shifts. In general, the offset variation of the traveltime shifts becomes more pronounced, if the contrast in μ enhances the anisotropic component of the shifts (i.e., increases the deviatoric strain).

On the whole, the anisotropic velocity perturbations largely govern the offset-dependent traveltime shifts for this group of models.

4.6.2 Layered Model

This model consists of eight horizontal layers whose parameters were adapted from velocity profiles measured in the Valhall Field in the North Sea (Figure 4.10). The components of the strain-sensitivity tensor correspond to those estimated by Prioul et al. (2004) for North Sea shales under two different ranges of hydrostatic load. Taking into account the weight of the model column, the layers above 2 km were assigned C_{ijk} that were estimated for the shales under the hydrostatic load in the range from 5 to 30 MPa [8]; the deeper layers were assigned C_{ijk} measured for the load between 30 and 100 MPa. In order to obtain the static stiffness similar to those published in Herwanger and Horne (2005) for their Valhall model, seismic velocities were reduced by 40%.

Stress and Strain Modeling Apart from the discontinuities in strain across the layer boundaries, the depletion-induced strains for the layered model are, in general, similar to those observed for the simpler models investigated above. For example, since the reservoir

[8] in the water layer (0-0.1 km), the strain-sensitivity tensor is set to zero

is stiffer than the rocks of the overburden, the deviatoric strain above the reservoir tends to concentrate around the reservoir rather than spreading throughout the upper part of the model (Figure 4.11). Also, as predicted by equation 4.2, the deviatoric strain is larger above the reservoir than beneath it because of the higher P-wave velocities in two bottom layers (Figures 4.11a–c).

The volumetric strain $\Delta e_{kk}$is also largely confined to the reservoir, where it exceeds the deviatoric strain $\Delta\epsilon_{ij}$. Outside the reservoir, however, Δe_{kk} is an order of magnitude smaller than the deviatoric strain $\Delta\epsilon_{ij}$ (compare Figures 4.11a and 4.11d). Some of the features of the distribution of the volumetric strain in the layered model can be explained using equation 4.3. For instance, because Δe_{kk} is inversely proportional to both V_P^2 and to V_P^2/V_S^2, the seventh layer accumulates more volumetric strain than any other layer (except for the reservoir) due to its small $V_P/V_S = 1.6$.

Figure 4.12 summarizes the influence of the depletion-induced strains on the velocity perturbation. As expected from our previous results (Fuck et al., 2009), the initially isotropic velocity model composed of homogeneous layers becomes anisotropic with a heterogeneous velocity field in each layer. In particular, each layer becomes elliptically anisotropic with a tilted symmetry axis. Because the components C_{ijk} are much larger for the shallow layers (between 0.1 km and 2 km depth), the stress-induced velocity changes are restricted primarily to the upper half of the model (Figure 4.12a). The sign of the anisotropy's parameter $\varepsilon = \delta$ indicates that the horizontal velocity is higher than the vertical velocity outside the reservoir ($\varepsilon > 0$) and smaller inside it ($\varepsilon < 0$, Figure 4.12a). The rotation of the symmetry axis from the vertical by the shear strain does not exceed 1° (positive angles in Figure 4.12b imply clockwise rotation from the vertical).

Offset Variation of Traveltime Shifts Figure 4.13 show ray-traced and approximate traveltime shifts for a range of reflector depths for a CMP located above the reservoir center. In contrast to the results of Fuck et al. (2009) for the homogeneous model, the approximation works better for deeper reflectors because the largest velocity perturbations are concentrated in the upper half of the model.

Another factor contributing to the poor performance of the linearized approximation for reflectors at the depths 0.85 km, 1.5 km and 2 km is ray bending, which is not taken into account by equation 4.7. This bending makes the traveltimes more sensitive to the horizontal and shear components of the deviatoric strain tensor, which increases the offset variation of the exact (ray-traced) shifts. Also, the approximation deteriorates for common midpoints near the reservoir edges due to the accumulation of the shear strain around the reservoir corners (Figure 4.11b). For example, the difference between the ray-traced and approximate time shifts for the reflectors above the reservoir increases as the CMP approaches the corner of the reservoir at $x = 1$ km.

Since the velocity perturbations occur mostly above the reservoir, the largest shifts (as well as their more pronounced offset variation) are observed for the shallow reflectors, especially in CMPs located above the reservoir corner (Figure 4.14). As was the case for the "homogeneous host rock" models with a relatively rigid reservoir, the reflections from the base of the reservoir and close to it show the smallest offset variation of the shifts, particularly for CMP locations above the center of the reservoir (Figure 4.13c). The magnitude of the traveltime shifts at small offsets for the deeper reflectors (3 and 4 km) is about the same as that for the reflector immediately below the reservoir at depth 2.7 km. The offset variation of the shifts increases gradually with the depth of the interface in Figures 4.13c, 4.14e and 4.14f, because events reflected from deeper interfaces are less influenced by the almost constant velocity perturbations inside the reservoir.

Figure 4.15 shows that the traveltime shifts are mostly due to the deviatoric strain, which also controls the offset variation of the shifts both above and below the reservoir. As already observed, deviatoric strains are almost constant inside the reservoir. As a consequence, contours of traveltime shifts have large spacing beneath the reservoir in Figure 4.15. Figure 4.16 further explores this issue by showing a decomposition of the traveltime shifts into its isotropic and anisotropic components for two reflectors below the reservoir. When the CMP is located above the reservoir center, both the isotropic and anisotropic components are almost invariant with offset, especially for the base of the reservoir.

4.6.3 Influence of The Reservoir Shape

The subsurface strain distribution caused by reservoir compaction also depends on the shape of the reservoir (e.g., Faux et al., 1997). Because pore-pressure changes inside the reservoir are equilibrated, they cause the reservoir to contract equally in all directions. As a result, it should be expected that one of the principal strain directions is perpendicular to the reservoir boundaries. For example, the principal strain direction outside a cylindrical reservoir is parallel to the radius of the circular cross-section of the reservoir. Shear strains vanish outside the reservoir only along the lines parallel to the coordinate axes that go through the center of the circular reservoir cross-section (Figure 4.17a). For reservoir with elliptical cross-section, the shear strains behave in a similar way, but the strain distribution is influenced by the elongation of the ellipse. The largest rotation of the principal strain directions with respect to the vertical occurs near the area with the highest curvature of the ellipse (Figure 4.17b). As the aspect ratio of the elliptical cross-section decreases, the shear strains tend to accumulate near the reservoir end points, and the strain distribution resembles that for a reservoir with rectangular cross-section (compare Figures 4.17c and 4.17d).

Figure 4.18 shows a comparison of the vertical deviatoric strains for rectangular and elliptical reservoirs with same area and aspect ratio. The distribution and magnitude of the compaction-induced strains for both reservoirs are similar, except for the larger strain closer accumulation near the vertical edges of the rectangular reservoir.

Since the magnitude and offset variation of traveltime shifts is governed by the subsurface strain distribution, we conclude that given similar area and aspect ratio, the behavior of traveltime shifts will not substantially change with the reservoir shape (if area and aspect ratio are fixed), especially for reflectors above the reservoir.

4.7 Discussion

Since our analysis is restricted to elastic deformation, the modeled traveltime shifts result primarily from the velocity perturbations. Traveltime shifts caused by the geometric changes, however, may become significant due to the displacement of sources and receivers caused by tides. Such phenomena should be taken into account when analyzing marine time-lapse data.

We believe that taking anelastic deformation into account would not significantly change the behavior of traveltime shifts above the compacting reservoir. Indeed, Chin and Nagel (2004) show that the large compaction and subsidence at Ekofisk field can be explained by restricting anelastic deformation to the reservoir itself. Hence, the patterns of stress and strain above the reservoir should remain similar to those discussed above. For reflections from interfaces below the reservoir, the shifts are still likely to be controlled by the anisotropic velocity changes. Indeed, anelastic deformation induces fracturing inside the reservoir, which not only enhances velocity anisotropy, but also reduces seismic velocities (Sinha and Plona, 2001). This effect can potentially compensate for the increase in the isotropic velocity perturbations caused by the volumetric contraction of the reservoir.

Compaction-related deformation is treated here as a static problem. In particular, we do not consider coupling between poroelastic deformation and fluid flow inside the reservoir. Although this coupling allows for the pore-pressure inside the reservoir to be influenced by the deformation of the host rock and vice-versa (Gutierrez and Lewis, 2002), such interaction should be small over the typical intervals between time-lapse seismic surveys (i.e., a couple of years). Also, since we assumed the pore-pressure drop to be equilibrated throughout the reservoir, we did not account for spatial variations in the pore-pressure. In cases where such a variation is significant, the velocity perturbations are likely to vary substantially inside the reservoir, which may induce larger offset variations of traveltime shifts beneath the reservoir.

Finally, the paper does not address potential problems in accurately measuring traveltime shifts on field prestack seismic data. Such problems range from the repeatability of the acquisition parameters to distortions caused by measuring time shifts on partial stacks formed by near-, mid- and far-offset data.

4.8 Conclusions

We have studied the influence of heterogeneity of the background velocity model on compaction-related traveltime shifts and their variation with offset. The main goal of our numerical simulations was to verify whether prestack analysis of traveltime shifts provides useful information for reservoir characterization in the presence of background heterogeneity.

When the reservoir is embedded in a medium with different elastic properties, the contrast in the rigidity modulus μ may cause substantial changes in the compaction-related strain. The background heterogeneity changes the relative magnitude of the isotropic and anisotropic velocity perturbations that are responsible for traveltime shifts. Nevertheless, traveltime shifts are mainly governed by the anisotropic velocity changes, because the most significant isotropic velocity changes are largely restricted to the reservoir itself. Thus, stacked data are not sufficient for reconstruction of the subsurface velocity perturbations caused by the reservoir compaction.

The numerical experiments allowed us to formulate some simple “rules of thumb”. For example, the larger the deviatoric strains produced by reservoir compaction, the larger the offset variation of traveltime shifts. If the reservoir is more rigid than the host rock, then the deviatoric strains tend to increase outside the reservoir and decrease inside it. Hence, in comparison with homogeneous models, the offset variation is larger above a more rigid reservoir than below it. Conversely, the offset variation of traveltime shifts decreases above a less rigid reservoir and increases below it.

Furthermore, the geomechanical modeling for the layered medium indicates that the distribution of compaction-induced strains of more complex models is not drastically different from that of simpler ones. For example, the deviatoric strains continue to be inversely proportional to the squared P-wave velocity V_P, while the volumetric strain is also inversely proportional to V_P^2/V_S^2. Moreover, the subsurface strain patterns for models with different background are similar, despite the discontinuities in strain across layer boundaries. For instance, because the reservoir in the layered model is more rigid than the overburden, the deviatoric strain is concentrated above the reservoir, while the volumetric strain dominates inside it.

Despite the similar geomechanical behavior, deeper formations in the layered model are stiffer and less strain-sensitive. As a result, the strain-induced velocity perturbations occur mostly in the upper part of the geologic section. Therefore, the most pronounced offset-varying traveltime shifts are observed for reflections from interfaces above the reservoir, especially for those recorded in CMPs close to the reservoir edges. Finally, given similar area and small aspect ratios of reservoirs whether the reservoir is represented by a rectangular or elliptical shape, does not drastically change the subsurface patterns of strain. As a result, traveltime shifts obtained for both types of cross-section should present similar magnitudes and offset variation for equivalent shot and CMP positions.

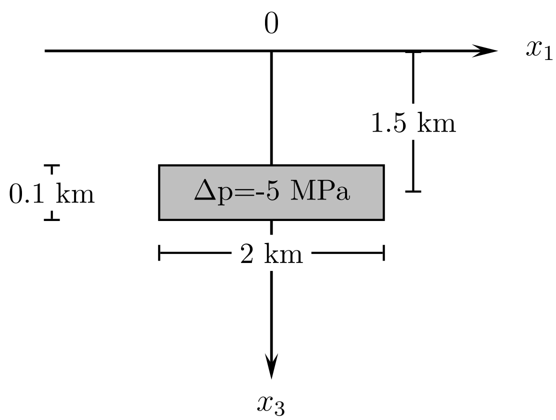

Figure 4.1. 2D model of a rectangular reservoir embedded in an isotropic homogeneous medium. The pressure drop inside the reservoir is 5 MPa. The medium parameters are taken from the laboratory data for Berea sandstone: $V_P = 2.3$ km/s, $V_P/V_S = 1.58$, $\rho = 2.14$ g/cm^3, $C_{111} = -13904$ GPa, $C_{112} = 533$ GPa and $C_{155} = -3609$ GPa. To compute the excess stress, we set the Biot-Willis coefficient α to 0.85 (the closer is α to unity, the more stress is generated by reducing the pore-pressure in the reservoir). To simulate the static stiffness coefficients, V_P was reduced by 10%, a typical difference between the static and dynamic stiffnesses for well-consolidated rocks with low porosity
.

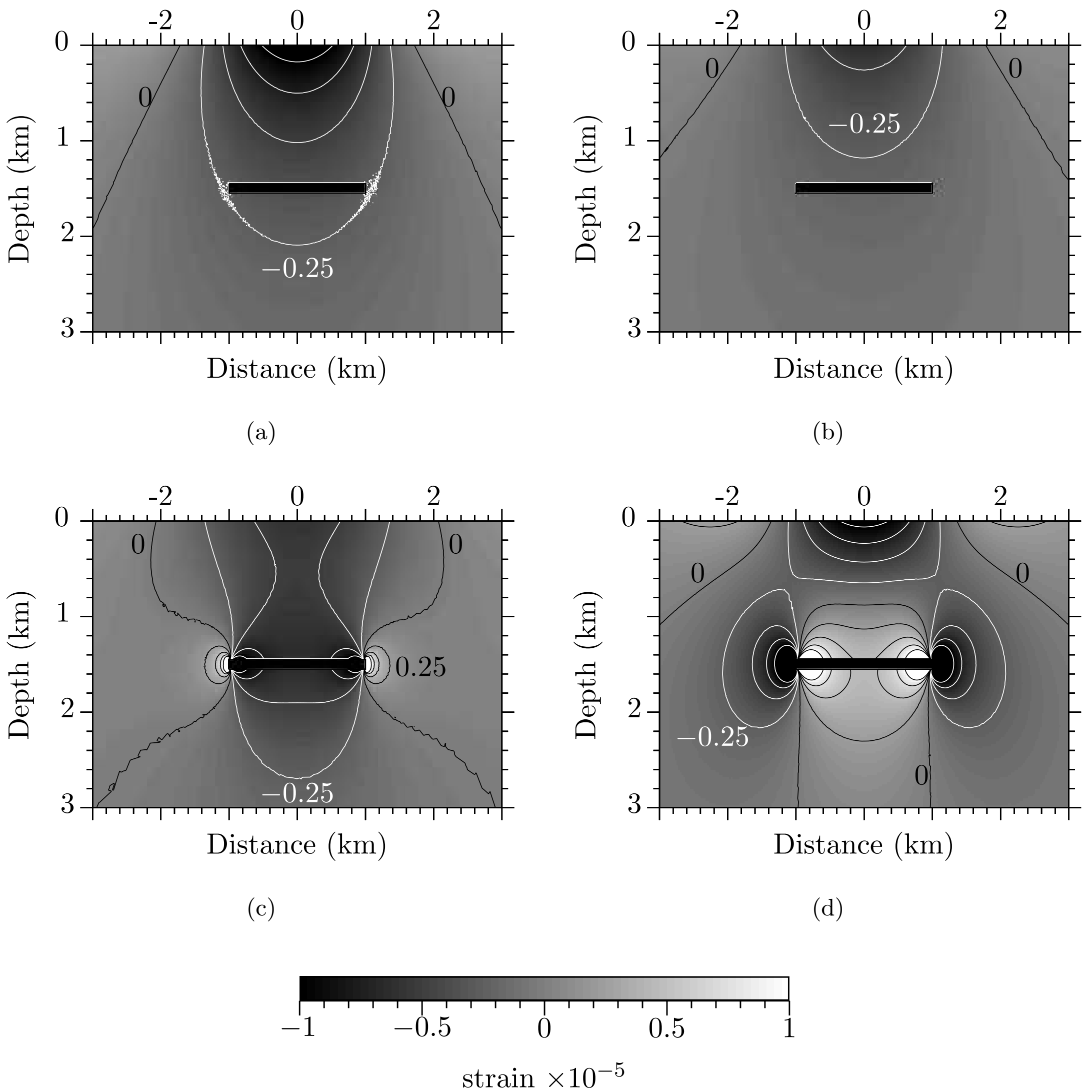

Figure 4.2. Compaction-related volumetric strain Δe_{kk} for models with different elastic contrast between the reservoir and host rock. Homogeneous background model (a) and models with b) V_P 25% higher outside the reservoir; c) V_S outside the reservoir is 20% lower than inside; d) V_S inside the reservoir is 20% lower than outside. Negative values are contoured in white, while zero and positive ones in black. The contour step is 0.25 $\times 10^{-5}$.

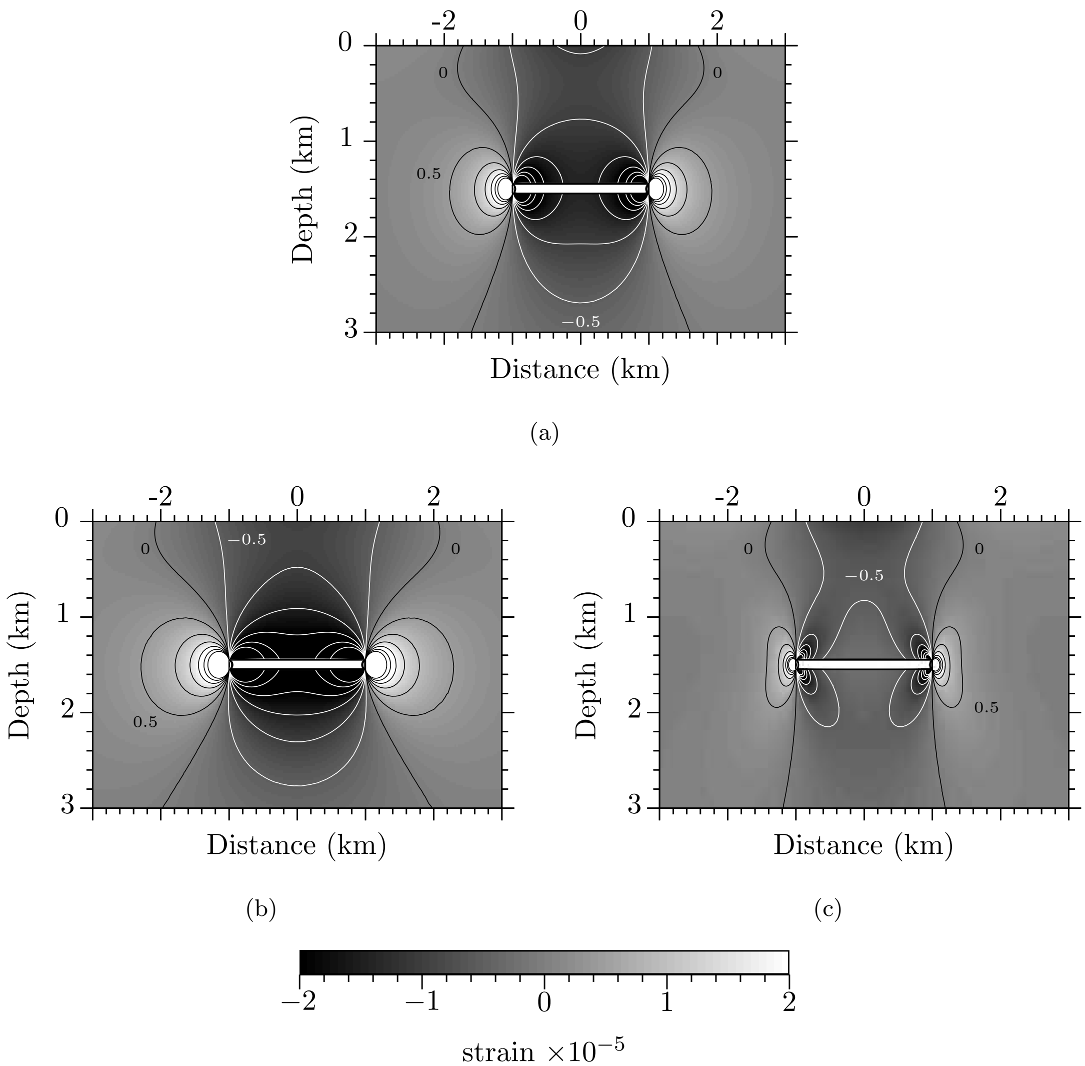

Figure 4.3. Compaction-related horizontal deviatoric strain Δe_{11}. Homogeneous background model (a) and models in which b) V_S is 20% lower outside the reservoir; c) V_S is 20% higher outside the reservoir. The contrast in μ is created by varying the V_P/V_S ratio, while holding both the density and P-wave velocity constant. The contour step is 0.5 $\times 10^{-5}$.

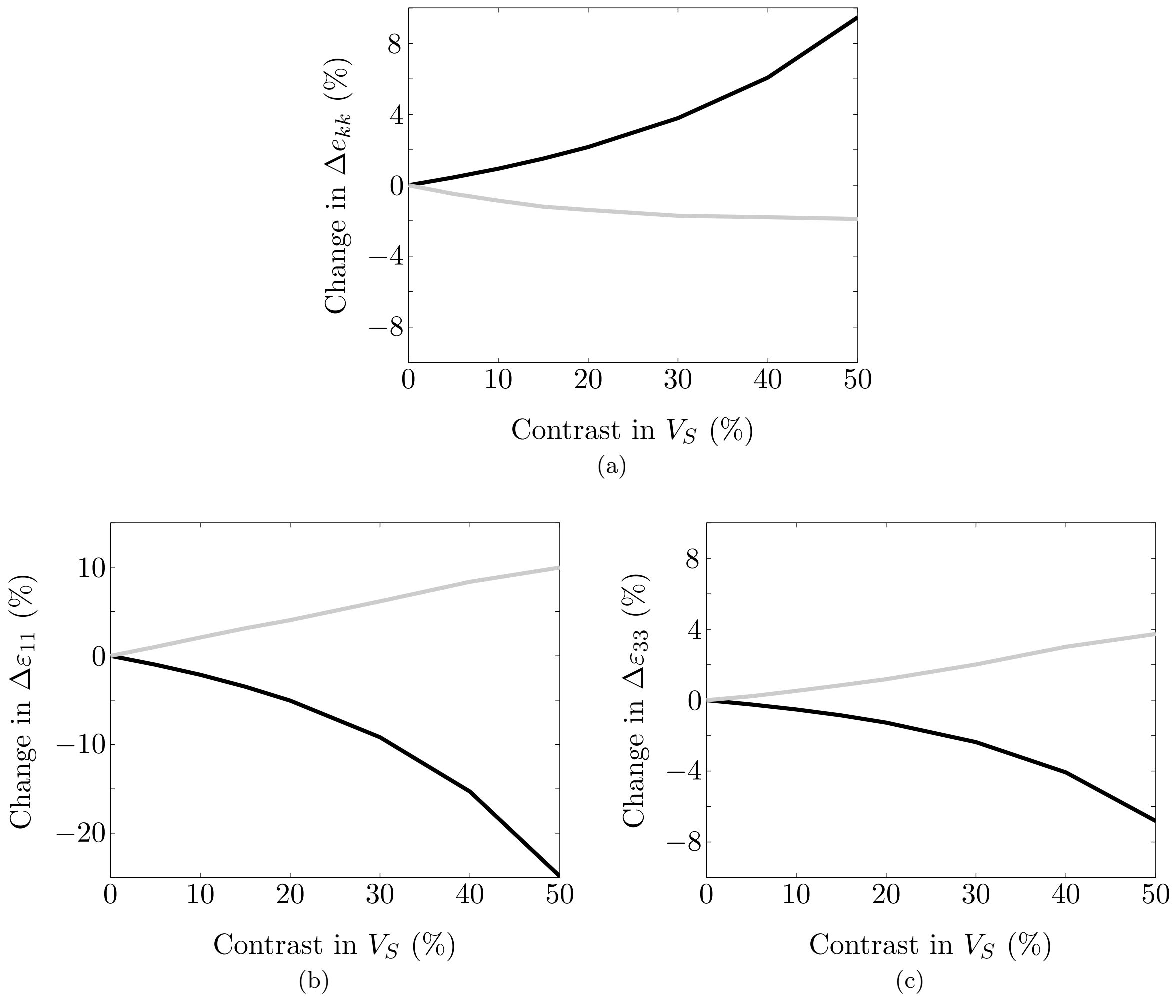

Figure 4.4. Relative strain changes at the center of the reservoir (0 km,1.5 km) compared to the homogeneous model. a) Volumetric strain; b) deviatoric horizontal strain; and c) deviatoric vertical strain. Black solid lines corresponds to reservoirs that are stiffer than host rocks; gray solid lines refer to reservoirs that are softer than host rocks . Elastic parameters of the homogeneous model are those from Figure 4.1.

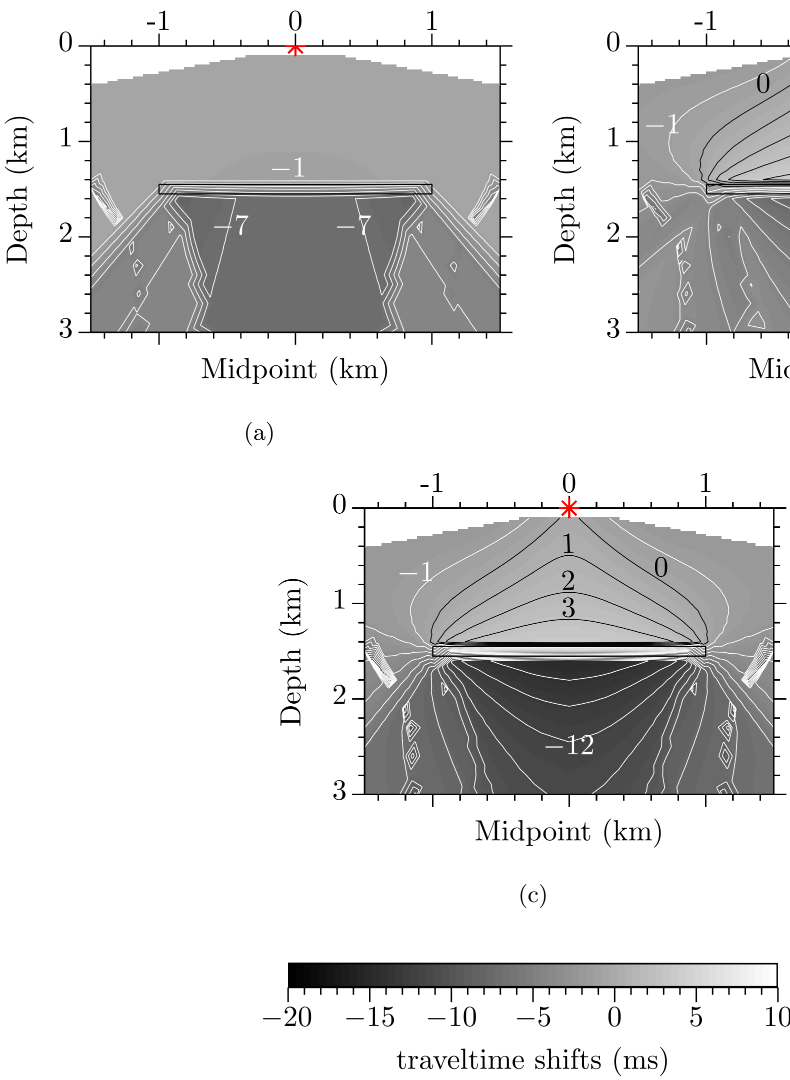

Figure 4.5. Approximate traveltime shifts for a shot above the center of the reservoir. The shift plotted at each (x,z) point would be recorded at the source-receiver offset $2x$ from an imaginary horizontal interface at depth z. The background model is heterogeneous, with V_P and V_P/V_S 25% higher outside the reservoir (i.e., no contrast in μ). Traveltime shifts caused by a) isotropic velocity changes ; b) anisotropic velocity changes; and c) total shifts.

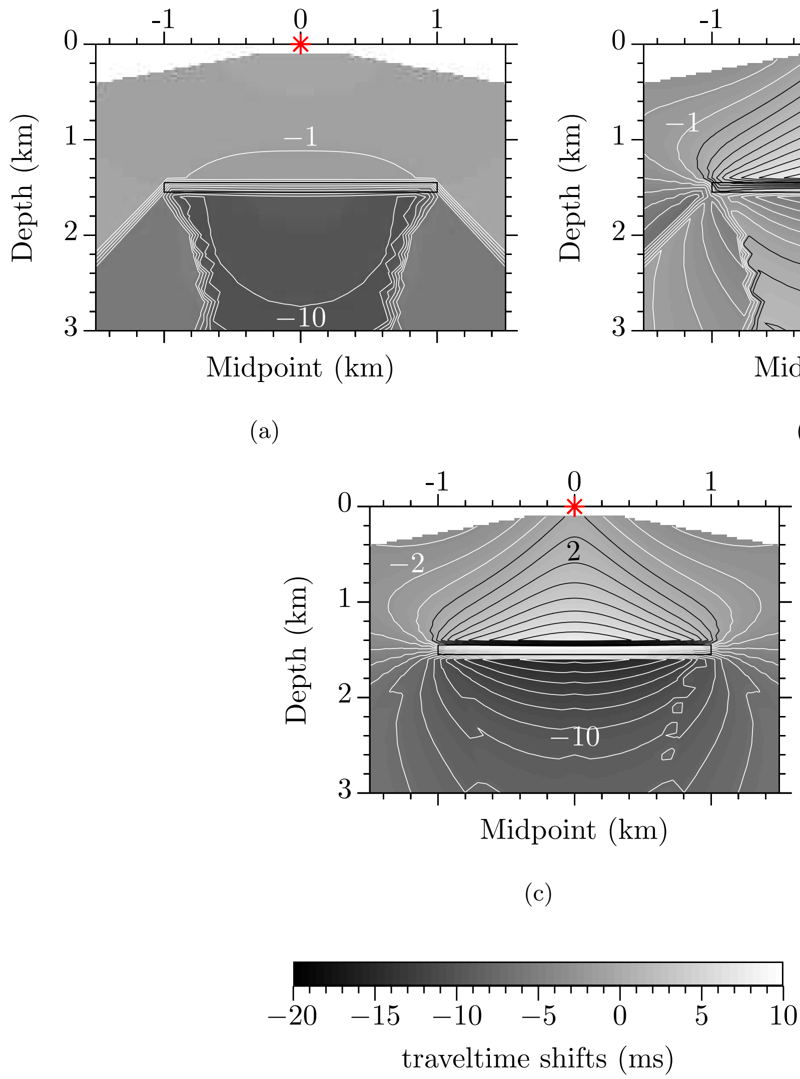

Figure 4.6. Approximate traveltime shifts for a shot above the center of the reservoir. The model is heterogeneous, with V_S 20% smaller outside the reservoir. Traveltime shifts caused by a) isotropic velocity changes, b) anisotropic velocity changes; and c) total shifts.

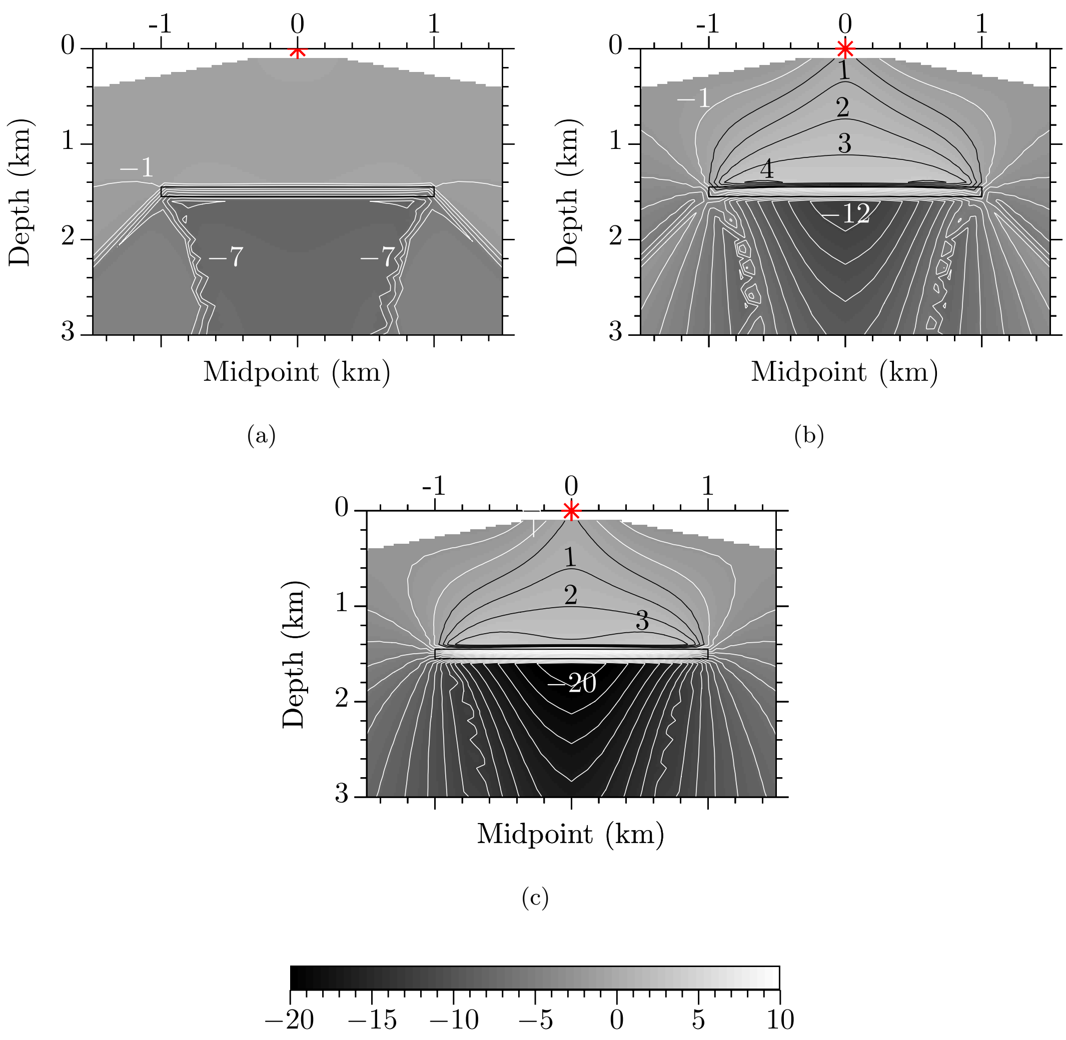

Figure 4.7. Approximate traveltime shifts for a shot above the center of the reservoir. The model is heterogeneous, with V_S 20% larger outside the reservoir. Traveltime shifts caused by a) isotropic velocity changes, b) anisotropic velocity changes; and c) total shifts.

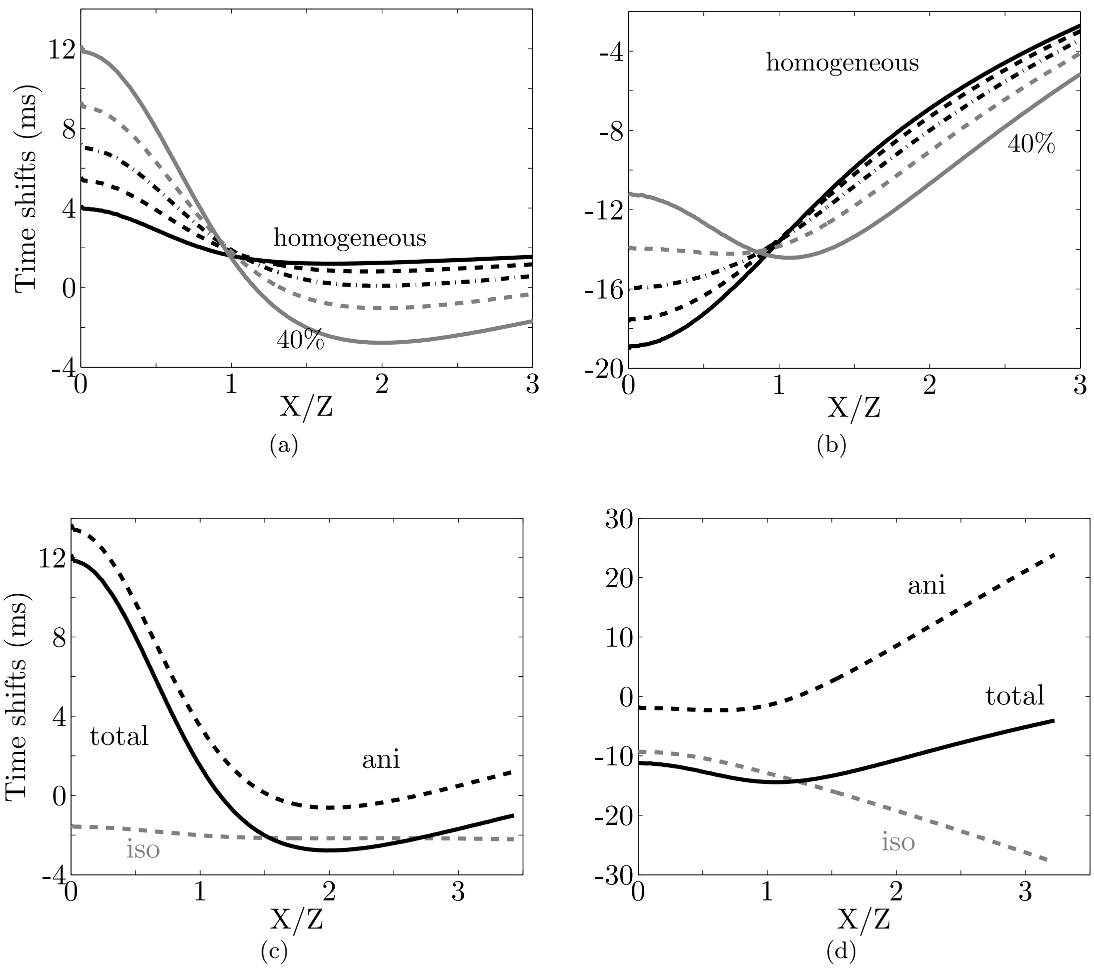

Figure 4.8. Traveltime shifts for CMP above the center of the reservoir for different contrasts in V_S (μ is larger inside the reservoir). Traveltime shifts for the a) top and b) bottom of the reservoir for the contrast in V_S varying from 0% (solid black) to 40% (solid gray line) in steps of 10%; X/Z is the offset-to-depth ratio. The decomposition of the traveltime shifts for the c) top and d) bottom of the reservoir into the isotropic (iso) and anisotropic (ani) components; the contrast in V_S is 40%.

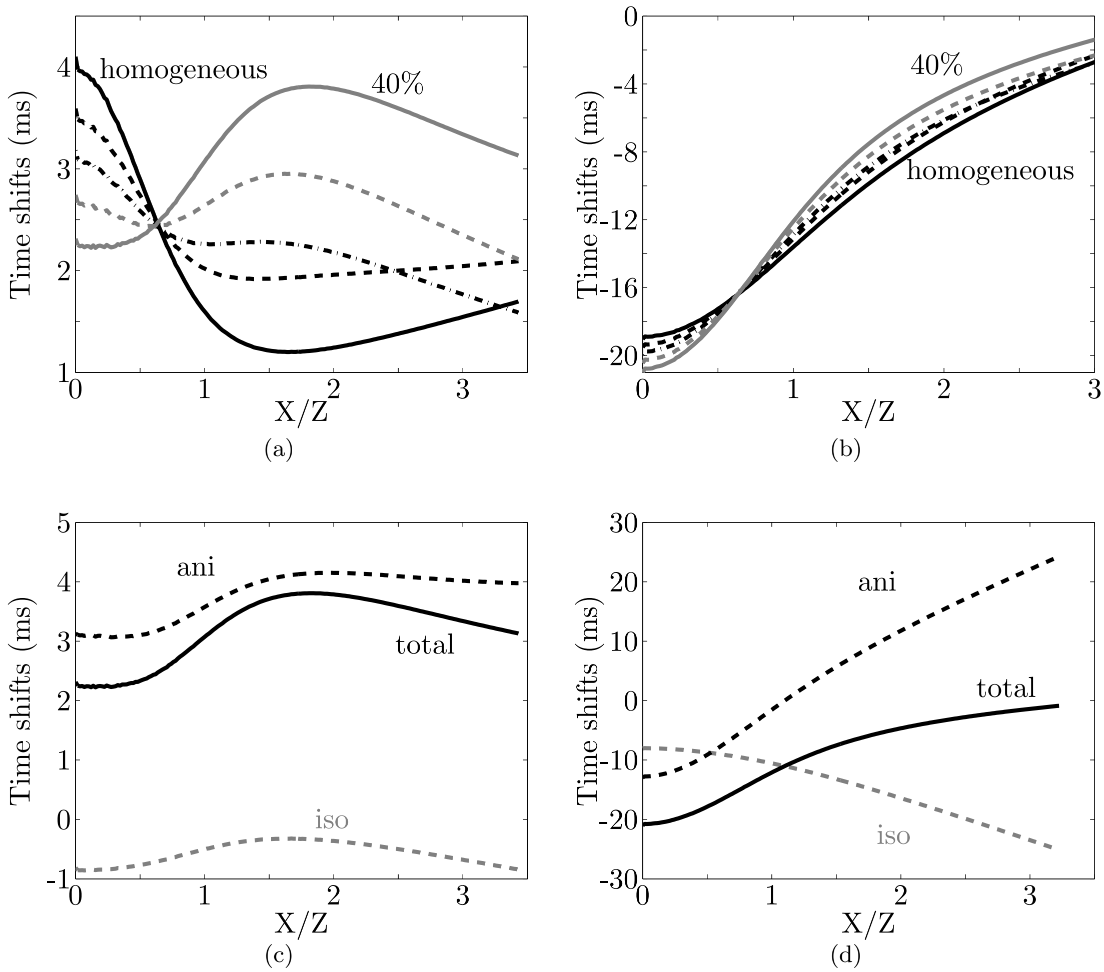

Figure 4.9. Traveltime shifts for CMP above the center of the reservoir for different contrasts in V_S (μ is smaller inside the reservoir). Traveltime shifts for the a) top and b) bottom of the reservoir for the contrast in V_S varying from 0% (solid black) to 40% (solid gray line) in steps of 10%; X/Z is the offset-to-depth ratio. The decomposition of the traveltime shifts for the c) top and d) bottom of the reservoir into the isotropic (iso) and anisotropic (ani) components; the contrast in V_S is 40%.

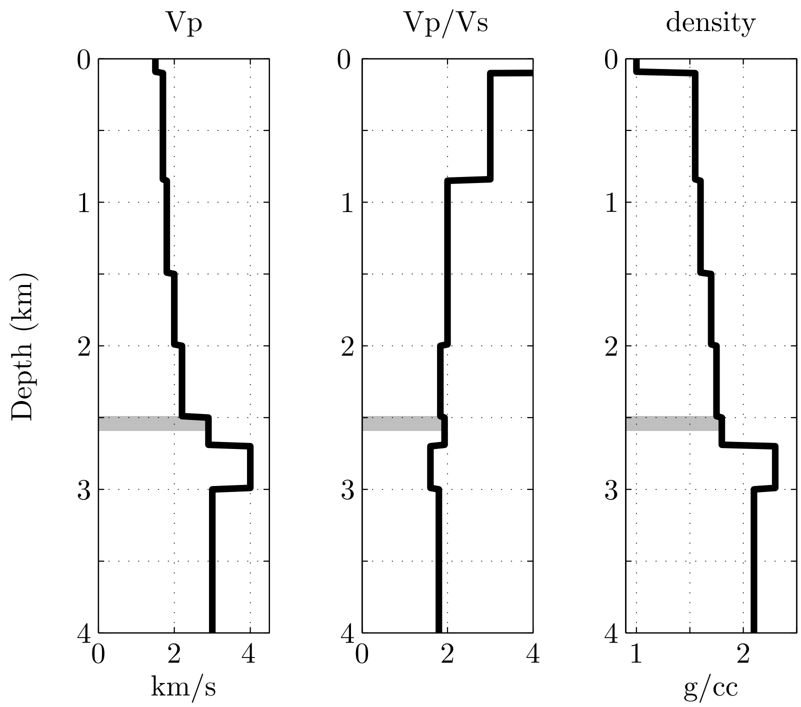

Figure 4.10. Velocity and density profiles adapted from data acquired at Valhall field in the North Sea (adapted from Røste, 2007). The model is composed of eight homogeneous layers, and the rectangular reservoir (the gray rectangle) is located within layer 6. The first layer (water) is 100 m thick, with $C_{ijk} = 0$ and $V_P/V_S = \infty$. For layers two through four, $C_{111} = -11300$ GPa, $C_{112} = -4800$ GPa and $C_{123} = 5800$. For layers five through eight, $C_{111} = -3100$ GPa, $C_{112} = -800$ GPa, and $C_{123} = 40$ GPa.

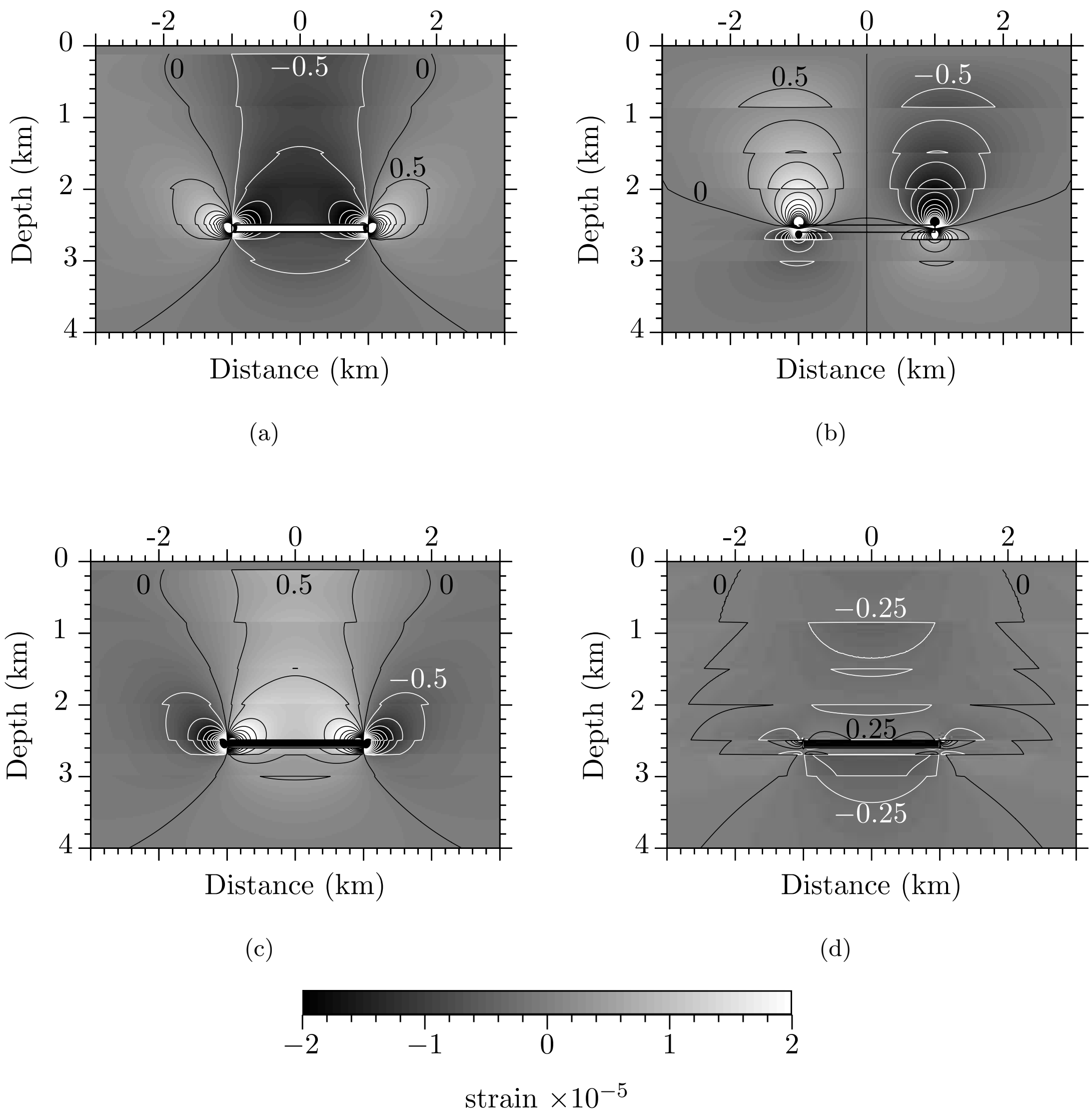

Figure 4.11. Deviatoric and volumetric strains caused by the pore-pressure drop $\Delta p = -2.5$ MPa inside the rectangular reservoir for the model from Figure 4.10. The deviatoric strains, a) $\Delta\epsilon_{11}$; b) $\Delta\epsilon_{13}$; c) $\Delta\epsilon_{33}$; and d) the volumetric strain Δe_{kk}. Negative strain values are contoured in white; zero and positive strains in black; the contour step is 0.5×10^{-5} in a), b), and c) and 0.25×10^{-5} in d). The color scale is clipped for better contrast. At the center of the reservoir (0 km,2.55 km), $\Delta\epsilon_{11} = 1.2 \times 10^{-4}$, $\Delta\epsilon_{33} = -2.5 \times 10^{-4}$ and $\Delta e_{kk} = -3.9 \times 10^{-4}$.

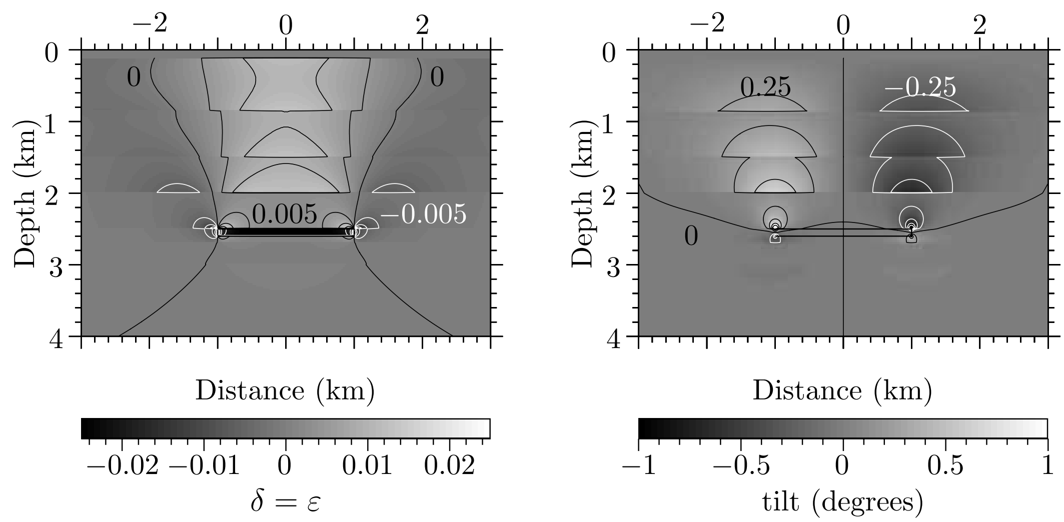

(a) (b)

Figure 4.12. Stress-induced velocity anisotropy for the layered model. a) Thomsen's parameter $\delta = \varepsilon$; b) the tilt of the symmetry axis. Positive values on both plots are contoured in black, while negative ones in white. Positive degrees mean clockwise rotation from the vertical.

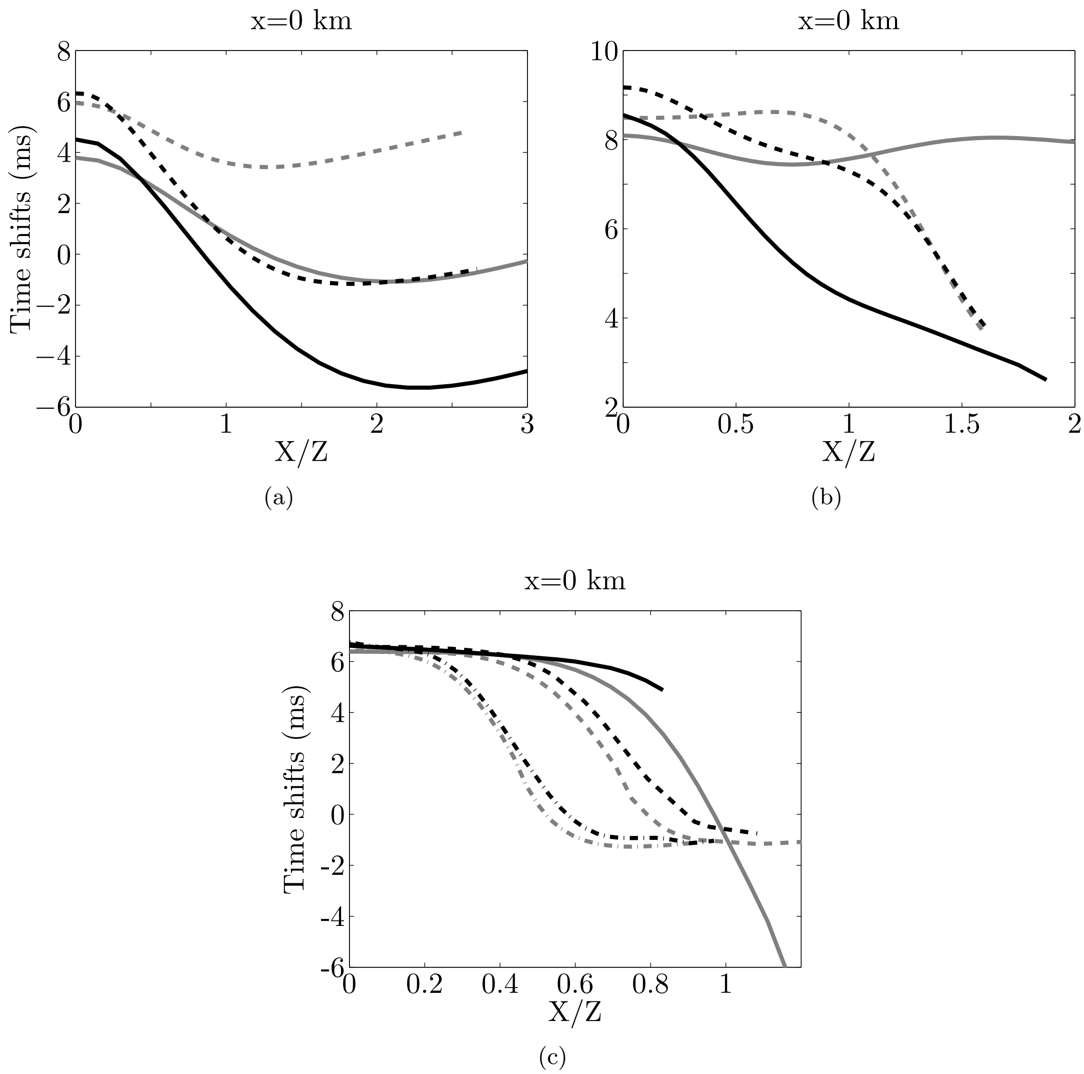

Figure 4.13. Comparison between ray-traced (black lines) and approximate traveltime shifts (gray) measured in a CMP above the reservoir center. Traveltime shifts for the reflectors at a) 0.85 km (solid lines) and 1.5 km (dashed); b) 2 km (solid) and 2.5 km (dashed); c) 2.7 km (solid), 3 km (dashed) and 4 km (dot-dashed).

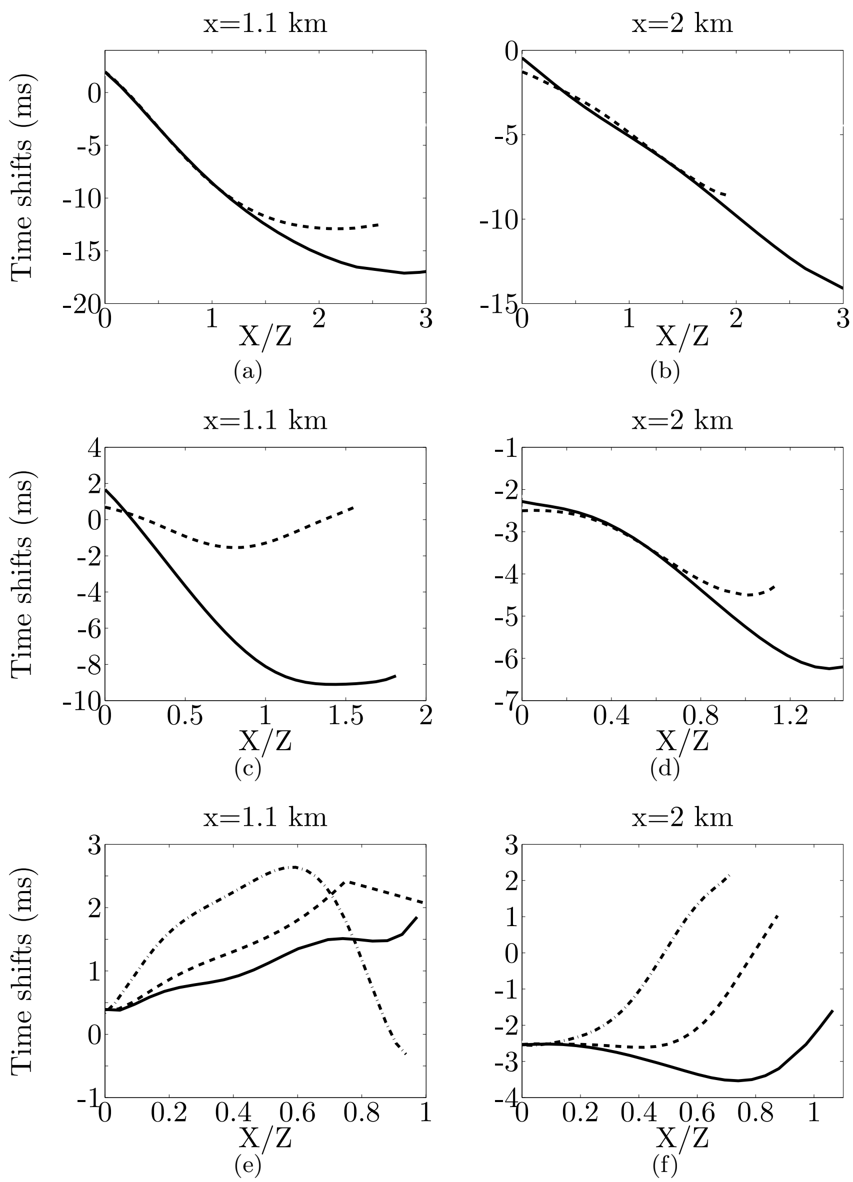

Figure 4.14. Ray-traced traveltime shifts measured in CMPs at $x = 1.1$ km (near reservoir corner) and at $x = 2$ km, for the reflectors at: a) and b), 0.85 km (solid line) and 1.5 km; c) and d), 2 km (solid) and 2.5 km (dashed); e) and f) 2.7 km (solid lines), 3 km (dashed) and 4 km (dot-dashed).

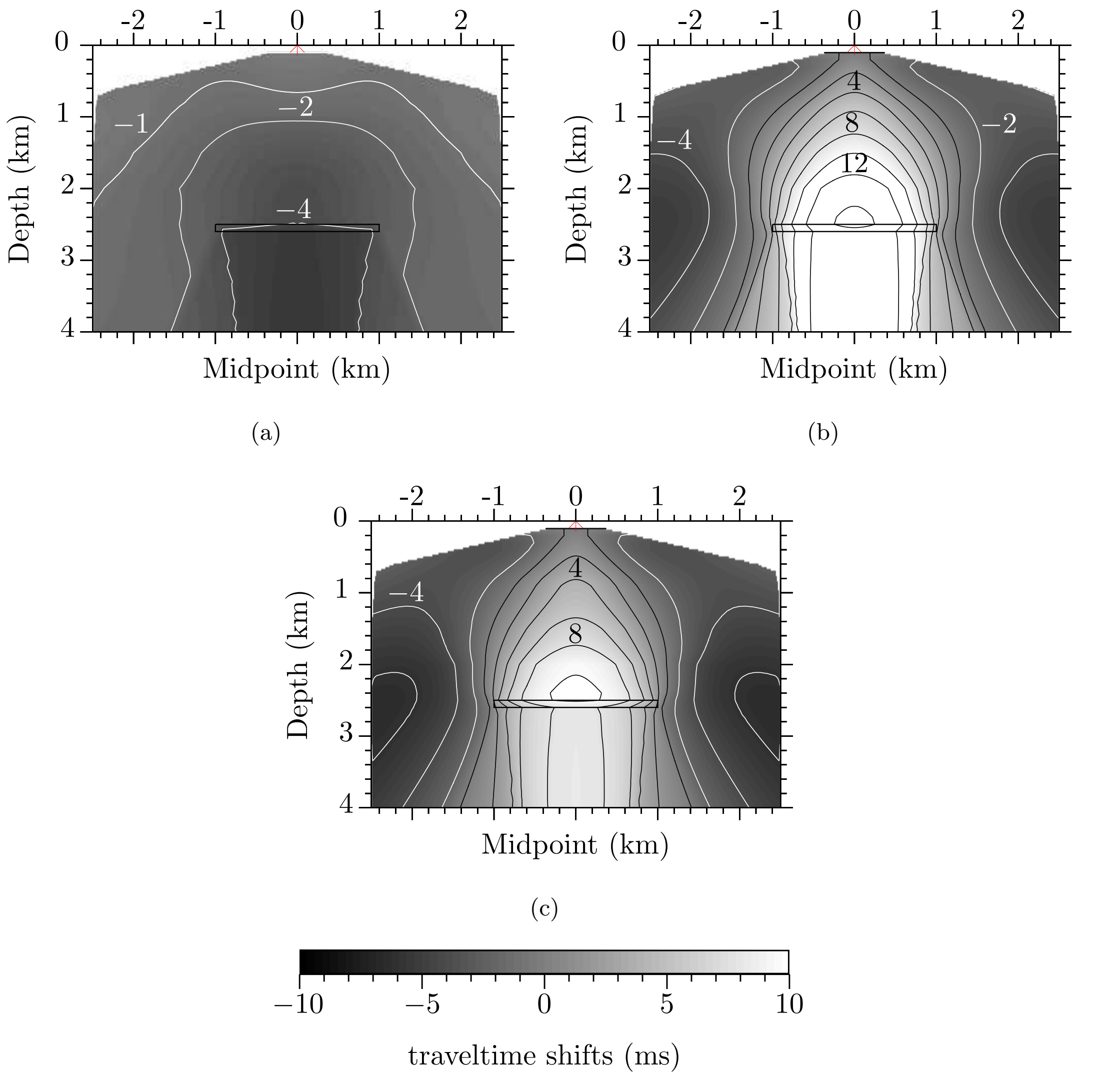

Figure 4.15. Decomposition of traveltime shifts computed from approximation 4.7 for a shot at X=0 km in the layered model. Traveltime shifts due to the a) isotropic and b) anisotropic velocity changes; c) the total traveltime shifts.

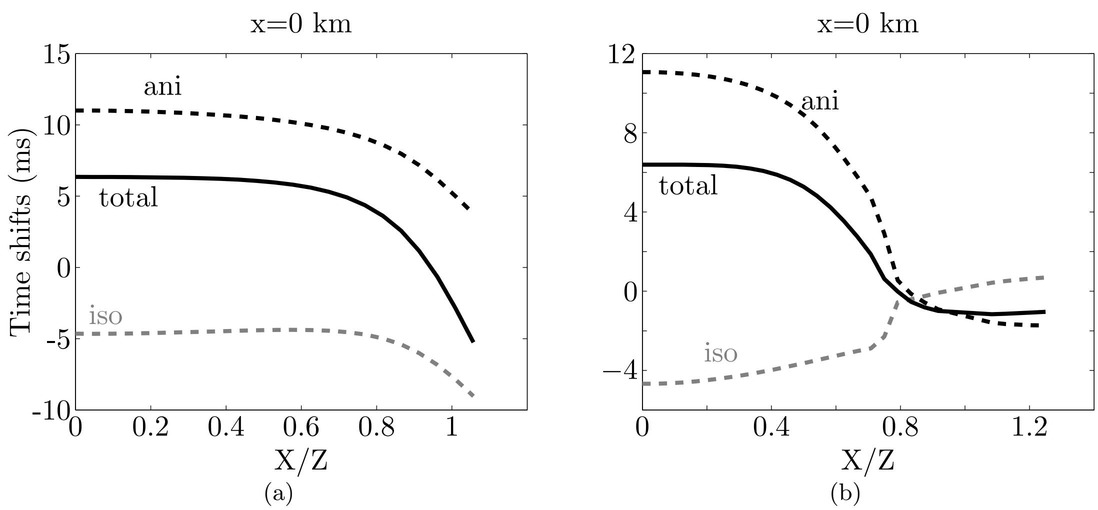

Figure 4.16. Comparison of the isotropic (iso) and anisotropic (ani) components of the traveltime shifts for the CMP above the reservoir center for events reflected from a) the base of the reservoir (2.6 km); and b) from the reflector at 3km depth.

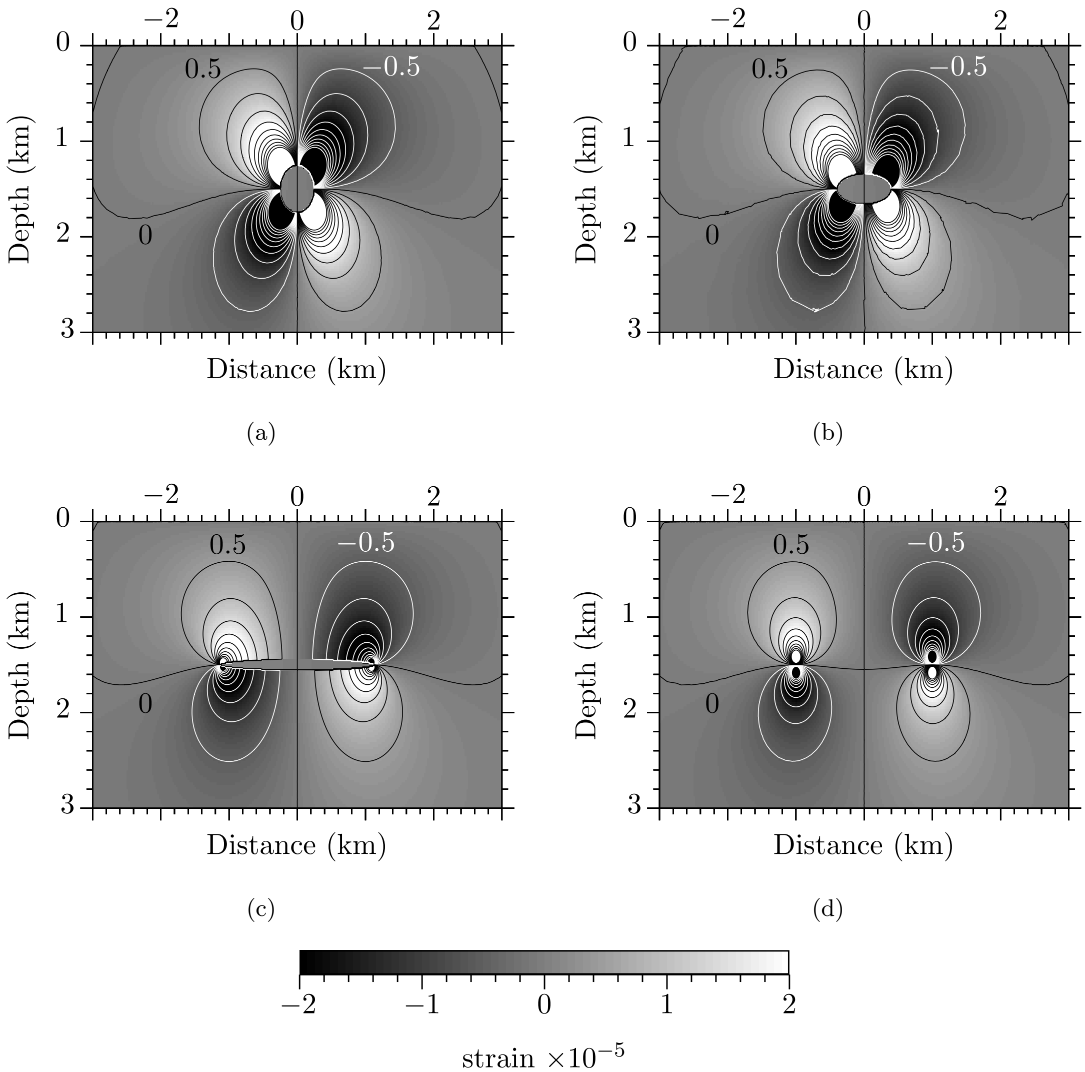

Figure 4.17. Shear strain $\Delta\varepsilon_{13}$ developed around compacting reservoirs of different shapes. The reservoir cross-section is a) circular; b) elliptical with the aspect ratio 1/4; c) elliptical with the aspect ratio 1/20; and d) rectangular with the aspect ratio 1/20; the area of the cross-sections is fixed. The model parameters are taken from Figure 4.1, with no elastic contrast between the reservoir and host rock (i.e., the background is homogeneous).

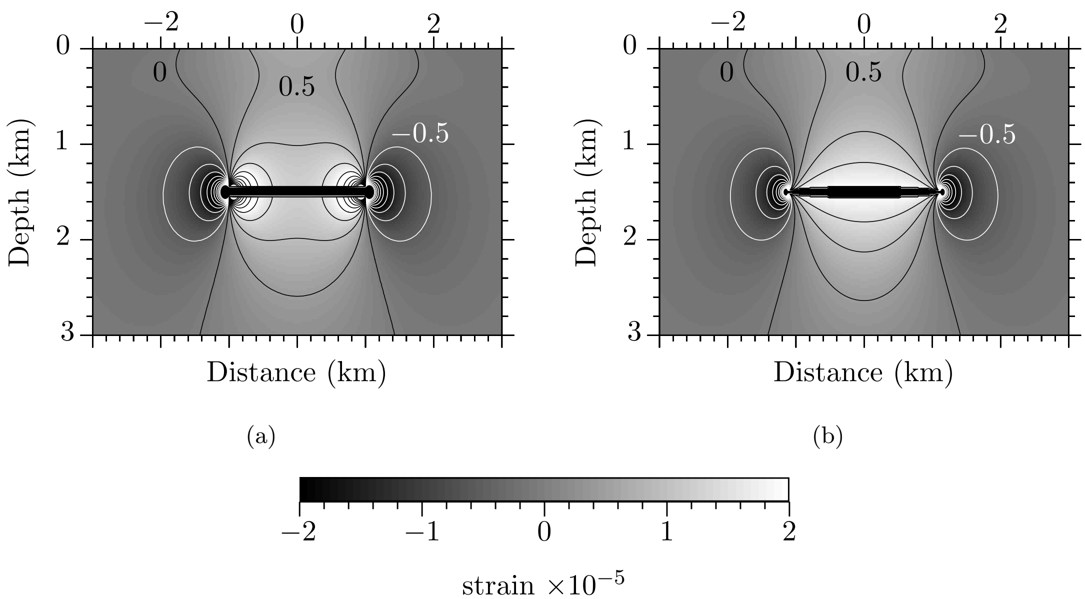

Figure 4.18. Vertical deviatoric strain $\Delta\varepsilon_{33}$ for reservoirs with a) rectangular and b) elliptical cross-sections. The area of the cross-section and its aspect ratio (1/20) are the same. The model parameters are taken from Figure 4.1.

Chapter 5

Analysis of the symmetry of a strained medium using nonlinear elasticity

5.1 Summary

Velocity variations caused by subsurface stress/strain changes play an important role in monitoring compacting reservoirs and in several other applications of seismic methods. The most general way of describing strain-induced velocity fields is by employing the theory of nonlinear elasticity, which operates with third-order elastic (TOE) tensors. These sixth-rank strain-sensitivity tensors, however, are difficult to manipulate because of the large number of terms involved in the algebraic operations. Thus, even evaluation of the anisotropic symmetry of a medium under stress/strain proves to be a challenging task. Here, we introduce a matrix representation of TOE tensors that allows computation of strain-related stiffness perturbations from a linear combination of 6×6 matrices scaled by the components of the strain tensor. In addition to streamlining the numerical algorithm, our approach helps to predict the strain-induced symmetry using relatively straightforward algebraic considerations. For example, our analysis shows that a transversely isotropic (TI) medium acquires orthorhombic symmetry if one of the principal directions of the strain tensor is aligned with the symmetry axis. Otherwise, the strained TI medium can become monoclinic or even triclinic.

5.2 Introduction

Monitoring subsurface stress/strain fields and their time-lapse variations is an important research area with applications in velocity model-building (e.g., Sengupta and Bachrach, 2008) and reservoir geophysics (e.g., Fuck et al., 2009). For example, pore-pressure drop due to hydrocarbon production leads to reservoir compaction, which produces excess stress and strain not only in the reservoir itself, but also in the surrounding rock mass.

Seismic velocities can help to monitor subsurface stress and strain because numerous laboratory experiments have demonstrated that the stiffness tensor changes under stress/strain (Eberhart-Phillips et al., 1989; Prasad and Manghnani, 1997). In the elastic regime, stress stiffens grain contacts and closes fractures, making rocks more rigid and increasing P- and S-wave velocities. Therefore, some theoretical models describe the stress/strain sensitivity of seismic velocities through the stiffening of grain contacts (e.g., Gassman and Hertz-Mindlin models discussed in Mavko et al., 1998), while others relate the velocity variation to closing (or opening) of microcracks (e.g., Mavko et al., 1995; Sayers, 2006).

An alternative approach that has been successfully applied to this problem is based on the nonlinear theory of elasticity (e.g. Sinha and Kostek, 1996; Winkler et al., 1998; Sinha and Plona, 2001). In contrast to the Hertz-Mindlin theory, it employs a Taylor series expansion that yields the full elastic tensor of the strained medium (Brugger, 1964). Unlike fracture-based models, nonlinear elasticity operates not with the fracture orientations and compliances, but with a third-order elastic (TOE) tensor responsible for the strain sensitivity of the rock mass.

We start by reviewing the nonlinear theory of elasticity and application of TOE tensors to model strain-induced velocity changes. Then we use Voigt notation to represent TOE tensors as $6 \times 6 \times 6$ matrices and analyze the structure of these matrices for several common symmetry classes. This matrix representation naturally leads to an algebraic method to predict the anisotropic symmetry of the strained medium from the symmetry of the TOE tensor and the structure of the strain tensor. We use the proposed method to study the symmetry of a wide range of strain-induced velocity models obtained by combining triclinic, monoclinic, orthorhombic, hexagonal and isotropic TOE tensors with several types of the strain tensor.

5.3 Physical Meaning of TOE Tensors

The nonlinear theory of elasticity (e.g. Prioul et al., 2004), provides the most general way to model strain-induced velocity changes. The stiffness coefficients c_{ijkl} (each index runs from 1 to 3) of a medium under stress/strain can be expressed in terms of the stiffnesses (c°_{ijkl}) of the undeformed medium and the applied strains (Δe_{ij}) and stresses (ΔS_{ij}):

$$c_{ijkl} = c^{\circ}_{ijkl} + c_{ijklmn}\Delta e_{mn} + \Delta S_{ik}\delta_{jl} + c^{\circ}_{ijpl}\Delta e_{kp} + c^{\circ}_{ipkl}\Delta e_{jp}\,, \tag{5.1}$$

where the summation convention over repeated indices is implied, and δ_{jl} is Kronecker's symbol. The elements c_{ijklmn} form the so-called third-order elastic (TOE) tensor, which appears in the Taylor series expansion of the strain-energy function W (Hearmon, 1953):

$$W = W^{\circ} + S_{ij}e_{ij} + \frac{1}{2}c_{ijkl}e_{ij}e_{kl} + \frac{1}{6}c_{ijklmn}e_{ij}e_{kl}e_{mn} + O(e^4_{ij})\,. \tag{5.2}$$

Ultrasonic experiments in rocks have shown that typically $\Delta S_{ij} \ll c_{ijkl} \ll c_{ijklmn}$ (Johnson and Rasolofosaon, 1996; Prioul et al., 2004), so the largest perturbation term in equation 5.1 is the one that contains the tensor c_{ijklmn}. Therefore, equation 5.1 can be simplified to

$$\begin{aligned} c_{ijkl} &= c^{\circ}_{ijkl} + c_{ijklmn}\,\Delta e_{mn} \\ &= c^{\circ}_{ijkl} + \Delta c_{ijkl}\,. \end{aligned} \tag{5.3}$$

According to approximation 5.3, the symmetry of the resulting stiffness tensor c_{ijkl} depends on the symmetries of the background medium (c°_{ijkl}) and the TOE tensor c_{ijklmn}, as well as on the structure of the strain tensor Δe_{mn}.

The large number of terms involved in equation 5.3 obscures the influence of the TOE and strain tensors on the stiffness perturbation Δc_{ijkl}. To facilitate analysis of strain-induced anisotropy, below we introduce a matrix representation of the main symmetry groups of the TOE tensor and recast equation 5.3 as a matrix-vector expression.

5.4 Symmetry of The TOE Tensor

By analogy with the geometric symmetry of crystals, elastic tensors can be classified into different symmetry groups in accordance with the invariance of their components with respect to certain rotations of the coordinate frame (e.g., Helbig, 1994). Because of the symmetry of the strain and stress tensors, the coefficients c_{ijklmn} are invariant with respect to the permutation of the indices i and j, k and l, m and n. Hence, TOE tensors can be represented using Voigt notation, which maps every pair of indices ij into a single index α varying from 1 to 6:

$$\alpha = i\delta_{ij} + (9 - i - j)(1 - \delta_{ij})\,, \tag{5.4}$$

which yields

$$\begin{aligned} &11 \mapsto 1; \quad 22 \mapsto 2; \quad 33 \mapsto 3; \\ &12 \mapsto 6; \quad 13 \mapsto 5; \quad 23 \mapsto 4\,. \end{aligned} \tag{5.5}$$

In addition, because the strain-energy function W is invariant with respect to coordinate transformations, the coefficients c_{ijklmn} remain the same if the pairs ij, kl and mn are interchanged. In Voigt notation these symmetries can be succinctly written as

$$C_{\alpha\beta\gamma} = C_{\beta\gamma\alpha} = C_{\gamma\beta\alpha} = C_{\beta\alpha\gamma}\,. \tag{5.6}$$

Application of Voigt notation to second-order elastic (SOE) tensors c_{ijkl} helps to replace them by symmetric 6×6 matrices (e.g., Helbig, 1994). Likewise, TOE tensors expressed in Voigt notation are represented by $6 \times 6 \times 6$ matrices or a six-element vector composed of 6×6 matrices:

$$C_{\alpha(\beta\gamma)} = \left(C_{1(\beta\gamma)}\,, C_{2(\beta\gamma)}\,, C_{3(\beta\gamma)}\,, C_{4(\beta\gamma)}\,, C_{5(\beta\gamma)}\,, C_{6(\beta\gamma)}\right)^{\mathsf{T}}\,. \tag{5.7}$$

Fumi (1951, 1952) and Hearmon (1953) describe the linearly independent elements of the TOE tensor for all possible symmetry classes. Here, we use their results to construct the matrix representation for several symmetries relevant in the context of exploration geophysics. We proceed from the lowest possible symmetry (triclinic), which is characterized by the absence of any symmetry elements (i.e., symmetry axes or planes), to the isotropic tensor, which is invariant with respect to any coordinate transformation. A more detailed analysis of the matrices $C_{\alpha\beta\gamma}$ for various symmetry classes can be found in Appendix G.

5.4.1 Triclinic Symmetry

Although the triclinic TOE tensor contains no symmetry elements, only 56 out of a total of $3^6 = 729$ elements are independent (equation 5.6). All six matrices that form the vector $C_{\alpha(\beta\gamma)}$ in equation 5.7 are symmetric because the indices β and γ can be interchanged:

$$C_{\alpha(\beta\gamma)} = \begin{pmatrix} C_{\alpha 11} & C_{\alpha 12} & C_{\alpha 13} & C_{\alpha 14} & C_{\alpha 15} & C_{\alpha 16} \\ C_{\alpha 12} & C_{\alpha 22} & C_{\alpha 23} & C_{\alpha 24} & C_{\alpha 25} & C_{\alpha 26} \\ C_{\alpha 13} & C_{\alpha 23} & C_{\alpha 33} & C_{\alpha 34} & C_{\alpha 35} & C_{\alpha 36} \\ C_{\alpha 14} & C_{\alpha 24} & C_{\alpha 34} & C_{\alpha 44} & C_{\alpha 45} & C_{\alpha 46} \\ C_{\alpha 15} & C_{\alpha 25} & C_{\alpha 35} & C_{\alpha 45} & C_{\alpha 55} & C_{\alpha 56} \\ C_{\alpha 16} & C_{\alpha 26} & C_{\alpha 36} & C_{\alpha 46} & C_{\alpha 56} & C_{\alpha 66} \end{pmatrix}; \tag{5.8}$$

$\alpha = 1, 2 \ldots, 6.$

5.4.2 Monoclinic Symmetry

The matrix representation of monoclinic TOE tensors can be derived from equation 5.8 by defining either a plane of mirror symmetry or a 2-fold symmetry axis (Winterstein, 1990).[1] The independent elements $C_{\alpha\beta\gamma}$ are invariant with respect to rotation by $\theta = \pi$ around the symmetry axis; the same set of independent $C_{\alpha\beta\gamma}$ can be obtained by using a symmetry plane perpendicular to this axis. If the horizontal plane $[x_1, x_2]$ is the plane of symmetry, the monoclinic TOE matrices for $\alpha = 1$, 2, 3, and 6 have the following form (Appendix G):

$$C_{\alpha(\beta\gamma)} = \begin{pmatrix} C_{\alpha 11} & C_{\alpha 12} & C_{\alpha 13} & 0 & 0 & C_{\alpha 16} \\ C_{\alpha 12} & C_{\alpha 22} & C_{\alpha 23} & 0 & 0 & C_{\alpha 26} \\ C_{\alpha 13} & C_{\alpha 23} & C_{\alpha 33} & 0 & 0 & C_{\alpha 36} \\ 0 & 0 & 0 & C_{\alpha 44} & C_{\alpha 45} & 0 \\ 0 & 0 & 0 & C_{\alpha 45} & C_{\alpha 55} & 0 \\ C_{\alpha 16} & C_{\alpha 26} & C_{\alpha 36} & 0 & 0 & C_{\alpha 66} \end{pmatrix}. \tag{5.9}$$

When $\alpha = 4$ or 5,

$$C_{\alpha(\beta\gamma)} = \begin{pmatrix} 0 & 0 & 0 & C_{\alpha 14} & C_{\alpha 15} & 0 \\ 0 & 0 & 0 & C_{\alpha 24} & C_{\alpha 25} & 0 \\ 0 & 0 & 0 & C_{\alpha 34} & C_{\alpha 35} & 0 \\ C_{\alpha 14} & C_{\alpha 24} & C_{\alpha 34} & 0 & 0 & C_{\alpha 46} \\ C_{\alpha 15} & C_{\alpha 25} & C_{\alpha 35} & 0 & 0 & C_{\alpha 56} \\ 0 & 0 & 0 & C_{\alpha 46} & C_{\alpha 56} & 0 \end{pmatrix}. \tag{5.10}$$

[1] A direction is called a k-fold symmetry axis when a tensor is invariant with respect to rotations by $\theta = 2\pi/k$ around it (Helbig, 1994).

Interestingly, the matrices described by equation 5.9 have the same structure (i.e., the same nonzero elements) as the matrix representing the monoclinic SOE tensor (e.g., Helbig, 1994). The matrices in equation 5.10, however, contain nonzero elements in place of the vanishing elements in equation 5.9. According to equations 5.9 and 5.10, the total number of independent $C_{\alpha\beta\gamma}$ for monoclinic symmetry is 32.

5.4.3 Orthorhombic Symmetry

Orthorhombic symmetry is characterized by three orthogonal 2-fold symmetry axes, or, correspondingly, by three orthogonal mirror symmetry planes (Helbig, 1994). Because orthorhombic symmetry is a special case of the monoclinic model, the matrix representation of the orthorhombic TOE tensor can be obtained from equations 5.9 and 5.10 by requiring invariance with respect to rotations by $\theta = \pi$ around the x_1- and x_2-axes. These constraints reduce the number of independent elements to 20, and the orthorhombic matrices $C_{\alpha\beta\gamma}$ can be written as (see Appendix G)

$$C_{\alpha(\beta\gamma)} = \begin{pmatrix} C_{\alpha 11} & C_{\alpha 12} & C_{\alpha 13} & 0 & 0 & 0 \\ C_{\alpha 12} & C_{\alpha 22} & C_{\alpha 23} & 0 & 0 & 0 \\ C_{\alpha 13} & C_{\alpha 23} & C_{\alpha 33} & 0 & 0 & 0 \\ 0 & 0 & 0 & C_{\alpha 44} & 0 & 0 \\ 0 & 0 & 0 & 0 & C_{\alpha 55} & 0 \\ 0 & 0 & 0 & 0 & 0 & C_{\alpha 66} \end{pmatrix}, \tag{5.11}$$

when $\alpha = 1$, 2, and 3. For $\alpha = 4$, 5, and 6,

$$C_{4(\beta\gamma)} = \begin{pmatrix} 0 & 0 & 0 & C_{144} & 0 & 0 \\ 0 & 0 & 0 & C_{244} & 0 & 0 \\ 0 & 0 & 0 & C_{344} & 0 & 0 \\ C_{144} & C_{244} & C_{344} & 0 & 0 & 0 \\ 0 & 0 & 0 & 0 & 0 & C_{456} \\ 0 & 0 & 0 & 0 & C_{456} & 0 \end{pmatrix}, \tag{5.12}$$

$$C_{5(\beta\gamma)} = \begin{pmatrix} 0 & 0 & 0 & 0 & C_{155} & 0 \\ 0 & 0 & 0 & 0 & C_{255} & 0 \\ 0 & 0 & 0 & 0 & C_{355} & 0 \\ 0 & 0 & 0 & 0 & 0 & C_{456} \\ C_{155} & C_{255} & C_{355} & 0 & 0 & 0 \\ 0 & 0 & 0 & C_{456} & 0 & 0 \end{pmatrix}, \tag{5.13}$$

$$C_{6(\beta\gamma)} = \begin{pmatrix} 0 & 0 & 0 & 0 & 0 & C_{166} \\ 0 & 0 & 0 & 0 & 0 & C_{266} \\ 0 & 0 & 0 & 0 & 0 & C_{366} \\ 0 & 0 & 0 & 0 & C_{456} & 0 \\ 0 & 0 & 0 & C_{456} & 0 & 0 \\ C_{166} & C_{266} & C_{366} & 0 & 0 & 0 \end{pmatrix} . \tag{5.14}$$

As was the case for monoclinic symmetry, the matrices $C_{\alpha\beta\gamma}$ with $\alpha = 1, 2$ and 3 have the same structure (i.e., the same nonzero elements) as the orthorhombic SOE matrix.

5.4.4 Hexagonal Symmetry

According to Hearmon (1953), there are two types of TOE tensors with hexagonal symmetry. The first type is defined by a 6-fold symmetry axis perpendicular to a mirror symmetry plane. The second (higher symmetry) type is obtained from the orthorhombic model by introducing a 6-fold symmetry axis perpendicular to one of the three orthogonal symmetry planes. Hereafter, we consider only TOE tensors of the second type.

The independent elements $C_{\alpha\beta\gamma}$ for type 2 hexagonal symmetry can be found by requiring that the matrix elements in equations 5.11–5.14 remain invariant with respect to a $2\pi/3$ rotation around the 6-fold symmetry axis, here assumed to point in the x_3-direction (more details are given in Appendix G). Note that if a certain element is invariant with respect to rotations of both $\theta = \pi$ (which is the case for the orthorhombic TOE tensor) and $\theta = 2\pi/3$ around the same axis, then it is also invariant with respect to rotations of $\theta = 2\pi/6 = \pi/3$.

Except for the matrix $C_{3(\beta\gamma)}$, all other matrices representing the TOE tensor with hexagonal symmetry have the same structure as those in equations 5.11–5.14. For hexagonal symmetry, however, the number of independent elements reduces to 10. The additional constraints are as follows[2]:

$$C_{112} = C_{111} - C_{166} - 3C_{266} \, ; \tag{5.15}$$
$$C_{122} = C_{111} - 2C_{166} - 2C_{266} \, ; \tag{5.16}$$
$$C_{222} = C_{111} + C_{166} - C_{266} \, ; \tag{5.17}$$
$$C_{223} = C_{113} \, ; \tag{5.18}$$
$$C_{233} = C_{133} \, ; \tag{5.19}$$
$$C_{123} = C_{113} - 2C_{366} \, ; \tag{5.20}$$
$$C_{244} = C_{155} = C_{144} + 2C_{456} \, ; \tag{5.21}$$
$$C_{255} = C_{144} \, ; \tag{5.22}$$
$$C_{355} = C_{344} \, . \tag{5.23}$$

Equations 5.15–5.23 include nine independent elements of the TOE tensor; the tenth independent element is C_{333}. Despite these constraints, $C_{1(\beta\gamma)}$ and $C_{2(\beta\gamma)}$ still retain the

[2]These constraints are obtained from the scheme of Fumi (1952), as discussed in Appendix G.

structure of the SOE matrix with orthorhombic symmetry. The matrix $C_{3(\beta\gamma)}$, on the other hand, has the VTI (transversely isotropic with a vertical symmetry axis) form:

$$C_{3(\beta\gamma)} = \begin{pmatrix} C_{113} & C_{123} & C_{133} & 0 & 0 & 0 \\ C_{123} & C_{113} & C_{133} & 0 & 0 & 0 \\ C_{133} & C_{133} & C_{333} & 0 & 0 & 0 \\ 0 & 0 & 0 & C_{344} & 0 & 0 \\ 0 & 0 & 0 & 0 & C_{344} & 0 \\ 0 & 0 & 0 & 0 & 0 & C_{366} \end{pmatrix} . \tag{5.24}$$

Thus, $C_{3(\beta\gamma)}$ does not have the same structure as $C_{1(\beta\gamma)}$ and $C_{2(\beta\gamma)}$, as was the case for the lower symmetries. It should be emphasized that in contrast to hexagonal SOE tensors, TOE tensors considered here are not "transversely isotropic" in the sense that they are not invariant with respect to arbitrary rotations around the 6-fold symmetry axis.

A similar pattern of matrix structures holds for $\alpha = 4$, 5, and 6. While $C_{6\beta\gamma}$ has the form described by equation 5.14, the constraints 5.21–5.23 show that $C_{4(\beta\gamma)}$ in equation 5.12 and $C_{5(\beta\gamma)}$ in equation 5.13 can be obtained from each other by permutation of columns and rows:

$$C_{5(\beta\gamma)} = \mathcal{R}_1 C_{4(\beta\gamma)} \mathcal{R}_1 \,, \tag{5.25}$$

where

$$\mathcal{R}_1 = \left(\begin{array}{c|c} P_1 & \mathbf{0} \\ \hline \mathbf{0} & P_1 \end{array} \right) . \tag{5.26}$$

Here, $\mathbf{0}$ is a 3×3 matrix of zeros and P_1 is a permutation matrix that interchanges the first and second columns or rows of any 3×3 matrix:

$$P_1 = \begin{pmatrix} 0 & 1 & 0 \\ 1 & 0 & 0 \\ 0 & 0 & 1 \end{pmatrix} . \tag{5.27}$$

5.4.5 Isotropic TOE

The isotropic TOE tensor is described by three linearly independent elements (e.g., Barsch and Chang, 1968), here chosen to be C_{123}, C_{144} and C_{456} (see Appendix G). The complete $C_{\alpha\beta\gamma}$ matrix for isotropic media can be expressed through just two matrices, $C_{1(\beta\gamma)}$ and $C_{4(\beta\gamma)}$:

$$C_{1(\beta\gamma)} = \begin{pmatrix} C_{111} & C_{112} & C_{112} & 0 & 0 & 0 \\ C_{112} & C_{112} & C_{123} & 0 & 0 & 0 \\ C_{112} & C_{123} & C_{112} & 0 & 0 & 0 \\ 0 & 0 & 0 & C_{144} & 0 & 0 \\ 0 & 0 & 0 & 0 & C_{155} & 0 \\ 0 & 0 & 0 & 0 & 0 & C_{155} \end{pmatrix} \tag{5.28}$$

and

$$C_{4(\beta\gamma)} = \begin{pmatrix} 0 & 0 & 0 & C_{144} & 0 & 0 \\ 0 & 0 & 0 & C_{155} & 0 & 0 \\ 0 & 0 & 0 & C_{155} & 0 & 0 \\ C_{144} & C_{155} & C_{155} & 0 & 0 & 0 \\ 0 & 0 & 0 & 0 & 0 & C_{456} \\ 0 & 0 & 0 & 0 & C_{456} & 0 \end{pmatrix}, \tag{5.29}$$

where (Thurston and Brugger, 1964b)

$$C_{111} = C_{123} + 6C_{144} + 8C_{456}\,, \tag{5.30}$$
$$C_{112} = C_{123} + 2C_{144}\,, \tag{5.31}$$
$$C_{155} = C_{144} + 2C_{456}\,. \tag{5.32}$$

The remaining matrices can be obtained from the following permutations:

$$C_{2(\beta\gamma)} = \mathcal{R}_1 C_{1(\beta\gamma)} \mathcal{R}_1\,, \quad C_{3(\beta\gamma)} = \mathcal{R}_2 C_{1(\beta\gamma)} \mathcal{R}_2\,, \tag{5.33}$$
$$C_{5(\beta\gamma)} = \mathcal{R}_1 C_{4(\beta\gamma)} \mathcal{R}_1\,, \quad C_{6(\beta\gamma)} = \mathcal{R}_2 C_{4(\beta\gamma)} \mathcal{R}_2\,. \tag{5.34}$$

The matrix $\mathcal{R}_2$ has the same block structure as $\mathcal{R}_1$ from equation 5.26, but with P_1 substituted by P_2, a matrix that interchanges the first and third rows or columns of 3×3 matrices:

$$P_2 = \begin{pmatrix} 0 & 0 & 1 \\ 0 & 1 & 0 \\ 1 & 0 & 0 \end{pmatrix}. \tag{5.35}$$

5.5 Symmetry of The Deformed Medium

The matrix representation of the TOE tensor helps to devise an algebraic procedure to evaluate the symmetry of a medium under stress/strain. Using Voigt notation, equation 5.3 can be expressed in terms of the TOE matrix $C_{\alpha\beta\gamma}$:

$$C_{\beta\gamma} = C^{\circ}_{\beta\gamma} + C_{\alpha\beta\gamma}\,\Delta E_{\alpha}\,, \tag{5.36}$$

where the vector $\Delta E_{\alpha} = (e_{11}, e_{22}, e_{33}, 2e_{23}, 2e_{13}, 2e_{12})^{\mathsf{T}}$ is obtained from the symmetric strain tensor Δe_{mn} by applying Voigt notation. Hereafter, the strain tensor with vanishing off-diagonal components ΔE_4, ΔE_5 and ΔE_6 will be called *diagonal*. If the elements ΔE_1, ΔE_2 and ΔE_3 of a diagonal strain tensor are equal, such a tensor represents *volumetric strain change* (Fuck et al., 2008).

Each perturbation stiffness element $\Delta C_{\beta\gamma} = C_{\alpha\beta\gamma}\,\Delta E_{\alpha}$ in equation 5.36 is obtained as a linear combination of the $C_{\alpha(\beta\gamma)}$ matrices scaled by the components of the vector ΔE_{α}. Due to the significant difference in the structure of the matrices $C_{\alpha(\beta\gamma)}$ for $\alpha = 1$, 2, 3 and

$\alpha = 4, 5, 6$, it is possible to separate the contributions of the normal (diagonal) and shear (off-diagonal) strain components in equation 5.36. Next, we analyze the symmetry of the perturbation matrix $\Delta C_{\alpha\beta}$ using the results of the previous section. The structure of the resulting stiffness matrix $C_{\beta\gamma}$ is defined by the stiffnesses of the undeformed medium and the nonzero elements of $\Delta C_{\beta\gamma}$.

5.5.1 Isotropic TOE Tensor

When the TOE tensor is isotropic, the symmetry of the matrix $\Delta C_{\alpha\beta}$ is entirely controlled by the structure of the strain tensor. This can be proved by substituting the matrix representation of the isotropic TOE tensor into equation 5.36.

For a volumetric strain change ($\Delta E_1 = \Delta E_2 = \Delta E_3$; $\Delta E_4 = \Delta E_5 = \Delta E_6 = 0$), the term $C_{\alpha\beta\gamma}\,\Delta E_\alpha$ reduces to the sum of the matrix $C_{1(\beta\gamma)}$ from equation 5.28 and its two permutations, $C_{2(\beta\gamma)}$ and $C_{3(\beta\gamma)}$, multiplied by the normal strain ΔE_1. The resulting tensor $\Delta C_{\alpha\beta}$ is isotropic:

$$\begin{aligned}
&\Delta C_{11} = \Delta C_{22} = \Delta C_{33} = (C_{111} + 2C_{112})\,\Delta E_1\,,\\
&\Delta C_{44} = \Delta C_{55} = \Delta C_{66} = (C_{144} + 2C_{155})\,\Delta E_1\,,\\
&\Delta C_{12} = \Delta C_{13} = \Delta C_{23} = \Delta C_{11} - 2\Delta C_{44} = (C_{123} + 2C_{111})\,\Delta E_1\,.
\end{aligned}$$

This confirms our expectation that any object undergoing volumetric change will remain just a scaled version of itself by conserving its original shape or symmetry.

If the applied strain is uniaxial, then the stiffness perturbation from equation 5.36 is transversely isotropic (TI). For example, the vertical strain ΔE_3 yields the tensor $\Delta C_{\alpha\beta}$ with VTI symmetry:

$$\begin{aligned}
\Delta C_{11} =& \Delta C_{22} = C_{112}\,\Delta E_3\,;\\
\Delta C_{33} =& C_{111}\,\Delta E_3\,;\\
\Delta C_{44} =& \Delta C_{55} = C_{155}\,\Delta E_3\,;\\
\Delta C_{66} =& C_{144}\,\Delta E_3\,;\\
\Delta C_{12} =& \Delta C_{11} - 2\Delta C_{66} = C_{123}\,\Delta E_3\,;\\
\Delta C_{13} =& \Delta C_{23} = C_{112}\,\Delta E_3\,.
\end{aligned}$$

When the strain tensor is diagonal, each matrix $C_{\alpha(\beta\gamma)}$ $(\alpha = 1, 2, 3)$ is multiplied with a different normal strain component, which results in the stiffness perturbation that has orthorhombic symmetry:

$$\Delta C_{\alpha\beta} = \begin{pmatrix}
\Delta C_{11} & \Delta C_{12} & \Delta C_{13} & 0 & 0 & 0\\
\Delta C_{12} & \Delta C_{22} & \Delta C_{23} & 0 & 0 & 0\\
\Delta C_{13} & \Delta C_{23} & \Delta C_{33} & 0 & 0 & 0\\
0 & 0 & 0 & \Delta C_{44} & 0 & 0\\
0 & 0 & 0 & 0 & \Delta C_{55} & 0\\
0 & 0 & 0 & 0 & 0 & \Delta C_{66}
\end{pmatrix}.$$

In fact, if the TOE tensor is isotropic, the symmetry of $\Delta C_{\alpha\beta}$ is always orthorhombic or higher, with the principal directions of the strain tensor defining the 2-fold symmetry axes of the deformed medium. For example, a nonzero component ΔE_6 causes a rotation of the principal directions of the strain tensor around the x_3-axis of the Cartesian coordinate system. In addition to $C_{1(\beta\gamma)}$, $C_{2(\beta\gamma)}$ and $C_{3(\beta\gamma)}$, the stiffness perturbation for $\Delta E_6 \neq 0$ also depends on the matrix $C_{6(\beta\gamma)}$ (equation 5.36):

$$\Delta C_{\alpha\beta} = \begin{pmatrix} \Delta C_{11} & \Delta C_{12} & \Delta C_{13} & 0 & 0 & \Delta C_{16} \\ \Delta C_{12} & \Delta C_{22} & \Delta C_{23} & 0 & 0 & \Delta C_{26} \\ \Delta C_{11} & \Delta C_{12} & \Delta C_{13} & 0 & 0 & \Delta C_{36} \\ 0 & 0 & 0 & \Delta C_{44} & \Delta C_{45} & 0 \\ 0 & 0 & 0 & \Delta C_{45} & \Delta C_{55} & 0 \\ \Delta C_{16} & \Delta C_{26} & \Delta C_{36} & 0 & 0 & \Delta C_{66} \end{pmatrix}. \tag{5.37}$$

The matrix $\Delta C_{\alpha\beta}$ in equation 5.37 describes an orthorhombic medium rotated around the x_3-axis because ΔC_{16}, ΔC_{26}, ΔC_{36} and ΔC_{45} are not independent. For instance, the element ΔE_6 in the coordinate system rotated by the angle θ around the x_3-axis is given by

$$\Delta E_6 = 2\Delta e_{12} = 2(\Delta E'_2 - \Delta E'_1)\sin\theta\cos\theta\,, \tag{5.38}$$

where $\Delta E'_1$ and $\Delta E'_2$ denote the components of the strain tensor in the unrotated coordinate system. Using equation 5.38, we find that

$$\Delta C_{36} = \left(\Delta C'_{23} - \Delta C'_{13}\right)\sin\theta\cos\theta\,, \tag{5.39}$$

where, $\Delta C'_{ij}$ are the components of the stiffness perturbation tensor in the unrotated coordinate system. Thus, the orientation of the vertical symmetry planes of the orthorhombic medium described by the matrix $\Delta C_{\alpha\beta}$ is determined by the element ΔE_6.

A numerical example of the stiffness perturbation $\Delta C_{\alpha\beta}$ that has orthorhombic symmetry resulting from the combination of a purely isotropic TOE tensor and an arbitrary (non-diagonal) strain tensor is given by Fuck et al. (2009). In their model, a pore-pressure drop inside a rectangular reservoir embedded in a homogeneous isotropic host rock induce stress/strain changes throughout the medium (Figure 5.1). The spatially varying stiffness perturbations caused by the excess stress/strain field are computed from equation 5.36. As illustrated by Figure 5.2, the compaction-related strain makes the reservoir and the surrounding medium both heterogeneous and anisotropic. In the vertical symmetry plane $[x_1, x_3]$ shown in Figures 5.1 and 5.2, the perturbation matrix $\Delta C_{\alpha\beta}$ corresponds to a transversely isotropic medium with elliptical P-wave anisotropy (i.e., the Thomsen parameters ε and δ are equal; Figure 5.2a). The accumulation of shear stress/strain near the corners of the reservoir causes a significant tilt of the symmetry axis from the vertical (Figure 5.2b).

5.5.2 Hexagonal TOE Tensor

If the 6-fold symmetry axis is parallel to the x_3-direction, the matrix $C_{3(\beta\gamma)}$ of the hexagonal TOE tensor has VTI symmetry, whereas $C_{1(\beta\gamma)}$ and $C_2(\beta\gamma)$ are orthorhombic

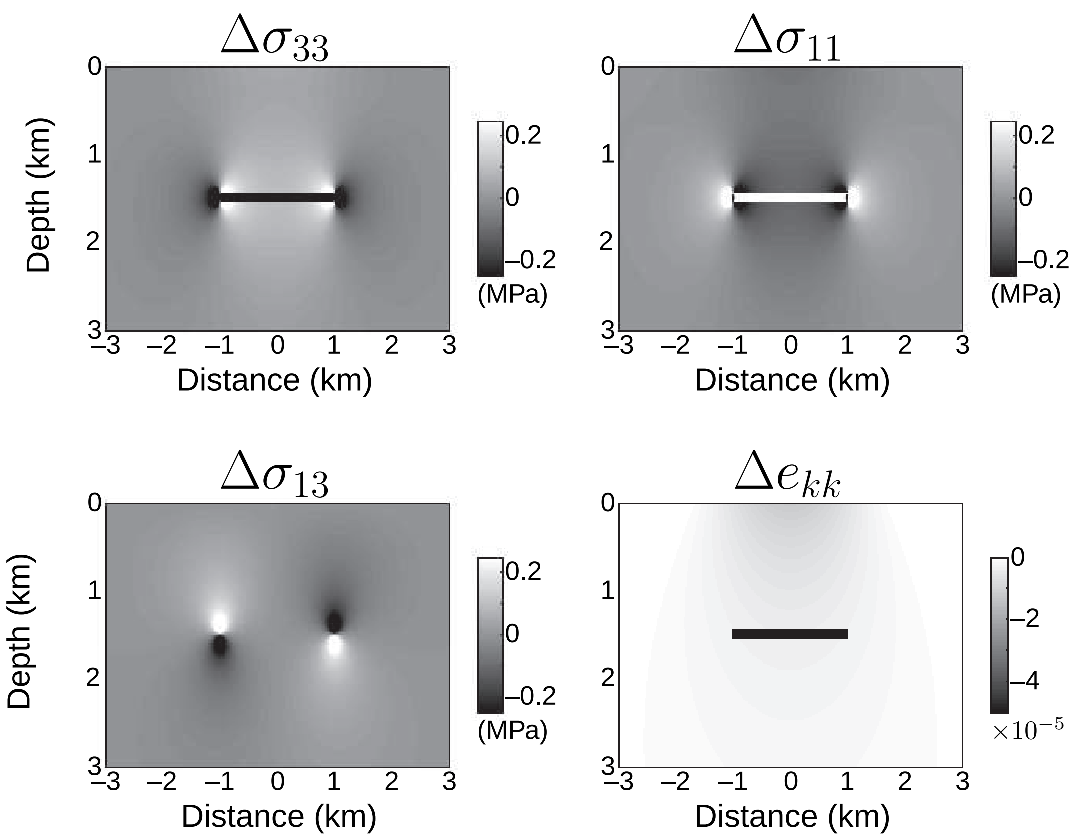

Figure 5.1. 2D stress and strain changes due to a 5 MPa drop in pore pressure (i.e., due to compaction) inside a rectangular reservoir (after Fuck et al., 2008). $\Delta\sigma_{33}$ and $\Delta\sigma_{11}$ are the normal deviatoric stresses, $\Delta\sigma_{13}$ is the shear deviatoric stress, and Δe_{kk} is the trace of the strain tensor. Negative values imply compression for stress and contraction (shortening) for strain. Inside the reservoir the maximum stresses are $\Delta\sigma_{33} = -2.2$ MPa and $\Delta\sigma_{11}$=1.7 MPa, while the volumetric change is constant: $\Delta e_{kk} = -4.6 \times 10^{-4}$. The plots were clipped for better visualization.

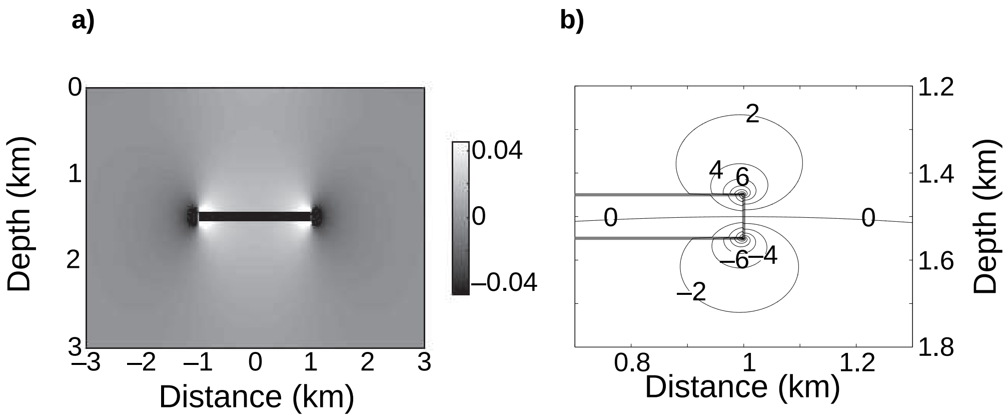

Figure 5.2. Anisotropy parameters and the symmetry-axis orientation of the strain-induced TI medium for the reservoir model from Figure 5.1 (after Fuck et al., 2008). a) The anisotropy parameter $\delta = \epsilon$ (color scale is clipped); b) contours of the angle between the symmetry axis and the vertical (positive angles correspond to clockwise axis rotation) near the right edge of the reservoir (solid gray rectangle). Inside the reservoir $\delta = -0.18$, while the tilt of the symmetry axis at the reservoir corners approaches $\pm 45°$.

(equations 5.11 and 5.24). Therefore, a uniaxial strain applied in the symmetry-axis direction (i.e., $\Delta E_3 \neq 0$) yields the stiffness perturbation with VTI symmetry. If a uniaxial strain is parallel to the x_1- or x_2-axis, the stiffness perturbation inherits the orthorhombic symmetry of either the $C_{1(\beta\gamma)}$ or the $C_{2(\beta\gamma)}$ matrix. Furthermore, any diagonal strain tensor also produces $\Delta C_{\alpha\beta}$ with orthorhombic symmetry.

Volumetric strain ($\Delta E_1 = \Delta E_2 = \Delta E_3$) leads to VTI symmetry of the matrix $\Delta C_{\alpha\beta}$, because the sum of the matrices $C_{1(\beta\gamma)}$, $C_{2(\beta\gamma)}$ and $C_{3(\beta\gamma)}$ gives the well-known VTI relationships:

$$\Delta C_{11} = \Delta C_{22} = (2C_{111} - C_{166} - 3C_{266} + C_{113})\,\Delta E_1\,, \tag{5.40}$$

$$\Delta C_{12} = \Delta C_{11} - 2\Delta C_{66} = (C_{112} + C_{122} + C_{123})\,\Delta E_1\,, \tag{5.41}$$

$$\Delta C_{13} = \Delta C_{23} = (C_{113} + C_{123} + C_{133})\,\Delta E_1\,, \tag{5.42}$$

$$\Delta C_{44} = \Delta C_{55} = (C_{144} + C_{155} + C_{344})\,\Delta E_1\,. \tag{5.43}$$

If the only non-vanishing shear strain is $\Delta E_6 = 2\Delta e_{12}$, the matrix $\Delta C_{\alpha\beta}$ still has orthorhombic symmetry, but its vertical symmetry planes are rotated with respect to the axes x_1 and x_2. This can be verified by showing that the elements ΔC_{45} and ΔC_{i6} $(i = 1, 2, 3)$ are not linearly independent (e.g., equation 5.39 remains valid). The presence of nonzero shear strains defined in planes that are not perpendicular to the 6-fold symmetry axis of the TOE tensor lowers the symmetry of the stiffness perturbation. For instance, when $\Delta E_5 \neq 0$ ($\Delta E_4 = \Delta E_6 = 0$), ΔC_{46} no longer represents a linear combination of ΔC_{66} and ΔC_{44}

because

$$\Delta C_{46} \neq (\Delta C_{66} - \Delta C_{44}) \sin\theta \cos\theta \,.$$

Then the symmetry of $\Delta C_{\alpha\beta}$ becomes monoclinic with the $[x_1, x_3]$ symmetry plane. Similarly, if ΔE_4 is the only nonzero strain element, the perturbation stiffness tensor is also monoclinic, but the symmetry plane is $[x_2, x_3]$. If both ΔE_4 and ΔE_5 are nonzero, the perturbation $\Delta C_{\alpha\beta}$ has triclinic symmetry.

5.5.3 Lower TOE Symmetries

The summation in equation 5.36 produces the stiffness perturbation that cannot have a higher symmetry than that of the TOE tensor. When the TOE tensor is orthorhombic or monoclinic, the symmetry of $\Delta C_{\alpha\beta}$ depends on the structure of the strain tensor only if the shear strains are nonzero. The combination of diagonal strain and the TOE tensor with orthorhombic or monoclinic symmetry always generates an orthorhombic or monoclinic stiffness perturbation $\Delta C_{\alpha\beta}$, respectively.

When the TOE tensor is orthorhombic, a single nonzero shear strain component produces the perturbation $\Delta C_{\alpha\beta}$ with monoclinic symmetry (equations 5.12–5.14). If two or three shear strains are nonzero, the resulting perturbation tensor is triclinic. Likewise, for a monoclinic TOE tensor, any shear strain not defined in the symmetry plane (i.e., in the plane perpendicular to the 2-fold symmetry axis) produces a triclinic perturbation $\Delta C_{\alpha\beta}$. Therefore, misalignment of the principal strain directions with the symmetry elements of the TOE tensor lowers the symmetry of $\Delta C_{\alpha\beta}$.

Finally, if the TOE tensor is triclinic, the stiffness perturbation always has triclinic symmetry as well, regardless of the structure of the strain tensor.

5.5.4 Symmetry of The Resulting Stiffness Tensor

The above discussion was focused on the symmetry of the perturbation stiffness matrix $\Delta C_{\beta\gamma} = C_{\alpha\beta\gamma}\, \Delta E_\alpha$ in equation 5.36. Once this matrix has been obtained, it is straightforward to evaluate the symmetry of the effective elastic tensor $C_{\alpha\beta}$ which describes the medium after deformation. In principle, the symmetry of the strained medium should not be higher than that of either $C^\circ_{\alpha\beta}$ or $\Delta C_{\alpha\beta}$. There might be situations, however, in which some of the off-diagonal terms in $C^\circ_{\alpha\beta}$ and $\Delta C_{\alpha\beta}$ cancel out, resulting in the deformed medium with a higher symmetry than those of the background model and the stiffness perturbation. Although this issue should be studied further, such strain-induced compensation of intrinsic anisotropy seems unlikely.

5.6 Conclusions

Excess stresses and strains generated by reservoir compaction and other physical processes in the subsurface cause velocity anisotropy that can be evaluated using seismic methods. Here, we used the theory of nonlinear elasticity based on third-order elastic (TOE) tensors to analyze the symmetry of a medium under stress/strain. Employing Voigt notation, we introduced a convenient representation of the TOE tensor c_{ijklmn} in terms of a $6 \times 6 \times 6$ matrix $C_{\alpha\beta\gamma}$. The strain-induced stiffness perturbation $\Delta C_{\beta\gamma}$ is then obtained by summing 6×6 TOE submatrices scaled by the components of the strain tensor. This formalism provides a direct way to assess the contribution of each strain component to the stiffness perturbation for a given symmetry of the TOE tensor. In particular, our approach helps to separate the influence of the normal and shear strains on the symmetry of the perturbed medium.

In the simplest case of a purely isotropic TOE tensor, the perturbation $\Delta C_{\beta\gamma}$ always has orthorhombic or higher symmetry with the the 2-fold symmetry axes defined by the principal directions of the strain tensor. When the strain is uniaxial, the stiffness perturbation is transversely isotropic, and the symmetry axis is parallel to the strain direction. The deformed medium remains isotropic only if an isotropic TOE tensor is combined with volumetric strain (i.e., the strain tensor has only identical diagonal elements).

When the TOE tensor is hexagonal (transversely isotropic), a uniaxial strain applied in the direction of the symmetry axis results in TI symmetry. However, if the strain tensor is diagonal or a uniaxial strain is confined to the plane orthogonal to the symmetry axis, the stiffness perturbation becomes orthorhombic. The influence of the off-diagonal (shear) strains may lower the symmetry of $\Delta C_{\beta\gamma}$ to monoclinic or even triclinic.

On the whole, our algebraic procedure significantly facilitates application of TOE tensors to analysis of strain-induced velocity perturbations. The formalism introduced here is as intuitive as that describing the strain sensitivity of seismic velocities through closing or opening of microcracks. Our results should be helpful in modeling and inversion of strain-induced anisotropic velocity fields near compacting hydrocarbon reservoirs and salt bodies.

5.7 Acknowledgments

We are grateful to our colleagues in the Center for Wave Phenomena (CWP) at Colorado School of Mines (CSM) for helpful discussions. This work was supported by the Consortium Project on Seismic Inverse Methods for Complex Structures at CWP.

Chapter 6

Conclusions and Future Work

In this thesis I investigated seismic signatures of effective anisotropic elastic media that can be used in static and dynamic reservoir characterization. The analysis included both fracture- and stress-induced anisotropy.

Chapter 2 is devoted to seismic signatures of an effective medium formed by two sets of vertical, orthogonal fractures with microcorrugated surfaces embedded in isotropic host rock. Using the weak-anisotropy approximation, I derived closed-form expressions for the shear-wave splitting, NMO ellipses of horizontal reflection events and P-wave reflection coefficient. These expressions provide valuable insight into the behavior of seismic signatures as a function of fracture rheology. The fracture weaknesses, for instance, control the orientation and eccentricity of the NMO ellipses of the reflected P-, S_1-, and S_2-waves. In particular, the contributions of the off-diagonal weaknesses Δ_{NH_i} and Δ_{VH_i} $(i = 1, 2)$, which are related to corrugation, lead to the rotation of the NMO ellipses with respect to the fracture strike directions. In contrast to the effective orthorhombic medium formed by two orthogonal sets of penny-shaped cracks, all three NMO ellipses in this model have different orientations.

Due to the lack of experimental data about the off-diagonal fracture weaknesses in reservoir rocks, an interesting future direction is to use the analytic equations from Chapter 2 to implement inversion for certain combinations of the weaknesses. For example, if the vertical velocities are available from check-shots, one can invert for the V_P/V_S ratio and the differences between the diagonal weaknesses Δ_{N_i}, Δ_{V_i} and Δ_{H_i} of the two sets. In addition, the sum of the off-diagonal weaknesses Δ_{NH_i} can be estimated from the P-wave NMO ellipse and AVO gradient. Constraining the weaknesses Δ_{VH_i} and Δ_{NV_i}, however, is more difficult, because they only appear in relatively small terms. For a single microcorrugated fracture set, both Δ_{VH} and Δ_{NV} can be determined from VSP data using the slowness surface of P-waves. It is not clear, however, if such an algorithm can be extended to more complicated models.

An analytic description of compaction-related traveltime shifts was given in Chapter 3. It was based on three assumptions: i) first-order traveltime perturbations provide good approximation for the traveltime shifts; ii) depletion-induced velocity perturbations can be described by a purely isotropic strain-sensitivity tensor; iii) reservoir compaction can be explained by elastic deformation. The first assumption helps to obtain an approximation that accurately describes ray-traced traveltime shifts, unless the velocity perturbations are large. The second assumption limits the stress-induced anisotropy to the special case of a tilted orthorhombic medium in 3D (equivalent to tilted TI in 2D), but it reduces the number of the independent third-order stiffnesses to three. The assumption of elastic deformation facilitates modeling of compaction, subsidence and strain caused by pore-pressure changes inside a reservoir.

The main result of Chapter 3 is equation 3.17, which generalizes existing expressions for zero-offset shifts and those for offset-dependent traveltime shifts in isotropic media. This equation helps to explain the behavior of compaction-related traveltime shifts in common-midpoint (CMP) and shot gathers. The two first-order components of traveltime shifts are related to the geometric and velocity changes. Analysis of equation 3.17 indicates that for elastic deformation the geometric component typically is at least an order of magnitude smaller than the contribution of the velocity perturbations. Traveltime shifts due to the velocity changes could be further split into two terms, one of which is related to the volumetric changes and the other to the deviatoric stresses. Significant volumetric changes are largely restricted to the reservoir and to the vicinity of the earth's surface. The deviatoric stress term, which is related to changes in the nonhydrostatic stress, controls the velocity anisotropy of the deformed elastic medium.

Although the numerical results in Chapter 3 were obtained for a simple 2D model, they illustrate the essential properties of stress-induced variations in reflection traveltimes. In particular, traveltime shifts for reflectors at and above the reservoir are associated primarily with the stress-induced anisotropy. Hence, adding an extra dimension (offset) to time-lapse analysis should help to better constrain the geomechanical changes around depleting blocks and improve interpretation of 4D seismic data.

Chapter 4 is focused on the influence of heterogeneity of the background velocity model on traveltime shifts and their variation with offset. In particular, the contrast in the rigidity modulus μ across the reservoir boundaries changes the compaction-induced strain and modifies the relative contributions of the isotropic and anisotropic velocity perturbations. Nevertheless, traveltime shifts are mainly governed by the anisotropic velocity perturbations since the most significant isotropic velocity changes are largely restricted to the reservoir itself. Thus, traveltime shifts should be studied in the prestack domain, since analysis of stacked data is not sufficient for reconstruction of compaction-induced velocity perturbations. In essence, the numerical experiments show that the larger the deviatoric strains produced by reservoir compaction, the larger the offset variation of traveltime shifts. The results for the Valhall-style layered model, in which deeper formations are stiffer and less sensitive to stress, suggest that both traveltime shifts and their variation with offset are largest for reflections from interfaces above the reservoir, recorded at CMP locations near the reservoir edge.

There are several promising directions of future research on traveltime shifts. First, the theory developed in Chapters 3 and 4 should be applied to analysis of field 4D datasets acquired over compacting reservoirs. Measurements of traveltime shifts on prestack seismic data present a number of challenges, such as noise in time-lapse signatures caused by non-repeatability. For example, it is necessary to account for the relative movement of sources and receivers due to sea tides between time-lapse marine surveys. Another important issue is to evaluate the impact of stacking on traveltime shifts because time-lapse analysis of partial stacks of near-, mid- and far-offsets is more stable than that on raw prestack data.

Future work should also consider implementation of tomographic inversion to map the stress-induced velocity field. It would be useful to derive similar equations describing traveltime shifts for shear-wave data (both pure and converted modes), which could provide valuable constraints on the stress distribution. Additional information for time-lapse analysis can be obtained from body-wave reflection coefficients, which provide a more localized estimate of the stress-induced velocity perturbations caused by reservoir depletion.

Two other issues worth investigating are the influence of anelastic deformation inside the compacting reservoir and the impact of treating deformation as a time-dependent variable. Addressing these problems should help to improve the description of traveltime shifts below compacting reservoirs and make it possible to carry out time-lapse analysis over longer time periods.

In Chapters 3 and 4, velocity perturbations in and around a compacting reservoir were modeled using the strain-sensitivity tensors from nonlinear elasticity theory. In Chapter 5, I introduced a new matrix representation of these third-order elastic (TOE) tensors that not only simplifies computation of the velocity perturbations, but also leads to a simple algebraic procedure to evaluate the symmetry of the stressed medium. Using Voigt notation, the TOE tensor c_{ijklmn} was represented by a $6 \times 6 \times 6$ matrix which allowed the stress-induced perturbation to be obtained by summing 6×6 matrices scaled by the components of the strain tensor. This matrix notation provides a direct way to account for the symmetry of TOE tensors and to separate the influence of the normal and shear strains on the symmetry of the perturbed medium.

Development of analytic expressions for traveltime shifts or other types of seismic signatures for a more complicated anisotropic background should benefit from the matrix representation proposed in Chapter 5. For example, this formalism predicts that for VTI background velocity models and a purely isotropic TOE tensor, the perturbed velocity field will have orthorhombic symmetry above and below the reservoir, but close to the reservoir edges the symmetry is monoclinic.

References

Bakulin, A., V. Grechka, and I. Tsvankin, 2000a, Estimation of fracture parameters from reflection seismic data - Part I: HTI model due to a single fracture set: Geophysics, **65**, 1788–1802.

——— 2000b, Estimation of fracture paramenters from reflection seismic data - Part II: Fractured models with orthorhombic symmetry: Geophysics, **65**, 1803–1817.

——— 2000c, Estimation of fracture paramenters from reflection seismic data - Part III: Fractured models with monoclinic symmetry: Geophysics, **65**, 1818–1830.

Barsch, G. R., and Z. Chang, 1968, Second- and higher-order effective elastic constants of cubic crystals under hydrostatic pressure: Journal of Applied Physics, **39**, 3276–3284.

Brugger, K., 1964, Thermodynamic definition of higher order elastic coefficients: Physical Review, **113**, A1611–A1612.

Cardona, R., 2002, Fluid substitution theories and multicomponent seismic characterization of fractured reservoirs: PhD thesis, Colorado School of Mines.

Červený, V., 2001, Seismic ray theory: Cambridge University Press.

Chapman, C., 2004, Fundamentals of seismic wave propagation: Cambridge University Press, 1st edition.

Chapman, C. H., and R. G. Pratt, 1992, Traveltime tomography in anisotropic media — I. Theory: Geophysical Journal International, **109**, 1–19.

Chin, L. Y., and N. B. Nagel, 2004, Modeling of subsidence and reservoir compaction under waterflood operations: International Journal of Geomechanics, **4**, 28–34.

DeVault, B., T. L. Davis, I. Tsvankin, R. Verm, and F. Hilterman, 2002, Multicomponent AVO analysis, Vacuum field, New Mexico: Geophysics, **67**, 701–710.

Downes, J. R., D. A. Faux, and E. P. O'Reilly, 1997, A simple method for calculating strain distributions in quantum dot structures: Journal of Applied Physics, **81**, 6700–6702.

Eberhart-Phillips, D., D.-H. Han, and M. D. Zoback, 1989, Empirical relations among seismic velocity, effective pressure, porosity and clay content in sandstone: Geophysics, **54**, 82–89.

Farra, V., 2001, High-order perturbations of the phase velocity and polarization of qP and qS waves in anisotropic media: Geophysical Journal International, **147**, 93–104.

Farra, V., and S. Le Bégat, 1995, Sensitivity of qP-wave traveltime and polarization vectors to heterogeneity, anisotropy and interfaces: Geophysical Journal International, **121**, 371–384.

Faux, D. A., J. R. Downes, and E. P. O'Reilly, 1997, Analytic solutions for strains distributions in quantum-wire structures: Journal of Applied Physics, **82**, 3754–3762.

Fuck, R. F., A. Bakulin, and I. Tsvankin, 2009, Theory of traveltime shifts around compacting reservoirs: 3D solutions for heterogeneous anisotropic media: Geophysics, **74**, D25–D36.

Fuck, R. F., and I. Tsvankin, 2006, Seismic signatures of two orthogonal sets of vertical microcorrugated fractures: Journal of Seismic Exploration, **15**, 183–208.

——— 2009, Analysis of the symmetry of a stressed medium using nonlinear elasticity: submitted to Geophysics, 24pp.

Fumi, F. G., 1951, Third-orer elastic coefficients of crystals: Physical Review, **83**, 1274–1275.

——— 1952, Third-order elastic coefficients in trigonal and hexagonal crystals: Physical Review, **86**, 561.

Geertsma, J., 1973, Land subsidence above compacting oil and gas reservoirs: Journal of Petroleum Technology, **25**, 734–744.

Glas, F., 1991, Coherent stress relaxation in half space: modulated layers, inclusions, steps, and a general solution: Journal of Applied Physics, **70**, 3556–3571.

Goldstein, H., 1980, Classical mechanics: Addison-Wesley, 2nd ed. edition.

Grechka, V., A. Bakulin, and I. Tsvankin, 2003, Seismic characterization of vertical fractures described as general linear-slip interfaces: Geophysical Prospecting, **51**, 117–129.

Grechka, V., P. Contreras, and I. Tsvankin, 2000, Inversion of normal moveout for monoclinic media: Geophysical Prospecting, **48**, 577–602.

Grechka, V., and I. Tsvankin, 2003, Feasibility of seismic characterization of multiple sets: Geophysics, **68**, 1399–1407.

Grechka, V., I. Tsvankin, and J. K. Cohen, 1999, Generalized Dix equation and analytic treatment of normal-moveout velocity for anisotropic media: Geophysical Prospecting, **47**, 117–148.

Guilbot, J., and B. Smith, 2002, 4D constrained depth conversion for reservoir compaction estimation: Application to Ekofisk field: The Leading Edge, **21**, 302–308.

Gurevich, B., 2003, Elastic properties of saturated porous rocks with aligned fractures: Journal of Applied Geophysics, **54**, 203–218.

Gutierrez, M. S., and R. W. Lewis, 2002, Coupling of fluid flow and deformation in underground formations: Journal of Engineering Mechanics, **128**, 779–787.

Hatchell, D. P. J., and S. J. Bourne, 2005a, Measuring reservoir compaction using time-lapse timeshifts: Annual International Meeting, Expanded Abstracts, 2500–2503.

Hatchell, P., and S. Bourne, 2005b, Rocks under strain: strain-induced time-lapse timeshifts are observed for depleting reservoirs: The Leading Edge, **24**, 1222–1225.

Hearmon, R. F. S., 1953, Third-order elastic coefficients: Acta Crystallographica, **6**, 331–340.

Helbig, K., 1994, Foundations of anisotropy for exploration seismics: Pergamon.

Herwanger, J., and S. Horne, 2005, Predicting time-lapse stress effects in seismic data: The Leading Edge, **24**, 1234–1242.

Herwanger, J., E. Palmer, and C. R. Schiøtt, 2007, Anisotropic velocity changes in seismic time-lapse data: 77th Annual International Meeting, SEG, Expanded Abstracts, 2883–2887.

Hodgson, N., C. MacBeth, L. Duranti, J. Rickett, and K. Nihei, 2007, Inverting for reservoir pressure change using time-lapse time strain: application to Genesis field, Gulf of Mexico: The Leading Edge, **26**, 649–652.

Hood, J. A., 1991, A simple method for decomposing fracture-induced anisotropy: Geophysics, **56**, 1275–1279.

Hu, S. M., 1989, Stress from a parallelepipedic thermal inclusion in a semispace: Journal of Applied Physics, **66**, 2741–2743.

Jech, J., and I. Pšenčik, 1989, First-order perturbation method for anisotropic media: Geophysical Journal International, **99**, 369–376.

Johnson, P. A., and P. N. J. Rasolofosaon, 1996, Nonlinear elasticity and stress-induced anisotropy in rock: Journal of Geophysical Research, **101**, 3113–3124.

Kachanov, M., and I. Sevostianov, 2005, On quantitative characterization of microstructures and effective properties: International Journal of Solids and Structures, **42**, 309–336.

Lanczos, C., 1986, Variational principles of mechanics: Dover Publications Inc., 4th edition.

Landrø, M., and J. Stammeijer, 2004, Quantitative estimation of compaction and velocity changes using 4D impedance and traveltime changes: Geophysics, **69**, 949–957.

Lynn, H., K. M. Simon, M. Layman, R. Schneider, C. R. Bates, and M. Jones, 1995, Use of anisotropy in P-wave and S-wave data for fracture characterization in a naturally fractured gas reservoir: The Leading Edge, **14**, 887–893.

Mallick, S., K. L. Craft, L. J. Meister, and R. E. Chambers, 1998, Determination of the principal directions of azimuthal anisotropy from P-wave seismic data: Geophysics, **63**, 692–706.

Mavko, G., T. Mukerji, and J. Dvorkin, 1998, The rock physics handbook, tools for seismic analysis in poroous media: Cambridge University Press, 1st edition.

Mavko, G., T. Mukerji, and N. Godfrey, 1995, Predicting stress-induced velocity anisotropy in rocks: Geophysics, **60**, 1081–1087.

Nakagawa, S., K. T. Nihei, and L. R. Myer, 2000, Shear-induced conversion of seismic waves across single fractures: International Journal of Rock Mechanics and Mining Sciences, **37**, 203–218.

Pérez, M. A., V. Grechka, and R. J. Michelena, 1999, Fracture detection in a carbonate reservoir using a variety of seismic methods: Geophysics, **64**, 1266–1276.

Prasad, M., and M. H. Manghnani, 1997, Effects of pore and differential pressure on compressional wave velocity and quality factor in berea and michigan sandstones: Geophysics, **62**, 1163–1176.

Press, W. H., S. A. Teukolsky, W. T. Vellerling, and B. P. Flannery, 1992, Numerical recipes in c—the art of scientific computing: Cambridge University Press, 2nd edition edition.

Prioul, R., A. Bakulin, and V. Bakulin, 2004, Nonlinear rock physics model for estimation of 3d subsurface stress in anisotropic formations: theory and laboratory verification: Geophysics, **69**, 415–425.

Pšenčik, I., and V. Vavryčuk, 2002, Approximate relation between the ray vector and the wave normal in weakly anisotropic media: Studia Geophysica et Geodaetica, **46**, 793–807.

Røste, T., 2007, Monitoring overbudern and reservoir changes from prestack time-lapse seismic data — applications to chalk fields: PhD thesis, NTNU.

Røste, T., A. Stovas, and M. Landrø, 2006, Estimation of layer thickness and velocity changes using 4D prestack seismic data: Geophysics, **71**, S219–S234.

Sarkar, D., A. Bakulin, and R. L. Kranz, 2003, Anisotropic inversion of seismic data for stressed media: theory and a physical modeling study on Berea sandstone: Geophysics, **68**, 690–704.

Sayers, C. M., 2006, Sensitivity of time-lapse seismic to reservoir stress path: Geophysical Prospecting, **54**, 369–380.

Sayers, C. M., and M. Kachanov, 1995, Microcrack-induced elastic wave anisotropy: Journal of Geophysical Research, **100**, 4149–4156.

Schoenberg, M., 1980, Elastic wave behavior across linear slip interfaces: Journal of the Acoustical Society of America, **68**, 1516–1521.

Schoenberg, M., and J. Douma, 1988, Elastic wave propagation in media with parallel fractures and aligned cracks: Geophysical Prospecting, **36**, 571–590.

Schoenberg, M., and F. Muir, 1989, A calculus for finely layered anisotropic media: Geophysics, **54**, 581–589.

Schoenberg, M., and C. M. Sayers, 1995, Seismic anisotropy of fractured rock: Geophysics, **60**, 204–211.

Segall, P., 1992, Induced stresses due to fluid extraction from axisymmetric reservoirs: Pure and Applied Geophysics, **139**, 535–560.

Segall, P., J.-R. Grasso, and A. Mossop, 1994, Poroelastic stressing and induced seismicity near the lacq gas field, southwestern France: Journal of Geophysical Research, **99**, 15,423–15,438.

Sengupta, M., and R. Bachrach, 2008, Velocity updating around salt bodies using stress modeling solutions and non-linear elasticity: 78th Annual International Meeting, SEG, Expanded Abstracts, 3048–3051.

Shapiro, S. A., and A. Kaselow, 2005, Porosity and elastic anisotropy of rocks under tectonic stress and pore-pressure changes: Geophysics, **70**, N27–N38.

Sinha, B. K., and S. Kostek, 1996, Stress-induced azimuthal anisotropy in borehole flexural waves: Geophysics, **61**, 1899–1907.

Sinha, B. K., and T. J. Plona, 2001, Wave propagation in rocks with elastic-plastic deformations: Geophysics, **66**, 772–785.

Soltanzadeh, H., C. D. Hawkes, and J. S. Sharma, 2007, Poroelastic model for production- and injection-induced stresses in reservoirs with elastic properties different from the surrounding rock: International Journal of Geomechanics, **7**, 353–361.

Thomsen, L., 1988, Reflection seismology over azimuthally anisotropic media: Geophysics, **53**, 304–313.

Thurston, R. N., and K. Brugger, 1964a, Third-order elastic constants and the velocity of small amplitude elastic waves in homogeneously stressed media: Physical Review, **133**, A1604 – A1610.

——— 1964b, Third-order elastic constants and the velocity of small amplitude elastic waves in homogeneously stressed media: Physical Review, **133**, A1604–A1610.

Toupin, R. A., and B. Bernstein, 1961, Sound waves in deformed perfectly elastic materials. acoustoelastic effect: Journal of the Acoustical Society of America, **33**, 216–225.

Tsvankin, I., 2001, Seismic signatures and analysis of reflection data in anisotropic media: Elsevier Science, Inc.

Vavryčuk, V., and I. Pšenčik, 1998, PP-wave reflection coefficients in weakly anisotropic elastic media: Geophysics, **63**, 2129–2141.

Wang, H. F., 2000, Theory of linear poroelasticity with applications to geomechanics and hydrogeology: Princeton University Press.

Winkler, K. W., B. K. Sinha, and T. J. Plona, 1998, Effects of borehole stress concentrations on dipole anisotropy measurements: Geophysics, **63**, 11–17.

Winterstein, D. F., 1990, Velocity anisotropy terminology for geophysicists: geop, **55**, 1070–1088.

Yale, D. P., and W. H. Jamieson, Jr., 1994, Static and dynamic mechanical properties of carbonates, *in* Nelson, P. P., and S. E. Laubach, eds., Rock Mechanics Models and Measurements challenges from Industry. Proceedings of the 1st North American Rock Mechanics Symposium, 463–471. Balkema.

Appendix A

Elements of the linear-slip theory

The linear-slip theory (Schoenberg, 1980; Schoenberg and Sayers, 1995) is designed to find an equivalent (long-wavelength) representation of a medium that contains one or several fracture sets. Fractures are treated as planar and parallel surfaces of weakness, and it is assumed that interaction between fractures can be ignored. The fracture length is taken to be infinite, while fracture apertures have to be small compared to the dominant seismic wavelength. According to the linear-slip theory, the jumps in the displacement vector $[u_i]$ (i.e., "slips") across a fracture are to the first order proportional to the (continuous) stresses σ_{jk}:

$$[u_i] = h\, K_{ij}\, \sigma_{jk}\, n_k, \tag{A.1}$$

where $\mathbf{n}$ is the normal to the fracture plane, h is the average spacing between fractures, and K_{ij} are called the "compliances" of the fracture set.

The effective compliance tensor $\mathbf{s}$ of a fractured medium is then found as the sum of the background compliance $\mathbf{s}_b$ and the excess compliances $\mathbf{s}_{f_i}$ of all fracture sets (e.g., Schoenberg and Muir, 1989; Hood, 1991):

$$\mathbf{s} = \mathbf{s}_b + \sum_{i=1}^{N} \mathbf{s}_{f_i}. \tag{A.2}$$

The compliances K_{ij} of each fracture set are mapped onto the corresponding compliance tensor s_{ijkl} using Hooke's law (Sayers and Kachanov, 1995):

$$s_{ijkl} = \frac{1}{4}\left(K_{ik}n_l n_j + K_{jk}n_i n_l + K_{il}n_j n_k + K_{jl}n_i n_k\right). \tag{A.3}$$

Equation A.1 indicates that $\mathbf{K}$ is a 3×3 matrix that has to be symmetric and nonnegative definite because of the symmetries of the compliance tensor. Hence, a fracture system can be described by up to six independent compliance elements. The diagonal terms of the matrix relate the jumps in the normal displacement ("normal slips") to the normal tractions acting across the surface of the fractures, as well as the tangential slips to the shear stresses. The off-diagonal elements are responsible for the coupling of the normal slips and shear stresses and vice-versa. Hereafter, we follow the notation of Grechka et al. (2003):

$$K_{11} \to K_N; \qquad K_{22} \to K_H; \qquad K_{33} \to K_V;$$
$$K_{12} \to K_{NH}; \qquad K_{13} \to K_{NV}; \qquad K_{23} \to K_{VH}.$$

We consider two vertical, orthogonal fracture sets oriented in such a way that that the x_1-axis is perpendicular to the first set. The summation in equation A.2 is more conveniently carried out using the condensed Voigt notation, which allows the compliance tensor to be replaced by a 6×6 compliance matrix. Then, according to equation A.3, the compliances matrices for the two sets take the form

$$s_{f1} = \begin{pmatrix} K_{N_1} & 0 & 0 & 0 & K_{NV_1} & K_{NH_1} \\ 0 & 0 & 0 & 0 & 0 & 0 \\ 0 & 0 & 0 & 0 & 0 & 0 \\ 0 & 0 & 0 & 0 & 0 & 0 \\ K_{NV_1} & 0 & 0 & 0 & K_{V_1} & K_{VH_1} \\ K_{NH_1} & 0 & 0 & 0 & K_{VH_1} & K_{H_1} \end{pmatrix}, \tag{A.4}$$

$$s_{f2} = \begin{pmatrix} 0 & 0 & 0 & 0 & 0 & 0 \\ 0 & K_{N_2} & 0 & K_{NV_2} & 0 & K_{NH_2} \\ 0 & 0 & 0 & 0 & 0 & 0 \\ 0 & K_{NV_2} & 0 & K_{V_2} & 0 & K_{VH_2} \\ 0 & 0 & 0 & 0 & 0 & 0 \\ 0 & K_{NH_2} & 0 & K_{VH_2} & 0 & K_{H_2} \end{pmatrix}. \tag{A.5}$$

The compliance matrix of the isotropic background can be written as

$$s_b = \begin{pmatrix} E^{-1} & -\nu/E & -\nu/E & 0 & 0 & 0 \\ -\nu/E & E^{-1} & -\nu/E & 0 & 0 & 0 \\ -\nu/E & -\nu/E & E^{-1} & 0 & 0 & 0 \\ 0 & 0 & 0 & \mu^{-1} & 0 & 0 \\ 0 & 0 & 0 & 0 & \mu^{-1} & 0 \\ 0 & 0 & 0 & 0 & 0 & \mu^{-1} \end{pmatrix}, \tag{A.6}$$

where E is Young's modulus and ν is Poisson's ratio, which can be expressed through the Lamé parameters λ and μ:

$$E = \frac{\mu\,(3\lambda + 2\mu)}{\lambda + \mu}; \tag{A.7}$$

$$\nu = \frac{\lambda}{2\,(\lambda + \mu)}. \tag{A.8}$$

Appendix B

Linearized stiffness matrix for two orthogonal fracture sets

Wave phenomena are more conveniently described using the effective stiffness matrix that can be obtained by inverting the compliance matrix A.2. To obtain weak-anisotropy approximations for seismic signatures, the stiffness elements can be linearized in the normalized quantities called fracture *weaknesses*. Following Grechka et al. (2003), the weaknesses for our model can be defined as

$$\Delta_{N_i} \equiv \frac{(\lambda + 2\mu)\, K_{N_i}}{1 + (\lambda + 2\mu)\, K_{N_i}}\,, \tag{B.1}$$

$$\Delta_{V_i} \equiv \frac{\mu K_{V_i}}{1 + \mu K_{V_i}}\,, \tag{B.2}$$

$$\Delta_{H_i} \equiv \frac{\mu K_{H_i}}{1 + \mu K_{H_i}}\,, \tag{B.3}$$

$$\Delta_{NV_i} \equiv \frac{\sqrt{\mu\,(\lambda + 2\mu)} K_{NV_i}}{1 + \sqrt{\mu\,(\lambda + 2\mu)} K_{NV_i}}\,, \tag{B.4}$$

$$\Delta_{NH_i} \equiv \frac{\sqrt{\mu\,(\lambda + 2\mu)} K_{NH_i}}{1 + \sqrt{\mu\,(\lambda + 2\mu)} K_{NH_i}}\,, \tag{B.5}$$

$$\Delta_{VH_i} \equiv \frac{\sqrt{\mu\,(\lambda + 2\mu)} K_{VH_i}}{1 + \sqrt{\mu\,(\lambda + 2\mu)} K_{VH_i}}\,, \tag{B.6}$$

where the subscript $i = 1, 2$ refers to the number of the fracture set. Since the matrix $\mathbf{K}$ has to be nonnegative definite, the weaknesses satisfy the inequalities

$$\Delta^2_{_{IJ}} \leq \Delta_{_I}\, \Delta_{_J}\,, \tag{B.7}$$

where I and J denote the subscripts N, V, and H.

Using equations A.2 and A.4–A.6 and linearizing the stiffness matrix $\mathbf{c} \equiv \mathbf{s}^{-1}$ in the fracture weaknesses (equations B.1–B.6), we obtain

$$\mathbf{c} \approx \begin{pmatrix} c_{11} & c_{12} & c_{13} & \chi c_{24} & c_{15} & c_{16} \\ c_{12} & c_{22} & c_{23} & c_{24} & \chi c_{15} & c_{26} \\ c_{13} & c_{23} & c_{33} & \chi c_{24} & \chi c_{15} & c_{36} \\ \chi c_{24} & c_{24} & \chi c_{24} & c_{44} & 0 & c_{46} \\ c_{15} & \chi c_{15} & \chi c_{15} & 0 & c_{55} & c_{56} \\ c_{16} & c_{26} & c_{36} & c_{46} & c_{56} & c_{66} \end{pmatrix}, \tag{B.8}$$

where

$$\chi \equiv \frac{\lambda}{\lambda + 2\mu}. \tag{B.9}$$

The linearized stiffness elements are given by

$$c_{11} = (\lambda + 2\mu)\left(1 - \Delta_{N_1} - \chi^2 \Delta_{N_2}\right), \tag{B.10}$$
$$c_{12} = \lambda \left(1 - \Delta_{N_1} - \Delta_{N_2}\right), \tag{B.11}$$
$$c_{13} = \lambda \left(1 - \Delta_{N_1} - \chi\, \Delta_{N_2}\right), \tag{B.12}$$
$$c_{14} = -\sqrt{\lambda\mu\chi}\, \Delta_{NV_2}, \tag{B.13}$$
$$c_{15} = -\sqrt{\mu\,(\lambda + 2\mu)}\, \Delta_{NV_1}, \tag{B.14}$$
$$c_{16} = -\sqrt{\mu\,(\lambda + 2\mu)}\, \left(\Delta_{NH_1} + \chi\, \Delta_{NH_2}\right), \tag{B.15}$$
$$c_{22} = (\lambda + 2\mu)\left(1 - \Delta_{N_2} - \chi^2 \Delta_{N_1}\right), \tag{B.16}$$
$$c_{23} = \lambda \left(1 - \chi\, \Delta_{N_1} - \Delta_{N_2}\right), \tag{B.17}$$
$$c_{24} = -\sqrt{\mu\,(\lambda + 2\mu)}\, \Delta_{NV_2}, \tag{B.18}$$
$$c_{25} = -\sqrt{\lambda\mu\chi}\, \Delta_{NV_1}, \tag{B.19}$$
$$c_{26} = -\sqrt{\mu\,(\lambda + 2\mu)}\, \left(\chi\, \Delta_{NH_1} + \Delta_{NH_2}\right), \tag{B.20}$$
$$c_{33} = (\lambda + 2\mu)\left[1 - \chi^2 \left(\Delta_{N_2} + \Delta_{N_1}\right)\right], \tag{B.21}$$
$$c_{34} = -\sqrt{\lambda\mu\chi}\, \Delta_{NV_2}, \tag{B.22}$$
$$c_{35} = -\sqrt{\lambda\mu\chi}\, \Delta_{NV_1}, \tag{B.23}$$
$$c_{36} = -\sqrt{\lambda\mu\chi}\, \left(\Delta_{NH_1} + \Delta_{NH_2}\right), \tag{B.24}$$
$$c_{44} = \mu \left(1 - \Delta_{V_2}\right), \tag{B.25}$$
$$c_{45} = 0, \tag{B.26}$$
$$c_{46} = -\mu \sqrt{\frac{\mu}{\lambda + 2\mu}}\, \Delta_{VH_2}, \tag{B.27}$$
$$c_{55} = \mu \left(1 - \Delta_{V_1}\right), \tag{B.28}$$
$$c_{56} = -\mu \sqrt{\frac{\mu}{\lambda + 2\mu}}\, \Delta_{VH_1}, \tag{B.29}$$
$$c_{66} = \mu \left(1 - \Delta_{H_1} - \Delta_{H_2}\right). \tag{B.30}$$

If the weaknesses of the second fracture set are equal to zero, the linearized effective stiffnesses given above reduce to those obtained by Grechka et al. (2003) for a single microcorrugated fracture set orthogonal to the x_1-axis. Another special case is that of rotationally invariant fractures, for which the off-diagonal weaknesses vanish and the tangential weaknesses Δ_{V_i} and Δ_{H_i} are equal to each other. If both fracture sets are made rotationally invariant, our stiffness matrix becomes identical to that in Bakulin et al. (2000b).

Appendix C

Time-lapse Variations of traveltimes

This appendix illustrates the ideas behind the variational approach that allowed us to describe traveltime shifts in 3D space for heterogeneous, generally anisotropic medium. The problem is to compute the variation of traveltimes t, within a certain time interval $[t_1, t_2]$:

$$\delta t = \delta \int_{t_1}^{t_2} \mathrm{d}t \tag{C.1}$$

Using the definition of the slowness vector as the normal to the wavefront, $p_i = dt/dx_i$ $(i = 1, 2, 3)$ (e.g. Chapman, 2004), we express the variational problem in terms of the slowness vector and the ray position vector $\mathbf{x}$ in Cartesian 3D space:

$$\delta t = \delta \int_{\mathbf{x}_1}^{\mathbf{x}_2} p_i \, \mathrm{d}x_i \,, \tag{C.2}$$

where $\mathbf{x}_1$ and $\mathbf{x}_2$ denote the position vectors for the end points of the reference ray. Here, the summation convention over repeated indexes is assumed. To allow variation of both the slowness and position vectors of the reference ray, we introduce the parameter τ which remains fixed during the perturbation of traveltimes:

$$\delta t = \delta \int_{\tau_2}^{\tau_1} \delta \left(p_i \frac{\mathrm{d}x_i}{\mathrm{d}\tau} \right) \mathrm{d}\tau = \delta \int_{\tau_2}^{\tau_1} \delta \left(p_i \dot{x}_i \right) \mathrm{d}\tau \,. \tag{C.3}$$

The variation of traveltimes should produce perturbed rays that also obey the eikonal equation. To incorporate this "eikonal" constrain into the problem we express it as a function $\mathcal{H}$ (Červený, 2001, e.g.):

$$\mathcal{H}(x_i, p_i) = \frac{1}{2} \left[V^2(x_i, p_i) p_i p_i - 1 \right] = 0 \,, \tag{C.4}$$

where $V(x_i, p_i)$ represents the phase velocity. Then, using a Lagrange multiplier Λ, we incorporate the constrain (C.4) directly into the variation of the traveltime by writing:

$$t = \int_{\tau_1}^{\tau_2} \left(p_i \dot{x}_i + \Lambda \mathcal{H} \right) \mathrm{d}\tau \,. \tag{C.5}$$

If we set $\Lambda = -1$ in the above equation (C.5), the integrand will become a new function

$$\mathcal{L} = p_i \dot{x}_i - \mathcal{H}\,, \tag{C.6}$$

and the parameter τ then represents traveltime along the unperturbed ray. We prove this, first by showing that from equation (C.4) we can define a new vector $u_k = V^2 p_k$, which is actually the group velocity vector, because

$$u_k p_k = 1 \quad \Leftrightarrow \quad u_k = \frac{dx_k}{dt}\,. \tag{C.7}$$

Since traveltimes should come from integration of function $\mathcal{L}$ in equation C.6, then:

$$t = \int_{\tau_1}^{\tau_2} \mathcal{L}\,\mathrm{d}\tau = \int_{\tau_1}^{\tau_2} \left(p_i \dot{x}_i - \mathcal{H}\right) \mathrm{d}\tau\,, \tag{C.8}$$

and by substituting equation C.4 into expression C.8, we obtain

$$t = \int_{\tau_1}^{\tau_2} \left(p_i \dot{x}_i - \frac{1}{2} p_i u_i + \frac{1}{2}\right) \mathrm{d}\tau\,, \tag{C.9}$$

By hypothesis, $dt = d\tau$, which implies $\dot{\mathbf{x}} = \mathbf{u}$. Hence,

$$t = \int_{\tau_1}^{\tau_2} \left(\frac{1}{2} p_i u_i + \frac{1}{2}\right) \mathrm{d}\tau = \int_{\tau_1}^{\tau_2} \mathrm{d}\tau\,,$$

proving that indeed $\tau = t$.

The form of $\mathcal{L}$ in equation C.6 indicates that it relates to $\mathcal{H}$ through a change of variables from group velocity vector $\dot{\mathbf{x}}$ to the slowness vector $\mathbf{p}$. Indeed, on account of definition C.4 and equation C.7, the group velocity $\dot{\mathbf{x}}$ is the gradient of $\mathcal{H}$ in relation to the slowness vector:

$$\dot{x}_i = \frac{\partial \mathcal{H}}{\partial p_i}\,. \tag{C.10}$$

If for each $\mathbf{p}$ there is a corresponding $\dot{\mathbf{x}}$, then equations C.10 are solvable for p_i as a function of $\dot{x}_i$, and $\mathcal{L}$ can be expressed as a function of x_i and $\dot{x}_i$ only. We note that x_i variables remain unchanged and so they are called *passive* variables (Lanczos, 1986). To account for the one-time change in $\mathcal{L}$ caused by the deformation of the medium due to reservoir compaction, we can add time t as another passive variable to the problem. The variation of traveltimes is then the variation of $\mathcal{L}$,

$$\delta t = \int_{\tau_1}^{\tau_2} \delta \mathcal{L} \mathrm{d}\tau = \int_{\tau_1}^{\tau_2} \delta \left(p_i \dot{x}_i - \mathcal{H}\right) \mathrm{d}\tau\,. \tag{C.11}$$

Expanding the perturbations of the integral kernels in equation C.11 above, yields

$$\frac{\partial \mathcal{L}}{\partial x_i} \delta x_i + \frac{\partial \mathcal{L}}{\partial \dot{x}_i} \delta \dot{x}_i + \frac{\partial \mathcal{L}}{\partial t} \delta t =$$

$$\left(\dot{x}_i - \frac{\partial \mathcal{H}}{\partial p_i}\right)\delta p_i + p_i \delta \dot{x}_i - \frac{\partial \mathcal{H}}{\partial x_i}\delta x_i - \frac{\partial \mathcal{H}}{\partial t}\delta t\,. \tag{C.12}$$

In principle, we should have expressed p_i as functions of $\dot{x}_i$ in the equation above. But this is unnecessary, since term-by-term comparison shows that the coefficient of δp_i is already zero in equation C.12. In addition, this comparison implies that

$$p_i = \frac{\partial \mathcal{L}}{\partial \dot{x}_i}\,, \tag{C.13}$$

and

$$\frac{\partial \mathcal{L}}{\partial t} = -\frac{\partial \mathcal{H}}{\partial t}\,, \tag{C.14}$$

$$\frac{\partial \mathcal{L}}{\partial x_i} = -\frac{\partial \mathcal{H}}{\partial x_i}\,. \tag{C.15}$$

Now to solve the perturbation problem we need to know what are the derivatives in equation C.15. To that effect, we observe that the variation of traveltimes is

$$\delta t = \int_{\tau_1}^{\tau_2}\left(\frac{\partial \mathcal{L}}{\partial x_i}\delta x_i + \frac{\partial \mathcal{L}}{\partial \dot{x}_i}\delta \dot{x}_i + \frac{\partial \mathcal{L}}{\partial t}\delta t\right)\mathrm{d}\tau \tag{C.16}$$

Using integration by parts we group the variations in relation to $\mathbf{x}$ and $\dot{\mathbf{x}}$ and, thus, the variation of the traveltimes becomes

$$\begin{aligned}\delta t = {} & \frac{\partial \mathcal{L}}{\partial \dot{x}_i}\delta x_i\bigg|_{\tau_1}^{\tau_2} + \int_{\tau_1}^{\tau_2}\frac{\partial \mathcal{L}}{\partial t}\delta t\,\mathrm{d}\tau \\ & + \int_{\tau_1}^{\tau_2}\left(\frac{\partial \mathcal{L}}{\partial x_i} - \frac{d}{d\tau}\frac{\partial \mathcal{L}}{\partial \dot{x}_i}\right)\delta x_i\,\mathrm{d}\tau\end{aligned} \tag{C.17}$$

If the end-points are fixed, then the first term equals zero in equation (C.17). Likewise, if there was no time variation of $\mathcal{L}$, then the second term would also be zero. If these two conditions hold, then we are back to tracing rays in the reference medium and the real ray trajectory is, according to Fermat's Principle, the one that renders $\delta t = 0$. So now we reach the conclusion that the third term should then be zero, which implies that

$$\frac{\partial \mathcal{L}}{\partial x_i} - \frac{d}{d\tau}\frac{\partial \mathcal{L}}{\partial \dot{x}_i} = 0\,. \tag{C.18}$$

The equations contained in expression (C.18) are in fact the Euler-Lagrange equations (e.g., Lanczos, 1986). By substituting equations C.15 into the Euler-Lagrange equations C.18, we get:

$$\dot{p}_i = \frac{\partial \mathcal{L}}{\partial x_i} = -\frac{\partial \mathcal{H}}{\partial x_i}\,. \tag{C.19}$$

Hence, whereas the variation of $\mathcal{L}(x_i, \dot{x}_i, t)$ depends on second order differential equations in x_i, the variation of $\mathcal{H}(x_i, p_i, t)$ depends only on first-order differential equations, in accordance to equations C.10 and C.13 and C.19. Physically, this means that it is easier to compute traveltime perturbations from variations of slowness surfaces (described by $\mathcal{H}$, the Hamiltonian in classical mechanics jargon) than from wavefronts (described by $\mathcal{L}$, the Lagrangian).

Using equations C.10, C.13 and C.19 the traveltime variation in equation C.11 can be written as

$$\begin{aligned}\delta t &= \int_{\tau_1}^{\tau_2} \left(p_i \delta \dot{x}_i + \dot{p}_i \delta x_i - \frac{\partial \mathcal{H}}{\partial t} \delta t \right) \mathrm{d}\tau \\ &= \int_{\tau_1}^{\tau_2} \left[\frac{d}{d\tau} \left(p_i \delta x_i \right) - \frac{\partial \mathcal{H}}{\partial t} \delta t \right] \mathrm{d}\tau \end{aligned} \tag{C.20}$$

The variation of $\mathcal{H}$ between time-lapse seismic surveys can be chosen as a constant, $\Delta\mathcal{H}$. Hence, the time interval δt, is arbitrary and we set it to unit. We then reach equation (3.1), which shows that first-order traveltime shifts are produced by perturbation of the Hamiltonian along the reference ray and by changes in its end-points:

$$\delta t = p_i \delta x_i \Big|_{\tau_1}^{\tau_2} - \int_{\tau_1}^{\tau_2} \Delta\mathcal{H} d\tau \tag{C.21}$$

It should be emphasized that this approach is only possible, because the relation between slowness surface and the wavefront is one-to-one. Hence, it is not valid near triplications in shear-wave wavefronts in anisotropic media, where ray-tracing approximations break down anyway.

Now it is necessary to describe the Hamiltonian perturbation $\Delta\mathcal{H}$, which arises due to reservoir compaction. Since the first-order perturbation operator works in the same way as a first derivative operator, from equation C.4 we obtain

$$\Delta\mathcal{H} = \frac{1}{2} \left[2V \Delta V p_k p_k \right] = \frac{\Delta V}{V} \,. \tag{C.22}$$

Note that perturbation of the slowness vector p_i is not considered here because it was already accounted for in the derivation of equation C.21. To obtain the perturbation of the velocity, ΔV, it is necessary to perturb the Christoffel equation, which controls the kinematics of seismic wave propagation in the ray theoretical sense. This first-order perturbation approach was first published by Jech and Pšenčik (1989), and here we include a simplified version of it for completeness. We start with the Christoffel equation:

$$\left(\Gamma_{ik} - V^2 \delta_{ik} \right) U_i = 0 \,, \tag{C.23}$$

where U_i is a component of the polarization vector and δ_{ij} is the Kronecher delta. The Christoffel matrix Γ_{ik} is defined in terms of the unit slowness vector $n_i = V\, p_i$:

$$\Gamma_{ik} = a_{ijkl} n_j n_l \,.$$

The first-order perturbation of equation (C.23) above leads to:

$$(\Delta\Gamma_{ik} - 2V\Delta V\delta_{ik})\, U_i + \left(\Gamma_{ik} - V^2\delta_{ik}\right) \Delta U_i = 0\,. \tag{C.24}$$

Further simplification is obtained by noting that multiplication a by polarization component U_k allows the elimination of the term multiplied by ΔU_i on account of the definition of the Christoffel equation (see equation C.23). Then,

$$\Delta\Gamma_{ik}U_iU_k - 2V\Delta V U_kU_k = 0\,.$$

Since the polarization vector is normalized, $U_kU_k = 1$, the equation above yields

$$\Delta V = \frac{\Delta\Gamma_{ik}U_iU_k}{2V} = \frac{\Delta a_{ijkl}n_jn_lU_iU_k}{2V}\,. \tag{C.25}$$

Plugging equation (C.25) into expression (C.22) we achieve a description for traveltime changes in terms of the changes of density-normalized elastic parameters Δa_{ijkl} and the polarization and propagation direction of the reference rays. If we further assume that perturbations are done for P-waves in isotropic background velocity model, then $\mathbf{U} = \mathbf{n}$. As a result, traveltime shifts due to velocity perturbations can be computed along the reference rays as:

$$\delta t = -\int_{\tau_1}^{\tau_2} \frac{\Delta V}{V} \mathrm{d}\tau = -\frac{1}{2}\int_{\tau_1}^{\tau_2} \frac{\Delta a_{ijkl}\, n_in_jn_kn_l}{V^2} \mathrm{d}\tau\,. \tag{C.26}$$

Appendix D

Elements of the matrix $\Delta C_{\alpha\beta}$

Here, we give a brief derivation of the perturbations of the stiffness coefficients obtained from the equation $\Delta c_{ijkl} = c_{ijklmn}\,\Delta e_{mn}$. To simplify the summation over repeated indices we take advantage of the following symmetries of the tensor c_{ijklmn} (e.g., Thurston and Brugger, 1964a):

$$c_{ijklmn} = c_{jiklmn} = c_{ijlkmn} = c_{ijklnm} = c_{klijmn} = c_{mnklij}. \tag{D.1}$$

These symmetries make it possible to use Voigt notation, which reduces the number of independent elements from 729 to 56. These elements are distributed in $6 \times 6 \times 6$ matrices, and the summation is accomplished by multiplying each cube face by the 6×1 vector formed by the element Δe_{ij} of the excess strain tensor:

$$\Delta C_{\alpha\beta} = C_{\alpha\beta\gamma}\,\Delta E_{\gamma}\,, \tag{D.2}$$

where

$$\Delta E_{\gamma} = (\Delta e_{11}, \Delta e_{22}, \Delta e_{33}, 2\Delta e_{23}, 2\Delta e_{13}, 2\Delta e_{12})^{\mathsf{T}}\ . \tag{D.3}$$

The indices α, β and γ run from 1 to 6. Application of equation D.2 is greatly simplified, if the $C_{\alpha\beta\gamma}$ matrices are formed by isotropic tensors, because such a tensor includes only 20 non-zero elements (Hearmon, 1953):

$$C_{111} = C_{222} = C_{333}\,, \tag{D.4}$$
$$C_{144} = C_{255} = C_{366}\,, \tag{D.5}$$
$$C_{112} = C_{223} = C_{133} = C_{113} = C_{122} = C_{233}\,, \tag{D.6}$$
$$C_{155} = C_{244} = C_{344} = C_{166} = C_{266} = C_{355}\,, \tag{D.7}$$
$$C_{123}\,, \tag{D.8}$$
$$C_{456}\,. \tag{D.9}$$

The isotropic symmetry of the sixth-order tensor implies that only three of the components listed above are linearly indepedent. Following the convention adopted in Thurston and Brugger (1964a), non-zero elements $C_{\alpha\beta\gamma}$ for isotropic media can be expressed through linear combinations of three Lamé-type parameters ν_i:

$$C_{111} = \nu_1 + 6\nu_2 + 8\nu_3\,, \tag{D.10}$$
$$C_{112} = \nu_1 + 2\nu_2\,, \tag{D.11}$$
$$C_{123} = \nu_1\,, \tag{D.12}$$
$$C_{144} = \nu_2\,, \tag{D.13}$$
$$C_{155} = \nu_2 + 2\nu_3\,, \tag{D.14}$$
$$C_{456} = \nu_3\,. \tag{D.15}$$

Using the tensor symmetries D.1 and equations D.4–D.9, the perturbations $\Delta C_{\alpha\beta}$ from equation D.2 can be written as

$$\Delta C_{11} = C_{111}\Delta E_1 + C_{112}(\Delta E_2 + \Delta E_3), \tag{D.16}$$
$$\Delta C_{22} = C_{111}\Delta E_2 + C_{112}(\Delta E_1 + \Delta E_3), \tag{D.17}$$
$$\Delta C_{33} = C_{111}\Delta E_3 + C_{112}(\Delta E_1 + \Delta E_2), \tag{D.18}$$

$$\Delta C_{44} = C_{144}\Delta E_1 + C_{155}(\Delta E_2 + \Delta E_3), \tag{D.19}$$
$$\Delta C_{55} = C_{144}\Delta E_2 + C_{155}(\Delta E_1 + \Delta E_3), \tag{D.20}$$
$$\Delta C_{66} = C_{144}\Delta E_3 + C_{155}(\Delta E_1 + \Delta E_2), \tag{D.21}$$

$$\Delta C_{12} = C_{123}\Delta E_3 + C_{112}(\Delta E_1 + \Delta E_2), \tag{D.22}$$
$$\Delta C_{13} = C_{123}\Delta E_2 + C_{112}(\Delta E_1 + \Delta E_3), \tag{D.23}$$
$$\Delta C_{23} = C_{123}\Delta E_1 + C_{112}(\Delta E_2 + \Delta E_3), \tag{D.24}$$

$$\Delta C_{14} = C_{144}\Delta E_4, \tag{D.25}$$
$$\Delta C_{15} = \Delta C_{35} = C_{155}\Delta E_5, \tag{D.26}$$
$$\Delta C_{16} = \Delta C_{26} = C_{155}\Delta E_6, \tag{D.27}$$
$$\Delta C_{24} = \Delta C_{34} = C_{155}\Delta E_4, \tag{D.28}$$
$$\Delta C_{25} = C_{144}\Delta E_5, \tag{D.29}$$
$$\Delta C_{36} = C_{144}\Delta E_6, \tag{D.30}$$

$$\Delta C_{45} = C_{456}\Delta E_6, \tag{D.31}$$
$$\Delta C_{46} = C_{456}\Delta E_5, \tag{D.32}$$
$$\Delta C_{56} = C_{456}\Delta E_4\,. \tag{D.33}$$

Appendix E

Perturbation of the Hamiltonian

To derive the perturbation of the Hamiltonian in equation 3.9 of the main text, we use equation 3.14 and assume that the strain-sensitivity tensor is isotropic (see Appendix D). First, we evaluate the numerator B of equation 3.9:

$$B = \Delta a_{ijkl}\, n_i n_j n_k n_l \,, \tag{E.1}$$

where Δa_{ijkl} are the density-normalized stiffness perturbations, and $\mathbf{n}$ is the unit slowness vector. Using Voigt notation to replace Δa_{ijkl} by the 6×6 matrix $\Delta A_{\alpha\beta}$ (α and β run from one to six), we find:

$$\begin{aligned} B = & \Delta A_{11} n_1^4 + \Delta A_{22} n_2^4 + \Delta A_{33} n_3^4 + 2\left(\Delta A_{12} + 2\Delta A_{66}\right) n_1^2 n_2^2 \\ & + 2\left(\Delta A_{13} + 2\Delta A_{55}\right) n_1^2 n_3^2 + 2\left(\Delta A_{23} + 2\Delta A_{44}\right) n_2^2 n_3^2 \\ & + 4\left(\Delta A_{16} n_1^2 + \Delta A_{26} n_2^2\right) n_1 n_2 + 4\left(\Delta A_{15} n_1^2 + \Delta A_{35} n_3^2\right) n_1 n_3 \\ & + 4\left(\Delta A_{24} n_2^2 + \Delta A_{34} n_3^2\right) n_2 n_3 + 4\left(\Delta A_{14} + 2\Delta A_{56}\right) n_1^2 n_2 n_3 \\ & + 4\left(\Delta A_{25} + 2\Delta A_{46}\right) n_1 n_2^2 n_3 + 4\left(\Delta A_{36} + 2\Delta A_{45}\right) n_1 n_2 n_3^2 \,. \end{aligned} \tag{E.2}$$

Note that $\Delta A_{\alpha\beta} = \rho^{-1} \Delta C_{\alpha\beta}$, where $\Delta C_{\alpha\beta}$ are given by equations D.16–D.33. Substituting equations D.16–D.33 into equation E.2 and taking into consideration equations D.10–D.15 leads to

$$\begin{aligned} \rho B = & \left[C_{111} \Delta E_1 + C_{112}\left(\Delta E_2 + \Delta E_3\right)\right] n_1^4 \\ & + \left[C_{111} \Delta E_2 + C_{112}\left(\Delta E_1 + \Delta E_3\right)\right] n_2^4 \\ & + \left[C_{112}\left(\Delta E_1 + \Delta E_2\right) + C_{111} \Delta E_3\right] n_3^4 \\ & + 2\left[C_{112} \Delta E_3 + \left(C_{112} + 2C_{155}\right)\left(\Delta E_1 + \Delta E_2\right)\right] n_1^2 n_2^2 \\ & + 2\left[C_{112} \Delta E_2 + \left(C_{112} + 2C_{155}\right)\left(\Delta E_1 + \Delta E_3\right)\right] n_1^2 n_3^2 \\ & + 2\left[C_{112} \Delta E_1 + \left(C_{112} + 2C_{155}\right)\left(\Delta E_2 + \Delta E_3\right)\right] n_2^2 n_3^2 \\ & + 4C_{155} n_1 n_2 n_3 \left(\Delta E_4 n_1 + \Delta E_5 n_2 + \Delta E_6 n_3\right) \\ & + 4C_{155} \left[\Delta E_6 n_1 n_2 \left(n_1^2 + n_2^2\right)\right. \\ & \left. + \Delta E_5 n_1 n_3 \left(n_1^2 + n_3^2\right) + \Delta E_4 n_2 n_3 \left(n_2^2 + n_3^2\right)\right] \,. \end{aligned} \tag{E.3}$$

Combining the terms containing C_{111}, C_{112} and C_{155} in equation E.3 yields

$$\begin{aligned}\rho B = &(C_{111} - C_{112}) \left(\Delta E_1 n_1^4 + \Delta E_2 n_2^4 + \Delta E_3 n_3^4\right) \\ &+ C_{112} e_{kk} + 4C_{155} \left[\Delta E_1 \left(n_1^2 - n_1^4\right)\right. \\ &+ \Delta E_2 \left(n_2^2 - n_2^4\right) + \Delta E_3 \left(n_3^2 - n_3^4\right) \\ &\left.+\Delta E_6 n_1 n_2 + \Delta E_5 n_1 n_3 + \Delta E_4 n_2 n_3\right],\end{aligned} \tag{E.4}$$

where Δe_{kk} is the trace of the excess strain tensor $\Delta e_{ij} = \Delta E_\gamma$. It follows from equations D.10–D.15 that $C_{111} - C_{112} = 4C_{155}$, which allows us to obtain B as

$$\begin{aligned}\rho B = &C_{112} \Delta e_{kk} + 4C_{155} \left(\Delta E_1 n_1^2 + \Delta E_6 n_1 n_2 + \Delta E_2 n_2^2\right. \\ &\left.+\Delta E_5 n_1 n_3 + \Delta E_4 n_2 n_3 + \Delta E_3 n_3^2\right) .\end{aligned} \tag{E.5}$$

In tensor notation, equation E.5 becomes

$$\rho B = C_{112} \Delta e_{kk} + 4C_{155} \Delta e_{ij} n_i n_j \,. \tag{E.6}$$

The contribution of the quadratic form $\Delta e_{ij}\, n_i n_j$ to the stiffness perturbations in equation E.6 causes the resulting velocity anisotropy to be elliptical.

Another interesting property of equation E.6 is that B is comprised of two terms, one of which is controlled by the volumetric changes (i.e., by Δe_{kk}). The strain tensor Δe_{ij} can be represented through its deviatoric ($\Delta \varepsilon_{ij}$) and dilational (Δe_{kk}) components:

$$\Delta e_{ij} = \Delta \varepsilon_{ij} + \frac{1}{3} \Delta e_{kk}\, \delta_{ij} \,,$$

and equation E.6 takes the form

$$\rho B = \frac{1}{3} \left(3C_{112} + 4C_{155}\right) \Delta e_{kk} + 4C_{155}\, \Delta \varepsilon_{ij} n_i n_j \,. \tag{E.7}$$

Using equations D.10 – D.15, we find that $3C_{112} + 4C_{155} = C_{111} + 2C_{112}$. Linear Hooke's law helps to express the deviatoric strain through the deviatoric stress as $\Delta \varepsilon_{ij} = \Delta \sigma_{ij}/(2c_{44})$, which leads to the following expression for the term B:

$$\rho B = \frac{1}{3} \left(C_{111} + 2C_{112}\right) \Delta e_{kk} + 2 \frac{c_{155}}{c_{44}}\, \Delta \sigma_{ij} n_i n_j \,. \tag{E.8}$$

Equation E.8 represents B as the sum of the contributions of the volumetric changes Δe_{kk} and the deviatoric stress changes $\Delta \sigma_{ij}$.

Appendix F

Comparison with equations for zero-offset data

Here we compare our equation 3.17 with the equation of Hatchell and Bourne (2005b) for zero-offset traveltime shifts. We consider zero-offset rays reflected from a horizontal interface in an isotropic homogeneous background medium. In addition, displacements are assumed to be vertical. Therefore, the only nonzero components of the slowness and displacement vectors in equation 3.17 are p_3 and δx_3:

$$\delta t = p_3 u_3 \Big|_{\tau_1}^{\tau_2} - \int_{\tau_2}^{\tau_1} \frac{\Delta V}{V} \mathrm{d}\tau \tag{F.1}$$

where $\delta x_3 = u_3$. Bringing the endpoint contributions under the integral, we obtain

$$\delta t = \int_{\tau_1}^{\tau_2} \left[\frac{\mathrm{d}\,(p_3 u_3)}{\mathrm{d}\tau} - \frac{\Delta V}{V} \right] \mathrm{d}\tau \,. \tag{F.2}$$

Expanding the derivative in the integrand and changing variables ($\mathrm{d}\tau = \mathrm{d}z/V$) yields the two-way traveltime shift:

$$\delta t = 2 \int_{0}^{Z} \left[V p_3 \frac{\mathrm{d}u_3}{\mathrm{d}z} + V u_3 \frac{\mathrm{d}p_3}{\mathrm{d}z} - \frac{\Delta V}{V} \right] \frac{\mathrm{d}z}{V} \,. \tag{F.3}$$

The integration is carried out from the surface ($z = 0$) to the reflector depth Z. From the eikonal equation it follows that $p_3 = 1/V$, and

$$\delta t = 2 \int_{0}^{Z} \left[\frac{\mathrm{d}u_3}{\mathrm{d}z} + V u_3 \frac{\mathrm{d}p_3}{\mathrm{d}z} - \frac{\Delta V}{V} \right] \frac{\mathrm{d}z}{V} \,. \tag{F.4}$$

Since the reference ray is traced in a homogeneous medium, $\mathrm{d}p_3/\mathrm{d}z = 0$. Also, according to the definition of the strain tensor, $\Delta e_{zz} = \mathrm{d}u_3/\mathrm{d}z$. Hence,

$$\delta t = 2 \int_{0}^{Z} \left[\Delta e_{zz} - \frac{\Delta V}{V} \right] \frac{\mathrm{d}z}{V} \,. \tag{F.5}$$

Equation F.5 is equivalent to the zero-offset result of Hatchell and Bourne (2005b) who rewrite δt as follows:

$$\delta t = 2 \int_{0}^{Z} (1 + R) \frac{\Delta e_{zz}}{V} \mathrm{d}z, \tag{F.6}$$

where

$$R = -\frac{\Delta V}{V}\frac{1}{\Delta e_{zz}}\,. \tag{F.7}$$

The equivalence of equations F.5 and F.6 confirms that equation 3.17 represents a generalization of previously published results.

Appendix G

Independent Elements of The TOE Tensor

Here, we follow Fumi (1951, 1952) and Hearmon (1953) to describe the independent elements of the third-order elastic tensor for several common symmetry classes. Independent elements c_{ijklmn} for a given class should remain invariant with respect to rotations around a symmetry axis or reflections through a symmetry plane. According to the definition of a sixth-rank Cartesian tensor, such invariance implies that any independent element c_{ijklmn} should satisfy the following set of equations:

$$c_{ijklmn} - c_{pqrsuv} R_{ip} R_{jq} R_{kr} R_{ls} R_{mu} R_{nv} = 0 \,, \tag{G.1}$$

where R_{ij} is the unitary matrix describing the transformation of the tensor c_{ijklmn} due to a coordinate change. Equation G.1 is used below to identify the set of independent elements for triclinic, monoclinic, orthorhombic, hexagonal and isotropic TOE tensors starting with the lower symmetries[1].

G.1 Triclinic Symmetry

The number N of independent elements $C_{\alpha\beta\gamma}$ for triclinic media can be found from the symmetry properties in equation 5.6 by taking into account that each index changes from 1 to 6 (Toupin and Bernstein, 1961):

$$N = \binom{6+3-1}{3} = \frac{8!}{3!\,5!} = 56 \,. \tag{G.2}$$

These 56 independent elements populate six full 6×6 symmetric matrices (equation 5.8).

G.2 Monoclinic Symmetry

For monoclinic media, only a subset of the 56 elements $C_{\alpha\beta\gamma}$ is independent. Since monoclinic symmetry has one mirror symmetry plane, the independent elements are the solutions of equation G.1 written for a reflection with respect to this plane. Assuming that

[1] Helbig (1994) uses the same approach to identify the independent elements of SOE tensors.

the symmetry plane is horizontal, the matrix R_{ij} in equation G.1 is

$$\mathbf{R} = \begin{pmatrix} 1 & 0 & 0 \\ 0 & 1 & 0 \\ 0 & 0 & -1 \end{pmatrix} . \tag{G.3}$$

Substituting equation G.3 into equation G.1, we find that each of the 56 equations reduces to:

$$c_{ijklmn} = (-1)^p c_{ijklmn} , \tag{G.4}$$

where p is the number of times that the index 3 appears in c_{ijklmn}. Hence, only the elements c_{ijklmn} with an even number of indices 3 satisfy equation G.4. The nonzero elements $C_{\alpha\beta\gamma}$ for monoclinic symmetry with a horizontal symmetry plane are listed in equations 5.9 and 5.10.

G.3 Orthorhombic Symmetry

Orthorhombic models are characterized by three orthogonal symmetry planes or, alternatively, by three orthogonal 2-fold symmetry axes. To identify the independent elements $C_{\alpha\beta\gamma}$, one can start with the monoclinic TOE tensor analyzed above and require invariance for reflection with respect to both vertical planes ($[x_1, x_3]$ or $[x_2, x_3]$). For example, the matrix R_{ij} for reflection with respect to the $[x_1, x_3]$-plane is

$$\mathbf{R} = \begin{pmatrix} 1 & 0 & 0 \\ 0 & -1 & 0 \\ 0 & 0 & 1 \end{pmatrix} . \tag{G.5}$$

Substitution of equation G.5 into equation G.1 yields 32 equations (one for each independent element of the monoclinic tensor c_{ijklmn}). These equations have the form of expression G.4, but the exponent p now stands for the number of times the index 2 appears in c_{ijklmn}. Therefore, the independent elements $C_{\alpha\beta\gamma}$ for orthorhombic symmetry should have an even number of indices 2 and 3. A similar procedure is applied to reflection with respect to the $[x_2, x_3]$-plane. The resulting matrix $C_{\alpha\beta\gamma}$, given in equations 5.11–5.14, has 20 independent elements.

G.4 Hexagonal Symmetry

To find out which components of the hexagonal tensor c_{ijklmn} are independent, we require that the elements c_{ijklmn} for orthorhombic media remain invariant with respect to rotation by $\theta = 2\pi/3$ around the axis x_3. The corresponding rotation matrix can be written as (Goldstein, 1980)

$$R = \begin{pmatrix} \cos\theta & \sin\theta & 0 \\ -\sin\theta & \cos\theta & 0 \\ 0 & 0 & 1 \end{pmatrix} . \tag{G.6}$$

Because the matrix R has nonzero off-diagonal elements, equations G.1 no longer reduce to a simple form similar to that of equation G.4. Instead, one needs to solve systems of equations that relate certain groups of nonzero elements $C_{\alpha\beta\gamma}$. These systems can be obtained by transposing equations A1–A10 of Hearmon (1953).[2]

From equations A1, A3 and A5–A7 of Hearmon (1953) one can deduce the constraints given in equations 5.15–5.23 above. Finally, we note that for any rotation around the x_3-axis, C_{333} always remains the same. Hence, it is the tenth (and last) independent element of the hexagonal TOE tensor.

G.5 Isotropy

A simple way of making the TOE tensor isotropic is to require that the 10 independent elements of the hexagonal tensor remain unchanged for arbitrary rotation around any axis. For example, c_{ijklmn} should stay the same when we interchange any two indices. Hence,

$$C_{111} = C_{222} = C_{333}; \tag{G.7}$$

$$C_{112} = C_{133} = C_{223} = C_{113} = C_{122} = C_{233}; \tag{G.8}$$

$$C_{144} = C_{255} = C_{366}; \tag{G.9}$$

$$C_{155} = C_{266} = C_{344} = C_{166} = C_{244} = C_{355}; \tag{G.10}$$

Taking into consideration the constraints in equations 5.15–5.23, the identities in equations G.7–G.10 also imply that

$$C_{112} = C_{123} + 2C_{144} , \tag{G.11}$$

$$C_{111} = C_{123} + 6C_{144} + 8C_{456} . \tag{G.12}$$

Therefore, the isotropic TOE tensor is completely defined by three independent constants (C_{123}, C_{144} and C_{456}), as shown in several publications (e.g. Barsch and Chang, 1968). The matrix representation of the isotropic TOE tensor is given in equations 5.28–5.34.

[2]This transposition is necessary because in our notation $C_{112} = c_{111122}$, as in Fumi (1952), and not $C_{112} = 3c_{111122}$, as in Hearmon (1953).